

THESIS FOR THE DEGREE OF DOCTOR OF PHILOSOPHY

VCSELS for High-Speed, Long-Reach, and
Wavelength-Multiplexed Optical Interconnects

Erik Haglund



Photonics Laboratory
Department of Microtechnology and Nanoscience (MC2)
CHALMERS UNIVERSITY OF TECHNOLOGY
Göteborg, Sweden, 2015

VCSELs for High-Speed, Long-Reach, and Wavelength-Multiplexed Optical Interconnects

Erik Haglund

Göteborg, August 2015

© Erik Haglund, 2015

ISBN 978-91-7597-255-8

Doktorsavhandlingar vid Chalmers Tekniska Högskola
Ny serie 3936
ISSN 0346-718X

Technical Report MC2-315
ISSN 1652-0769

Photonics Laboratory
Department of Microtechnology and Nanoscience (MC2)
Chalmers University of Technology, SE-412 96 Göteborg, Sweden
Phone: +46 (0) 31 772 1000

Front cover illustration: From left to right: a 50 Gbit/s eye diagram, high-speed VCSELs on a chip, and cross-section SEM image of released free-hanging grating bars (each bar is around 250 nm wide).

Printed by Chalmers reproservice, Chalmers University of Technology
Göteborg, Sweden, August, 2015

VCSELs for High-Speed, Long-Reach, and Wavelength-Multiplexed Optical Interconnects

Erik Haglund

Photonics Laboratory

Department of Microtechnology and Nanoscience (MC2)
Chalmers University of Technology, SE-412 96 Göteborg, Sweden

Abstract

The vertical-cavity surface-emitting laser (VCSEL) is the standard light source in short-reach fiber-optic links in datacenters and supercomputers. These systems use an enormous number of links, making cost and energy efficiency pressing issues. GaAs-based 850 nm VCSELs are therefore attractive due to low-cost fabrication, a small device footprint enabling compact integration into 2-D arrays, and above all, the capability of high-speed direct modulation at low power consumption. However, present commercial VCSELs, operating at around 25 Gbit/s over up to 100 m of multimode fiber, have insufficient speed, energy-efficiency, and reach for future links.

Many of the attractive VCSEL properties stem from their small modal and active region volumes. The first part of this thesis explores the limits of optical and electrical confinement in high-speed VCSELs by using the shortest possible cavity length, and positioning the current-confining oxide aperture close to the active region. This enabled small-oxide-aperture VCSELs with record-high modulation bandwidth of 30 GHz, capable of energy-efficient data transmission at 25-50 Gbit/s with record-low dissipated energy per bit in the VCSEL of <100 fJ/bit.

High-speed VCSELs are usually transverse multimode with large spectral widths. This leads to penalties from chromatic and modal fiber dispersion, limiting the feasible transmission distance to around 100 m at 25 Gbit/s, which is too short for large datacenters. The second part of this thesis demonstrates that VCSELs with narrow spectral widths, realized using either a small oxide aperture or an integrated mode filter, can transmit data at high bit rates over much longer distances. VCSELs with mode filters enabled transmission at 20 Gbit/s over 2000 m, setting a bit-rate-distance product record for directly modulated 850 nm VCSEL links.

To enable higher link capacity, wavelength division multiplexing may be used, where several channels at different wavelengths are transmitted in the same fiber. The final part of the thesis presents the design, fabrication, and experimental results for monolithically integrated 980 nm multi-wavelength VCSEL arrays. By using high-contrast gratings with different parameters as top mirrors, the VCSEL resonance wavelength may be set in a post-growth process. Lasing over a wavelength span of 15 nm was realized.

Keywords: vertical-cavity surface-emitting laser, optical interconnect, high-speed modulation, spectral width, oxide aperture, quasi-single-mode, mode filter, high-contrast grating, wavelength control.

List of Papers

This thesis is based on the following appended papers:

- [A] **E. Haglund**, P. Westbergh, J. S. Gustavsson, E. P. Haglund, A. Larsson, “High-speed VCSELs with strong confinement of optical fields and carriers,” to appear in *J. of Lightwave Technol.*, vol. 33, no. 24, pp. 1-9, Dec. 2015, (invited paper).
- [B] **E. Haglund**, P. Westbergh, J. S. Gustavsson, E. P. Haglund, A. Larsson, M. Geen, and A. Joel, “30 GHz bandwidth 850 nm VCSEL with sub-100 fJ/bit energy dissipation at 25-50 Gbit/s,” *Electron. Lett.*, vol. 51, no. 14, pp. 1096-1098, July 2015.
- [C] R. Safaisini, K. Szczerba, **E. Haglund**, P. Westbergh, J. S. Gustavsson, A. Larsson, and P. Andrekson, “20 Gbit/s error-free operation of 850 nm oxide-confined VCSELs beyond 1 km of multimode fibre,” *Electron. Lett.*, vol. 48, no. 19, pp. 1225-1227, Sept. 2012.
- [D] R. Safaisini, K. Szczerba, P. Westbergh, **E. Haglund**, B. Kögel, J. S. Gustavsson, A. Larsson, and P. Andrekson, “High-Speed 850 nm quasi-single-mode VCSELs for extended-reach optical interconnects,” *J. Opt. Commun. Netw.*, vol. 5, no. 7, pp. 686-695, July 2013.
- [E] **E. Haglund**, Å. Haglund, P. Westbergh, J. S. Gustavsson, B. Kögel, and A. Larsson, “25 Gbit/s transmission over 500 m multimode fibre using 850 nm VCSEL with integrated mode filter,” *Electron. Lett.*, vol. 48, no. 9, pp. 517-518, April 2012.
- [F] **E. Haglund**, Å. Haglund, J. S. Gustavsson, B. Kögel, P. Westbergh, and A. Larsson, “Reducing the spectral width of high speed oxide confined VCSELs using an integrated mode filter,” *Proc. of SPIE*, vol. 8276, pp. 82760L1-8, Feb. 2012.
- [G] R. Safaisini, **E. Haglund**, P. Westbergh, J. S. Gustavsson, and A. Larsson, “20 Gb/s data transmission over 2 km multimode fibre using 850 nm mode filter VCSELs,” *Electron. Lett.*, vol. 50, no. 1, pp. 40-42, Jan. 2014.
- [H] **E. Haglund**, J. S. Gustavsson, J. Bengtsson, Å. Haglund, A. Larsson, D. Fattal, W. Sorin, and M. Tan, “Demonstration of post-growth wavelength setting of VCSELs using high-contrast gratings,” submitted to *Opt. Express*, Aug. 2015.

Related publications and conference contributions by the author not included in the thesis:

Journal papers

- [I] P. Westbergh, R. Safaisini, **E. Haglund**, B. Kögel, J. S. Gustavsson, A. Larsson, M. Geen, R. Lawrence, and A. Joel, "High-speed 850 nm VCSELs with 28 GHz modulation bandwidth operating error-free up to 44 Gbit/s," *Electron. Lett.*, vol. 48, no. 18, pp. 1145-1147, Aug. 2012.
- [J] P. Westbergh, R. Safaisini, **E. Haglund**, J. S. Gustavsson, A. Larsson, M. Geen, R. Lawrence, and A. Joel, "High-speed oxide confined 850-nm VCSELs operating error-free at 40 Gb/s up to 85°C," *IEEE Photon. Techn. Lett.*, vol. 25, no. 8, pp. 768-771, April 2013.
- [K] P. Westbergh, E. P. Haglund, **E. Haglund**, R. Safaisini, J. S. Gustavsson, and A. Larsson, "High-speed 850 nm VCSELs operating error free up to 57 Gbit/s," *Electron. Lett.*, vol. 49, no. 16, pp. 1021-1023, Aug. 2013.

Conference presentations and papers

- [L] P. Westbergh, **E. Haglund**, J. S. Gustavsson, Å. Haglund, B. Kögel, and A. Larsson, "High speed VCSELs for short reach communication," *European Semiconductor Laser Workshop 2011*, Lausanne, Switzerland, Sept. 2011.
- [M] A. Larsson, J. S. Gustavsson, Å. Haglund, J. Bengtsson, B. Kögel, P. Westbergh, R. Safaisini, **E. Haglund**, K. Szczerba, M. Karlsson, and P. Andrekson, "High speed VCSELs for optical interconnects," *24th International Conference on Indium Phosphide and Related Materials 2012*, Santa Barbara, CA, USA, paper Th-2C.1, Aug. 2012.
- [N] A. Larsson, J. S. Gustavsson, Å. Haglund, B. Kögel, J. Bengtsson, P. Westbergh, **E. Haglund**, and P. P. Baveja, "High-speed tunable and fixed-wavelength VCSELs for short-reach optical links and interconnects," in *Proc. of SPIE*, vol. 8276, pp. 82760H1-9, San Francisco, CA, USA, Feb. 2012.
- [O] P. Westbergh, R. Safaisini, **E. Haglund**, B. Kögel, J. S. Gustavsson, A. Larsson, and A. Joel, "High-speed 850 nm VCSELs with 28 GHz modulation bandwidth," *European Semiconductor Laser Workshop 2012*, Brussels, Belgium, Sept. 2012.
- [P] R. Safaisini, K. Szczerba, **E. Haglund**, P. Westbergh, J. S. Gustavsson, A. Larsson, and P. Andrekson, "22 Gb/s error-free data transmission beyond 1 km of multi-mode fiber using 850 nm VCSELs," in *Proc. of SPIE*, vol. 8639, pp. 86390T1-7, San Francisco, CA, USA, Feb. 2013.
- [Q] P. Westbergh, R. Safaisini, **E. Haglund**, J. S. Gustavsson, A. Larsson, and A. Joel, "High-speed 850 nm VCSELs with 28 GHz modulation bandwidth for short reach communication," in *Proc. of SPIE*, vol. 8639, pp. 86390X1-6, San Francisco, CA, USA, Feb. 2013.
- [R] J. S. Gustavsson, A. Larsson, Å. Haglund, J. Bengtsson, P. Westbergh, R. Safaisini, and **E. Haglund**, "High speed 850nm VCSELs for >40Gb/s transmission," in *Optical Fiber Communication Conference (OFC) 2013*, San Francisco, CA, USA, paper OTh4H.4, Feb. 2013.
- [S] P. Westbergh, R. Safaisini, **E. Haglund**, J. S. Gustavsson, A. Larsson, and A. Joel, "High speed oxide confined 850 nm VCSELs operating error-free at 47 Gbit/s at room

temperature and 40 Gbit/s at 85°C;” *Conference of Lasers and Electro-Optics (CLEO) Europe*, Munich, Germany, paper CB-7.1, May 2013.

- [T] J. S. Gustavsson, A. Larsson, Å. Haglund, J. Bengtsson, P. Westbergh, R. Safaisini, and **E. Haglund**, “High-speed, high-temperature VCSELs for optical interconnects,” in *IEEE Photonic Society Summer Topical Meeting Series 2013*, Waikoloa, HI, USA, paper MA2.2, July 2013.
- [U] **E. Haglund**, P. Westbergh, E. P. Haglund, R. Safaisini, J. S. Gustavsson, K. Szczerba, Å. Haglund, and A. Larsson, “850 nm datacom VCSELs for higher-speed and longer-reach transmission,” *European VCSEL Day*, Lausanne, Switzerland, June 2013.
- [V] A. Larsson, P. Westbergh, J. S. Gustavsson, **E. Haglund**, and E. P. Haglund, “High speed VCSELs and VCSEL arrays for single and multicore fiber interconnects,” in *Proc. of SPIE*, vol. 9381, pp. 93810D1-11, San Francisco, CA, USA, Feb. 2015.
- [W] S. Kumari, J. S. Gustavsson, R. Wang, E. P. Haglund, P. Westbergh, D. Sanchez, **E. Haglund**, Å. Haglund, J. Bengtsson, N. Le Thomas, G. Roelkens, A. Larsson, and R. Baets, “Integration of GaAs-based VCSEL array on SiN platform with HCG reflectors for WDM applications,” in *Proc. of SPIE*, vol. 9372, pp. 93720U1-7, San Francisco, CA, USA, Feb. 2015.
- [X] **E. Haglund**, P. Westbergh, J. S. Gustavsson, E. P. Haglund, A. Larsson, M. Geen, and A. Joel, “High-speed 850 nm VCSEL with 30 GHz modulation bandwidth,” *Conference of Lasers and Electro-Optics (CLEO) Europe*, Munich, Germany, paper CB-2.4, June 2015.

Other publications

- [Y] **E. Haglund**, Å. Haglund, P. Westbergh, J. S. Gustavsson, B. Kögel, and A. Larsson, “Mode-filtered semiconductor lasers enable longer-reach optical interconnects,” *SPIE Newsroom*, Oct. 2012.

Acknowledgement

There are many who have supported me during the last five years, making this work possible. I would first like to thank my supervisor and examiner Prof. Anders Larsson for letting me work in this exciting field, and for his friendly support, with a door always open for discussions. I would like to thank Åsa Haglund for cheerfully sharing her vast experience in VCSELs, and also for, together with Petter Westbergh, giving me an excellent introduction to the fine art of VCSEL processing. However, no VCSELs would have been fabricated without the outstanding Nanofabrication Laboratory staff, working endlessly to keep our magnificent cleanroom running. I am also grateful to Johan S. Gustavsson and Jörgen Bengtsson for simulations of VCSELs and HCGs, Rashid Safaisini for collaboration on difficult projects, Krzysztof Szczerba for answering any question in the world, Benjamin Kögel for teaching me about courage, and Emanuel Haglund for discussions about everything from shaving to VCSELs. My office mates Martin Stattin and Attila Fülöp deserves many thanks for their support in dealing with problems both large and small. I am very lucky to work at the Photonics Lab with so many great past and present Fiber Guys and Opto Dudes, and an excellent secretary in Jeanette Träff. I'm especially grateful to Tobias, Aleš, and Clemens for many memorable moments.

There would be no HCG-VCSELs without the enthusiasm of Mike Tan, David Fattal, and Wayne Sorin at HP Labs in Palo Alto. Wayne Sorin is also acknowledged for the HCG reflectivity measurement, David Fattal for HCG simulations, and Prof. Mattias Hammar at KTH for providing the epitaxial 980 nm HCG test structure.

This thesis is latest step in my, so far, 23 year long education. I would not have made it this far without great teachers and mentors guiding me along and inspiring me. I'm especially grateful to Mr. Thomas Walters at Bell Lane School, London, Jan Stumle at Tingvallagymnasiet, Karlstad, and Tobias Gründl and Christian Grasse, formerly at TU München.

Finally, I want to thank my wonderful family and friends, and my lovely Hanna, for always being there for me.

The research on high-speed VCSELs was financially supported by the Swedish Foundation for Strategic Research (SSF) projects LASTECH and MUTOI, and the European FP7 project VISIT (224211). The high-contrast grating project was financed by HP Labs. IQE Europe is gratefully acknowledged for supplying the epitaxial VCSEL material.

Erik Haglund

Göteborg
August 2015

Abbreviations

4-PAM	four-level pulse amplitude modulation	MBE	molecular beam epitaxy
ACC	air-coupled cavity	MCF	multicore fiber
AOC	active optical cable	MEMS	micro-electric-mechanical system
AR	anti-reflection	MMF	multi-mode fiber
ARDE	aspect-ratio-dependent etching	MOCVD	metal-organic chemical vapor deposition
BCB	benzocyclobutene	MUX	multiplexer
BER	bit error rate	NCU	National Central University, Taiwan
BR	bit rate	OOK	on-off keying
BTB	back-to-back	OSA	optical spectrum analyzer
BW	bandwidth	PECVD	plasma-enhanced chemical vapor deposition
CMOS	complementary metal-oxide-semiconductor	PL	photoluminescence
DBR	distributed Bragg reflector	PRBS	pseudorandom binary sequence
DEMUX	demultiplexer	QW	quantum well
DFB	distributed feedback laser	RCWA	rigorous coupled-wave analysis
EC	extended cavity	RF	radio frequency
EDR	energy-to-data ratio	RIE	reactive ion etching
FEC	forward error correction	RMS	root-mean-square
flops	floating-point operations per second	RT	room temperature
FWHM	full width at half maximum	SCC	semiconductor-coupled cavity
HCG	high-contrast grating	SCH	separate confinement heterostructure
HDR	heat-to-data ratio	SEM	scanning electron microscopy
HPC	high-performance computing	SDM	spatial-division multiplexing
ICP	inductively-coupled plasma	SMF	single-mode fiber
IV	current-voltage	SMSR	side-mode suppression ratio
LED	light-emitting diode	SOI	silicon on insulator
		TE	transverse electric
		TM	transverse magnetic
		TUB	Technical University of Berlin
		UIUC	University of Illinois, Urbana-Champaign
		VCSEL	vertical-cavity surface-emitting laser
		VOA	variable optical attenuator
		WDM	wavelength-division multiplexing
		WPE	wall-plug efficiency

Table of Contents

Abstract	i
List of Papers	iii
Acknowledgement	vii
Abbreviations	ix
1 Introduction	1
1.1 VCSELs in Optical Interconnects	2
1.2 High-Speed VCSELs	3
1.3 VCSELs for Energy-Efficient Data Transmission	5
1.4 Longer-Reach Optical Interconnects	8
1.5 Multiplexing in Optical Interconnects	10
1.6 Scope and Outline of Thesis	12
2 VCSEL Fundamentals	13
2.1 History of VCSELs	14
2.2 Cavity and Mirrors	14
2.3 Active Region	16
2.4 Optical and Electrical Confinement	17
2.5 Spectral Characteristics	19
2.6 Thermal Properties	22
3 VCSEL Dynamics	25
3.1 Intrinsic Dynamics	25
3.2 Thermal Limitations	29
3.3 Parasitic Effects	31
3.4 High-Speed VCSEL Design	32
3.5 High-Speed Characterization	34
3.5.1 Small-Signal Modulation Response	34

3.5.2	Large-Signal Modulation and Data Transmission	35
4	Quasi-Single Mode VCSELS	37
4.1	Small Oxide Aperture	38
4.2	Surface Relief Mode Filter	39
4.2.1	Effects on Static Characteristics	41
5	VCSEL Fabrication	43
5.1	Lithography	43
5.2	Thin Film Deposition	44
5.3	Etching	45
5.4	Wet Oxidation	46
5.5	High-Speed VCSEL Process	46
5.5.1	Surface-Relief Processing	48
6	Monolithic Multi-Wavelength HCG-VCSEL Arrays	49
6.1	Monolithic Multi-Wavelength VCSEL Arrays	49
6.2	High-Contrast Gratings	51
6.3	Physics of HCGs	52
6.4	Design of Multi-Wavelength HCG-VCSEL Arrays	55
6.4.1	Transverse Electrical Confinement	56
6.4.2	Semiconductor-Air Interface	57
6.4.3	Wavelength-Setting and Threshold Material Gain	59
7	HCG Fabrication	61
7.1	HCG Definition	62
7.2	HCG Dry Etching	63
7.3	GaAs/InGaP HCGs for 980 nm VCSELS	64
7.4	AlGaAs/GaAs HCGs for 850 nm VCSELS	66
7.5	HCG-VCSEL Fabrication	67
8	HCG-VCSEL Experiments	69
8.1	Test Structures	69
8.2	HCG-VCSELS	71
8.2.1	Single-Mode Emission	72
9	Outlook and Future Directions	75
10	Summary of Papers	79
	References	85
	Papers A–H	107

Chapter 1

Introduction

Few people in the industrialized world can imagine their everyday life without the Internet; we use it almost every waking hour. It has created previously unimaginable possibilities for keeping in touch with family and friends, searching for information, and sharing of ideas and knowledge. In recent years, the proliferation of smartphones and the concept of *cloud computing* has dramatically changed the way we use the Internet. One of the most important effects of this development is that our computers, tablets, and smartphones are mainly used as terminals, where we can access information and input commands, while the data storage and processing is located on servers in massive datacenters distributed around the world.

As microprocessor clock speeds are not increasing rapidly, the increasing demand of datacenter and supercomputer capacity is solved by parallel operation of an ever larger number of servers and processor cores [1]. While the fastest supercomputer in 2002 used 5120 cores (NEC Earth-Simulator, 36 Tflops), the fastest supercomputer as of August 2015 counts a massive 3,120,000 cores (Tianhe-2, 34 Pflops) [2]. Meanwhile, the largest datacenters in the world already span over 100,000 m² each (equivalent to 12 FIFA standard football fields) [3, 4]. This up-scaling by parallelization means that present and future datacenters and supercomputers require an internal network with enormous capacity. Since copper cables have high attenuation at high frequencies, the most promising solution is to use fiber-optic links (called optical interconnects) to connect different parts of the system. The vast majority of these links are shorter than 100 m in length [5], but as datacenters are growing larger, longer low-cost high-speed links up to 2 km will be required [6]. Energy-efficient short links (<1 m) will also be needed when optical links migrate closer to the processors (optical backplanes, on-board, and on-chip interconnects) [7, 8]. Future

exascale supercomputers, capable of 1 Exaflop per second (Exa= 10^{18}), are estimated to require an astonishing bidirectional optical interconnect capacity of 400 PB/s [7, 9]. Even if this data was to be transmitted at channel speeds as high as 40 Gbit/s, a grand total of 160 million channels would be needed for *one* exascale supercomputer. The vast interconnect bandwidth required in present and future systems creates a demand for higher-speed (>25 Gbit/s) and highly energy-efficient interconnects. This makes GaAs-based vertical-cavity surface-emitting lasers (VCSELs) well-suited transmitters for optical interconnects, with advantages such as low-cost fabrication, high-speed modulation at low power-consumption, small footprint, and high reliability [10, 11].

1.1 VCSELs in Optical Interconnects

A schematic figure of a single-channel optical interconnect, with its different parts, is shown in Figure 1.1. These are often integrated into active optical cables (AOCs), which are “plug-and-play” cables with electrical interfaces at both ends while the electro-optics are fully sealed. Today’s commercial short-reach (<300 m) optical interconnects employ GaAs-based VCSELs emitting at 850 nm. Most AOCs have several channels bundled together, such that 100 Gbit/s AOCs consist of either ten 10 Gbit/s channels or four 25 Gbit/s channels transmitted through a ribbon of multi-mode fibers (MMFs), with arrays of VCSELs and detectors at each end. VCSEL-based links commonly use direct modulation and on-off keying (OOK), where the laser output is changed between two fixed levels by modulating the applied voltage.

The MMF used in 850 nm interconnects is more expensive than single-mode fiber (SMF) because of its complex refractive index profile [12]. However, because of the larger core size (50 μm compared to SMF 8 μm), MMF offers relaxed alignment tolerances, enabling low-cost assembly and packaging of VCSEL-based transceivers. GaAs *pin* photodetectors used in 850 nm optical interconnects feature a relatively large active area for efficient coupling from the large core size MMF, which translates into a larger capacitance and consequently lower bandwidth than the smaller SMF coupled photodetectors.

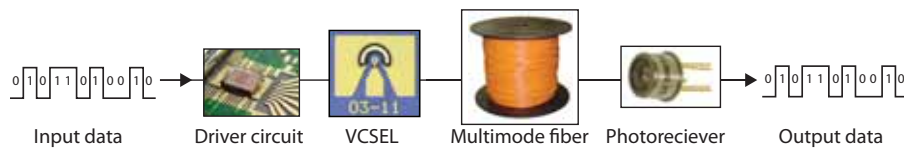


Figure 1.1: Schematic figure of a VCSEL-based optical interconnect link.

This is equivalent to a trade-off between detector responsivity and bandwidth. The photodetector is one of the limiting factors for both reach and speed of optical interconnects, making the development of faster and more sensitive photodetectors imperative.

Today, 850 nm GaAs-based VCSEL technology is used in 95% of all optical networking applications <1000 m [13]. Depending on application, three standardized data networking protocols dominate the 850 nm interconnect market; Ethernet (local area networks), Infiniband (high-performance computing, supercomputers), and Fibre Channel (storage area networks). Even though there are some differences, all work with 10-16 Gbit/s per channel over distances up to 300-550 m over OM4 MMF [14]. Higher-speed AOCs working at channel speeds of \sim 25 Gbit/s are expected in the very near future for distances up to 100 m [15], and channel speeds up to 50 Gbit/s may be seen towards the end of this decade [16]. Parallel optical transceivers with arrays of VCSELS and photodetectors, each operating at 25 Gbit/s, will soon realize commercial optical interconnects with an aggregate capacity of 400 Gbit/s in each direction [15].

1.2 High-Speed VCSELS

Increasing the bandwidth and high-speed transmission properties of GaAs-based VCSELS at 850 nm has been an important research direction since the early 1990's [17]. Already in 1997, K. Lear *et al.* demonstrated VCSELS with 21.5 GHz bandwidth, using an oxide-implanted 850 nm VCSEL [18]. The first 20 Gbit/s operation of 850 nm VCSELS was presented by IBM in 2001 [19]. It took 7 years before 30 Gbit/s was demonstrated by Finisar in 2008, using an oxide-confined VCSEL [20]. However, only two years later, P. Westbergh *et al.* at Chalmers University of Technology demonstrated 850 nm VCSELS capable of 40 Gbit/s transmission [21]. These VCSELS also broke the old bandwidth record, achieving 23 GHz by optimization of the damping characteristics [22]. Since then there has been an impressive development in VCSEL small-signal modulation bandwidth, and especially high-speed data transmission. In 2013 high-speed VCSELS from Chalmers with 28 GHz bandwidth enabled 57 Gbit/s at room temperature (RT), and 40 Gbit/s at 85°C [23, 24]. Using driver and receiver circuits with electronic equalization, the same VCSELS could transmit at 71 Gbit/s at RT [25], and 50 Gbit/s up to 90°C [26]. This is the fastest VCSEL-based link to date without the use of forward error correction (FEC). The newest generation high-speed 850 nm VCSELS from Chalmers is presented in Papers A and B. By strongly confining optical fields and carriers, a small-signal modulation bandwidth of 30 GHz was reached, which is currently the record for conventional VCSELS. Current state-of-the-art bandwidths and

Table 1.1: Current short-wavelength high-speed VCSEL records using OOK.

Group	λ [nm]	BW [GHz]/ BR [Gbit/s]	T [°C]	Year	Ref.
High bandwidth					
Chalmers	850	30	RT	2015	Paper B
UIUC ¹	980	37	RT	2015	[27]
TU Berlin	980	23	85	2014	[28]
High bit rate					
Chalmers	850	57	RT	2013	[23]
TU Berlin	980	46	85	2014	[28]
High bit rate (with equalization)					
IBM-Chalmers	850	71	RT	2015	[25]
IBM-Chalmers	850	50	90	2015	[26]

¹with coherent VCSEL array.

transmission speeds for high-speed VCSELs are summarized in Table 1.1 at both RT and 85°C.

Although 850 nm still remains the standard wavelength for commercial optical interconnects, there is a strong interest in 980-1060 nm GaAs-based VCSELs. These longer wavelengths have several inherent advantages, such as highly strained InGaAs quantum wells for higher differential gain and lower transparency carrier density, superior high-temperature performance due to deeper quantum wells, and the use of binary GaAs in the distributed Bragg reflectors (DBRs) for increased electrical and thermal conductivity [29]. In addition, the GaAs substrate is transparent at these longer wavelengths, enabling bottom emitting devices for flip-chip mounting [30], which is not possible at 850 nm. However, there are also some disadvantages compared to 850 nm VCSELs, such as higher loss in polymer waveguides [31], and higher free-carrier absorption [20]. Researchers from Technical University of Berlin (TUB) have in recent years demonstrated impressive results with their 980 nm VCSELs. A temperature-stable VCSEL design, with optimized resonance-gain offset [32], enabled bandwidths of 25 GHz at RT, decreasing only slightly to 23 GHz at 85°C [28]. These devices also have the present record for high-temperature data transmission at 46 Gbit/s. Researchers at NEC and Furukawa in Japan are at the forefront on \sim 1060 nm VCSELs [33–36]. NEC’s ion-implanted tunnel-junction VCSELs were actually the first to operate at 40 Gbit/s, already in 2007 [33]. Furukawa presented some of the earliest results on energy-efficient high-speed data transmission with VCSELs in 2011 [36, 37].

This work concerns only direct-modulation OOK, but higher-level amplitude modulation formats can potentially enable higher bit rates, at the expense of needing a larger power budget [38]. Four-level pulse amplitude modulation (4-PAM) transmission using 850 nm VCSELs has been demonstrated up to 60 Gbit/s without the use of FEC [39]. Unconventional VCSEL

structures with coupled cavities for multiple resonance peaks have recently demonstrated bandwidths exceeding 30 GHz. By tuning the photon-photon resonance peak, the modulation response can be lifted, enabling bandwidths of up to 37 GHz [27]. Data transmission experiments at 40 Gbit/s have so far been presented using this type of devices [40]. Furthermore, there is ongoing research into utilizing other techniques than intensity modulation to transmit data, such as polarization oscillation switching of spin-polarized VCSELS [41].

1.3 VCSELS for Energy-Efficient Data Transmission

Today’s widely deployed 10 Gbit/s optical interconnects typically consume 25 pJ/bit [35]. The VCSEL itself typically consumes only a few percent of this (<1 pJ/bit), with the rest being used by the driver electronics and receiver. To make future high-speed interconnects for supercomputers and datacenters feasible, the link energy consumption must be dramatically reduced to ~ 1 pJ/bit, also at higher channel speeds [7]. Even lower energies per bit may be needed as optical links migrate closer to the processors, in for instance on-board and on-chip interconnects [1, 8]. The performance of state-of-the-art energy-efficient VCSEL links is stated in Table 1.2. Researchers at IBM have demonstrated energy-efficient driver and receiver circuits in 32-nm SOI CMOS, increasing the VCSEL’s share of the total interconnect power consumption to 30-40% [42]. This makes energy-efficient high-speed VCSELS an important research direction. As seen in Table 1.2, the target performance of 1 pJ/bit was reached at 25 Gbit/s, but already at 35 Gbit/s this almost tripled to 2.7 pJ/bit due to higher driver and receiver power consumption, and increased VCSEL bias. At higher bit rates, SiGe BiCMOS circuits with equalization have been used to demonstrate impressive transmission at 40-71 Gbit/s. However, they consume quite a lot of energy at ~ 25 pJ/bit [25, 43–45]. A significant reduction in the power consumption of high-bit-rate driver and receiver circuits will be needed to enable future VCSEL links at ≥ 40 Gbit/s.

Table 1.2: Energy efficiency of full VCSEL-based links. All results are for back-to-back transmission at RT using 850 nm VCSELS.

Group	BR [Gbit/s]	Link eff.	VCSEL eff. (% of link)	Year	Ref.
32-nm SOI CMOS					
IBM-Sumitomo	25	1.0 pJ/bit	396 fJ/bit (40%)	2013	[42]
IBM-Sumitomo	35	2.7 pJ/bit	800 fJ/bit (30%)	2013	[42]
130-nm SiGe BiCMOS (with equalization)					
IBM-Emcore	40	22.3 pJ/bit	653 fJ/bit (3%)	2012	[43]
IBM-Finisar	56	23.7 pJ/bit	245 fJ/bit (1%)	2013	[44]
IBM-Chalmers	64	26.3 pJ/bit	320 fJ/bit (1%)	2014	[45]

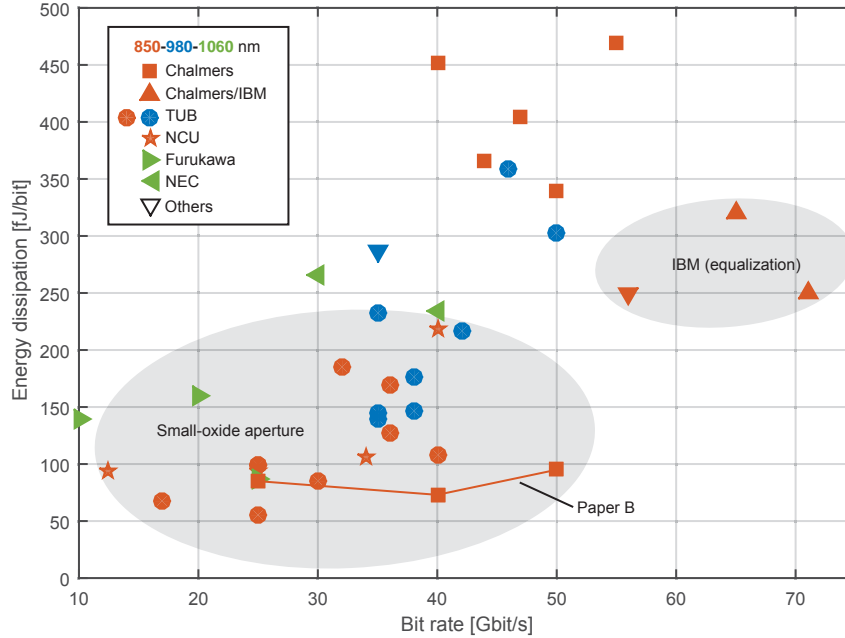


Figure 1.2: State-of-the-art VCSEL dissipated energy per bit for high-speed transmission with 850-980-1060 nm VCSELs. The colors indicate the wavelength, while the shapes indicate the affiliation. (TUB=Technical University of Berlin, NCU=National Central University, Taiwan.) [21, 23–25, 28, 34–37, 44, 45, 47–58], and Paper B.

Considering only the VCSEL, it is reasonable to assume that it may consume about 10% (100 fJ/bit) of the mentioned 1 pJ/bit target for the full interconnect. This requires VCSELs with excellent high-speed properties at low bias currents, and low resistance for low voltage. A high static wall-plug efficiency (WPE) is also beneficial, but the WPE is not a good figure of merit on its own [46]. A VCSEL's capability of energy-efficient high-speed data transmission is commonly quantified by either the energy-to-data ratio

$$\text{EDR} = \frac{V \cdot I}{BR}, \quad (1.1)$$

where V is the voltage, I bias current, and BR bit rate, or the dissipated heat-to-data ratio

$$\text{HDR} = \frac{V \cdot I - P_{\text{opt}}}{BR} = (1 - \text{WPE}) \cdot \text{EDR}, \quad (1.2)$$

where P_{opt} is the output optical power [48]. Considering only the VCSEL, the HDR is the more appropriate figure of merit, since the EDR does not take the WPE into account, while it is obvious that a higher output power would benefit the receiver energy efficiency. The EDR and HDR are given in fJ/bit in this work, but may also be stated in the equivalent unit of mW/(Tbit/s).

Figure 1.2 shows the HDR from the most energy-efficient and highest-speed VCSEL transmission experiments, and the current records at RT and 85°C are summarized in Table 1.3. Researcher from TUB have shown impressive energy-efficient high-speed VCSELS at 850 and 980 nm in recent years, using VCSELS with small oxide apertures of 2-4 μm [28, 46–48, 54, 56, 59]. Even though small-oxide-aperture VCSELS do not have the highest WPE ($\sim 20\%$ compared to $\sim 30\%$ for larger oxide apertures), they have excellent high-speed properties at low bias currents because of the small active and modal volumes (see Chapter 3) [46]. The most prominent results from TUB are HDRs of 56 fJ/bit at 25 Gbit/s and 108 fJ/bit at 40 Gbit/s. While the result at 25 Gbit/s is still a record, our latest VCSELS enabled sub-100-fJ/bit transmission at 25–50 Gbit/s, with 73 fJ/bit at 40 Gbit/s, and even 95 fJ/bit at 50 Gbit/s, see Table 1.3 and Paper B. This demonstrates that VCSELS are capable of energy-efficient operation at 40 and 50 Gbit/s without the use of power-hungry equalization techniques. At 1060 nm, Furukawa has demonstrated energy-efficient operation with <100 fJ/bit dissipated energy at 25 Gbit/s [35].

As seen in Figure 1.2, the record dissipated energy per bit lies within the range of 50–100 fJ/bit from 10–50 Gbit/s. Even low bit-rates of 10 Gbit/s have HDRs similar to the record at 50 Gbit/s. The reason is that HDR is given in terms of *energy* per bit; for equal HDR at 25 and 50 Gbit/s, the VCSEL must therefore consume about half as much *power* at 25 Gbit/s as 50 Gbit/s. Even at low bit rates, the VCSEL power consumption must still be high enough to bias the VCSEL at a reasonable point above the threshold.

Table 1.3: Current record VCSEL HDRs for high-speed data transmission.

Group	λ [nm]	BR [Gbit/s]	T [°C]	HDR [fJ/bit]	Year	Ref.
TU Berlin	850	25	RT	56	2012	[59]
Chalmers	850	40	RT	73	2015	Paper B
Chalmers	850	50	RT	95	2015	Paper B
IBM-Chalmers ¹	850	71	RT	250	2015	[25]
TU Berlin	980	35	85	139	2014	[56]
TU Berlin	980	38	85	177	2014	[54]

¹using driver circuits with equalization.

1.4 Longer-Reach Optical Interconnects

Long-reach optical interconnects for ~ 500 - 2000 m currently employ InP-based 1310 nm distributed feedback laser (DFB) and SMF [6]. Even though MMF is more expensive per meter than SMF, the low-cost fabrication of VCSELs-based transceivers and energy-efficient direct modulation could still make VCSEL-based MMF links justifiable for long-reach optical interconnects by using 850 nm VCSELs.

The launching and propagation of the VCSEL output signal through MMF is a complex process. First, the coupling of the VCSEL modes into the MMF is not a trivial problem. Depending on launch conditions such as angle, offset from fiber center, and spot size, each VCSEL mode can excite several different fiber modes, referred to as mode groups. Second, there are three main fiber-related effects that may limit the transmission distance over MMF; fiber loss, chromatic dispersion, and modal dispersion. The simplest, but often not limiting, is the absorption loss during propagation, which is 2.3 dB/km at 850 nm for OM4 MMF. However, for commercial implementation of long-reach MMF links, it will be important to have a large received power in order to have an adequate power budget for the link. The separation in wavelength of the transverse modes emitted by the VCSEL cause a broadening of the signal during propagation in the MMF by chromatic dispersion. In addition, the different modes in the fiber have different propagation constants, giving rise to modal dispersion. During modulation, the relative optical power in the VCSEL modes fluctuate by mode competition. This causes a random fluctuation in the effects of modal dispersion and possible mode-selective losses and coupling, collectively referred to as mode-partition noise. In highly multimode VCSEL links the mode-partition noise is reduced by the averaging over many modes, but lasers with a few modes can suffer greatly. Due to the absence of other modes, single-mode lasers do not experience any significant mode-partition noise. The standard OM3 and OM4 MMFs have optimized graded-index profiles in order to minimize the modal dispersion at 850 nm, making chromatic dispersion the dominating effect [60].

As a rule of thumb, at 10 Gbit/s, chromatic and modal fiber dispersion will significantly distort the signal for transmission distances exceeding 300 m of OM4 MMF, causing inter-symbol-interference and bit errors [61]. At higher bit rates, the shorter bit slot makes the link even more sensitive to dispersion effects, and the maximum transmission distance decreases even further. The highest transmission speed across 100 m of MMF is 43 Gbit/s (60 Gbit/s using equalization) [23, 45]. In addition, commercial 850 nm AOCs are limited to 100 m at 25 Gbit/s [62]. However, quasi-single-mode VCSELs with reduced spectral width, and thereby reduced effects of dispersion, may transmit at high

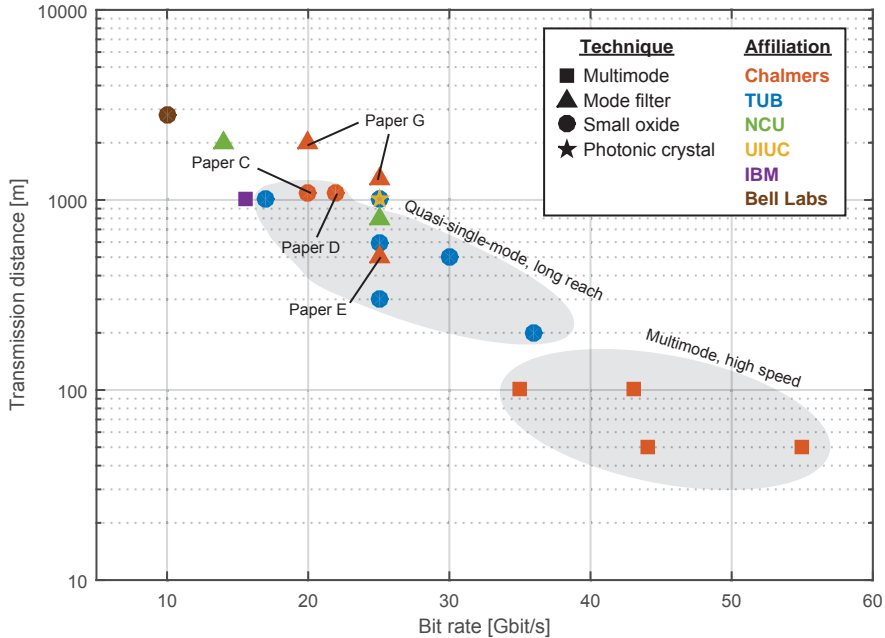


Figure 1.3: State-of-the-art high-speed long-distance transmission using 850 nm VCSELs with OOK and multimode fiber. All devices, except the photonic crystal VCSEL, are oxide confined, and only the mode filter and photonic crystal VCSELs have special mode-selective structures. All links perform at bit-error-rate $<10^{-12}$, except the IBM link where only open eyes are shown. (TUB=Technical University Berlin, UIUC=University of Illinois at Urbana-Champaign, NCU=National Central University.) [21, 23, 24, 49, 51, 63–70], and Papers C, D, E and G.

bit rates over much longer distances.

Giaretta *et al.* [63] and Pepeljugoski *et al.* [64] demonstrated already in 2000 and 2002, respectively, that 850 nm VCSEL links at >10 Gbit/s over >1 km of MMF are feasible by using low-spectral-width VCSELs. As a matter of fact, Giaretta held the record for the highest bit-rate-distance product with 28.2 Gbit·km/s (10 Gbit/s over 2820 m) until 2014 (Paper G). Increasing VCSEL bandwidths, and larger datacenters, have sparked an interest in extending the reach of high-speed (>20 Gbit/s) VCSEL MMF links. The 2011 paper [65] by Fiol *et al.* from TUB demonstrating 25 Gbit/s over 300 m of OM3 fiber started the race. Only two years later researchers from Chalmers University of Technology (Papers C and D), TUB [51], and University of Illinois, Urbana-Champaign (UIUC) [70] had demonstrated ≥ 25 Gbit/s links over ≥ 1 km of

MMF, see Figure 1.3. This was possible by reducing the spectral width of recently developed high-speed VCSELs.

The most common approach is to use a small oxide aperture of ~ 3 μm , as used in [51, 66, 68] and Papers C and D. The optical guiding can also be modified by etching a photonic crystal in high-speed VCSELs as demonstrated by Tan *et al.* at UIUC [70]. Photonic crystal VCSELs can have excellent spectral properties and low resistance, but increased scattering loss reduces the output power and efficiency. The technique of using a surface-relief mode filter to reduce the spectral width of VCSELs is applied in Papers E and F, enabling transmission at 25 Gbit/s over 500 m. A further development of the mode-filter fabrication process improved this to 25 Gbit/s over 1300 m of OM4 fiber and 20 Gbit/s over 2000 m, setting the still standing bit-rate-distance-product record of 40 Gbit·km/s for OOK 850 nm VCSEL links (Paper G). The mode-filter technique allows for a larger oxide aperture, with potentially lower differential resistance, and higher output power to compensate for propagation loss in long-reach links. Shi *et al.* from National Central University, Taiwan (NCU), used a combination of mode filtering by Zn-diffusion and small oxide relief (where the oxidized layer is completely removed for low capacitance) to achieve quasi-single-mode operation, enabling 14 Gbit/s over 2 km, and 25 Gbit/s over 800 m [49, 67].

Higher-level amplitude modulation formats can potentially enable longer-reach transmission, but require a larger power budget [38], or complex circuits for FEC. 4-PAM has been demonstrated at 12.5 Gbit/s over 600 m of fiber [71], and 48.7 Gbit/s over 200 m using FEC [72]. The current record bit-rate-distance-product at 850 nm is 107.6 Gbit·km/s, and was achieved using discrete multitone modulation and FEC [73], while we hold the record for direct modulation OOK (Paper G). Future long-reach interconnects may also use VCSELs at 980 and 1060 nm, which have the advantage of significantly smaller loss and chromatic dispersion in the silica used in the optical fibers [74]. While the standardized OM4 MMF is optimized for a low modal dispersion around 850 nm, fiber optimized for higher modal bandwidth, broader wavelength spans, and longer wavelengths are currently being developed [75, 76]. Another competing technology is longer-wavelength VCSELs at 1310 or 1550 nm, where the use of SMF avoids most of the effects of dispersion. Directly modulated InP-based 1550 nm VCSELs have shown close-to error-free transmission at 40 Gbit/s over 1 km of SMF [77].

1.5 Multiplexing in Optical Interconnects

Besides higher single-channel speed, energy-efficiency, and longer-reach, there is an additional need for a denser integration of transceivers and fibers. Supercomputers are already approaching the point where there is no room for

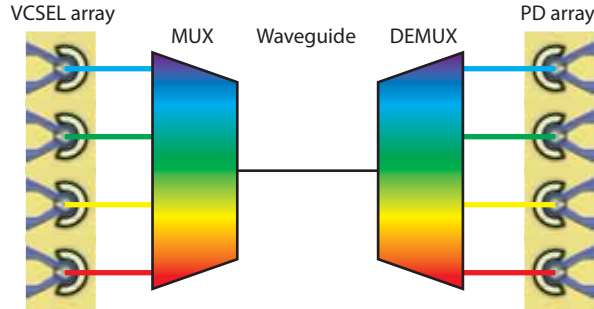


Figure 1.4: Simple schematic figure of a 4-channel VCSEL-based WDM optical interconnect.

any more interconnect ports on the switch circuit boards, and Gbit/s/mm (of edge space) or Gbit/s/mm² are becoming important figures of merit [78]. Some form of multiplexing of the interconnect channels could be the solution. Although AOCs already use a crude form of spatial-division multiplexing with VCSEL/detector arrays and fiber ribbons, everything can be made smaller by using multicore fibers (MCFs) with several closely spaced cores in one fiber. Dense VCSEL arrays, with a circular layout fitting to a 6-core MCF, have recently demonstrated transmission at 240 Gbit/s (6x40 Gbit/s), without any cross-talk penalty [79, 80].

Another solution is to use wavelength-division multiplexing (WDM) to transmit several channels at different wavelengths in each fiber core, see Figure 1.4. This could enable the interconnect capacity needed for future supercomputers without needing an unfeasible number of fibers [7]. In addition, since MMF is more expensive per unit length than SMF, WDM could also make short-wavelength interconnects cost-effective for longer distances ($\sim 500\text{-}1000\text{+m}$) [6, 78]. Short-wavelength WDM for optical interconnects faces numerous technological challenges, foremost the need for energy-efficient, low-cost, and small-footprint VCSEL arrays, and low-loss multiplexers (MUX) and demultiplexers (DEMUX). Demultiplexing is a major challenge since optical interconnects must operate from room temperature to 85°C without active cooling, leading to a thermal wavelength drift of the VCSELs of around 4 nm (see Section 2.6). WDM links have been demonstrated using short-wavelength VCSELs with different emission wavelengths fabricated from different wafers [81, 82]. However, this complicates the packaging of the transceivers [83]. WDM in optical interconnects would greatly benefit from the development of monolithically integrated multi-wavelength VCSEL arrays, but these are intrinsically difficult to realize, as the resonance wavelength of the VCSEL cavity is set dur-

ing the epitaxial growth. This is further discussed in the second part of this thesis that demonstrates multi-wavelength VCSEL arrays using high-contrast gratings (HCGs). Eventually, transmission over a ribbon of MCFs, with several wavelengths in each core, using high-speed VCSELs, and advanced drivers and receivers, could enable 10's of or even 100 Tbit/s capacity in a single AOC.

As of today, the only commercial short-wavelength WDM product on the market is Cisco's 40 Gbit/s BiDi transceivers that transmits counter-propagating wavelengths at 832 and 918 nm in each fiber using VCSELs fabricated from two different wafers [84]. Using a fiber pair, 2x20 Gbit/s is transmitted in each direction for a total bi-directional capacity of 40 Gbit/s. The broad commercial breakthrough for short-wavelength WDM is yet to come, but there is significant industrial interest in short-wavelength coarse WDM, and WDM in the 860-1100 nm range is currently being discussed in the IEEE 400 Gigabit Ethernet Task Force [85].

1.6 Scope and Outline of Thesis

The focus of this work has been on several important aspects of VCSELs for future optical interconnects. The first part concerns conventional 850 nm VCSELs for longer-reach and energy-efficient data transmission at high data rates. Chapter 2 introduces the VCSEL fundamentals. It is followed by Chapter 3 with a more detailed discussion on VCSEL dynamics and high-speed VCSEL design. Chapter 4 describes the two different quasi-single-mode VCSEL approaches used to enable longer-reach transmission; a small oxide aperture or an integrated mode filter. The VCSEL fabrication methods are described in Chapter 5. The second part of the thesis presents the design, fabrication, and experimental results for 980 nm multi-wavelength VCSEL arrays using HCGs. Chapter 6 describes the basics of HCGs and the design of HCG-VCSEL multi-wavelength arrays. The grating fabrication process is discussed in Chapter 7, followed by experimental results in Chapter 8. An outlook and future directions, for both parts, are provided in Chapter 9. The results from the work on which this thesis is based are finally presented in the appended Papers A-H, which are summarized in Chapter 10.

Chapter 2

VCSEL Fundamentals

As the name indicates, vertical-cavity surface-emitting lasers (VCSELs) emit light normal to the surface by lasing in a vertical cavity, as seen in Figure 2.1a. The cavity is formed by two highly reflective DBRs ($\sim 99.5\%$), with a forward biased pn -junction sandwiched between them providing optical gain. In contrast to the VCSEL, the earlier developed edge-emitting Fabry Perot laser has a horizontal resonator with cleaved semiconductor-air facets acting as mirrors, see Figure 2.1b. This means that the wafer must be cleaved to enable testing and screening, while VCSELs may be tested on-wafer during production and integrated into 2D arrays. VCSELs are sometimes referred to as micro-cavity lasers and have several significant advantages because of their small cavity

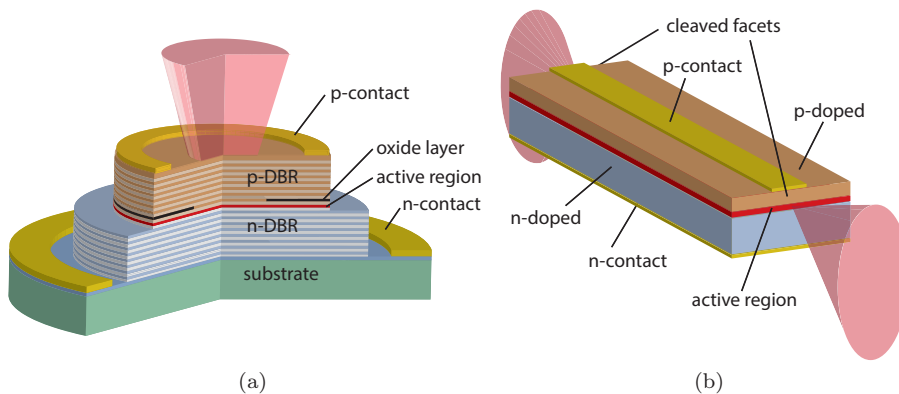


Figure 2.1: (a) Cut-through VCSEL sketch. (b) Edge emitting stripe laser.

size, such as low threshold currents and excellent high-speed properties at low power consumption.

2.1 History of VCSELs

The concept of a vertical-cavity semiconductor laser was first proposed in 1977 by Professor K. Iga from Tokyo Institute of Technology, who two years later also demonstrated the first VCSEL, lasing under pulsed operation at 77 K [86, 87]. The first VCSEL more resembled a “vertical edge emitter” with a relatively long cavity and metal-coated mirrors. The first reports on room temperature operation of VCSELs were published in 1989 [88, 89]. During the 1990’s VCSEL research really took off and the first commercial VCSELs came on the market in the middle of the decade. VCSEL-based short-reach fiber-optic links for data communication were introduced in 1996 [90]. Today 850 nm GaAs-based VCSEL technology is extensively utilized in short-reach optical communication links, with 95% of all optical networking applications <1000 m using multimode fiber and 850 nm VCSELs [13]. The largest volume market for VCSELs is, however, in optical computer mice where 850 nm VCSELs are used to track movement on uniform surfaces with higher resolution and speed than the earlier light-emitting diode (LED) optical mice [17]. In 2013, the total VCSEL production was around 100 million devices per year, with the price of a computer-mouse 850 nm VCSEL approaching \$0.10 [17]. VCSEL production output is increasing, with larger wafer sizes being used to scale up production. In March 2014 IQE delivered the first 6" epitaxial VCSEL wafers which can accommodate up to 300,000 VCSELs per wafer [91].

2.2 Cavity and Mirrors

The distributed Bragg reflector (DBR) mirrors comprise a stack of alternating high and low refractive index material, where the light is partially reflected at each interface. If the optical thickness of each layer equals a quarter wavelength, this wavelength will experience the Bragg condition, meaning that all reflections add up in phase leading to a large reflection for the whole stack, see Figure 2.2a. The peak reflectivity depends on the number of DBR pairs and the refractive index difference Δn between the high- and low-index material, while the width of the reflection stopband mainly depends on Δn [92]. DBRs are commonly fabricated using either dielectric or epitaxial material systems. Dielectric DBRs may achieve a high reflectivity with <10 pairs due to the high index contrast (e.g. SiO₂/TiO₂ with $\Delta n = 0.90$ at 850 nm [93]), while epitaxial DBRs need ~20-30 pairs because of the lower index contrast (e.g. Al_{0.90}Ga_{0.10}As/Al_{0.12}Ga_{0.90}As with $\Delta n = 0.46$ [94]). On the other hand epitaxial DBRs can be doped and often function as current spreaders to achieve

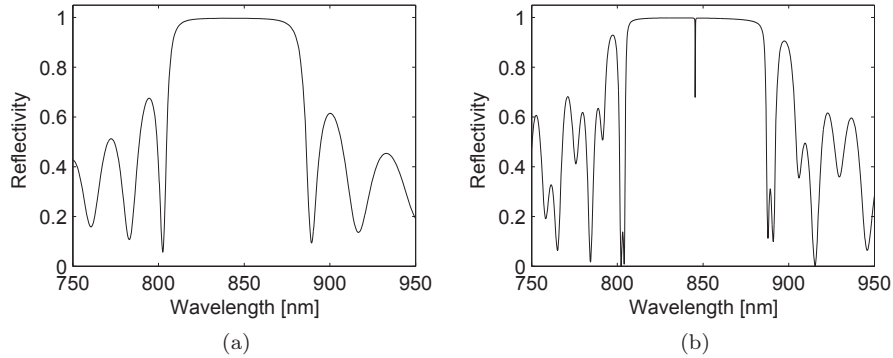


Figure 2.2: Calculated reflectivity spectra for (a) a VCSEL top DBR with 23 pairs of $\text{Al}_{0.90}\text{Ga}_{0.10}\text{As}/\text{Al}_{0.12}\text{Ga}_{0.88}\text{As}$ and (b) a full VCSEL cavity. The single narrow longitudinal resonance is seen at 845 nm.

a uniform injection of carriers into the active region. For the mirror where no transmission is required, a hybrid DBR may be used where the DBR is covered with gold or copper to increase reflectivity. The metal may also function as a heat sink and a contact for current injection. A completely different type of mirror, based on a high-contrast grating (HCG), is used in the second part of this thesis (see Chapter 6). GaAs-based VCSEL designs commonly feature epitaxial DBRs in the mature AlGaAs material system.

The VCSEL has a short cavity, of length L_{cav} , sandwiched between the two DBRs. However, the effective cavity length L_{eff} is longer, due to the penetration¹ of the optical field into the DBRs [92] (Figure 2.3). The longitudinal resonance of the VCSEL cavity is set by the phase condition; that the optical field must repeat itself after one round-trip in the cavity. Therefore, twice the effective optical length $L_{eff}n_{eff}$ must equal an integer number m of wavelengths λ_0 according to

$$2L_{eff}n_{eff} = m\lambda_0 \Rightarrow \lambda_0 = \frac{2L_{eff}n_{eff}}{m}. \quad (2.1)$$

Because of the short cavity length, only one longitudinal mode falls within the gain bandwidth, making the device inherently single longitudinal mode (though usually not single transverse mode), see Figure 2.2b.

¹For penetration depths into the top and bottom DBRs of L_p^T and L_p^B , the effective cavity length is $L_{eff} = L_p^T + L_{cav} + L_p^B$.

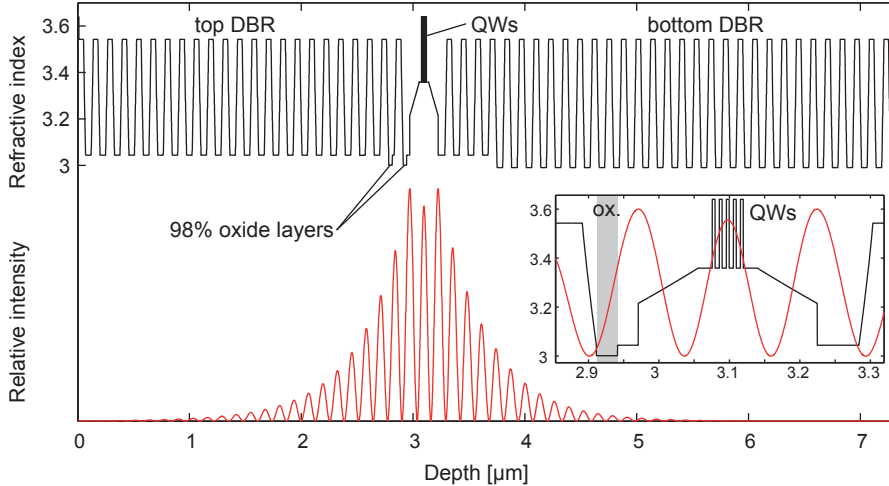


Figure 2.3: Refractive index profile and simulated standing wave of the optical field inside a VCSEL cavity with a cavity length of $3/2\lambda$, and a double oxide layer above the active region. The inset shows the overlap of the standing wave with the quantum wells (QWs) and the nearest oxide layer (ox.). The substrate is to the right.

2.3 Active Region

The active region provides the optical gain. During lasing the modal gain must balance the optical losses according to

$$g_{th} = \frac{1}{\Gamma} \left(\alpha_i + \frac{1}{2L_{eff}} \ln \frac{1}{R_m^T R_m^B} \right), \quad (2.2)$$

where g_{th} is the threshold gain, Γ the optical confinement factor representing the fraction of the standing wave that overlaps with the active region, α_i the internal optical loss (due to free-carrier absorption and diffraction loss), and R_m^T and R_m^B are the top and bottom mirror reflectivities. In semiconductor lasers the optical gain by stimulated emission is achieved by injecting carriers into a forward biased pn -junction. Electrons and holes accumulate in the conduction and valence band respectively, which under high enough injection gives rise to a population inversion and thereby optical gain. The first semiconductor laser, demonstrated in 1962, had an active region consisting of a GaAs homojunction and could only operate in pulsed mode at 77 K because of the high band-to-band absorption [95]. Today the active region usually consists of a pin -heterojunction with quantum wells (QWs) situated in the lower-bandgap intrinsic layer. The QWs trap the carriers, providing a high

carrier density and a good spatial overlap between the electron and hole wave functions. Since the stimulated emission process is related to the optical field strength, the QWs are placed at an antinode of the optical field to achieve a high gain, see Figure 2.3. State-of-the-art high-speed 850-1060 nm VCSELs use strained InGaAs QWs which reduces the density of states, meaning that fewer carriers are required to reach a certain gain (i.e. a larger differential gain) [96]. GaAs-based VCSELs with highly strained InGaAs QWs have been demonstrated up to ~ 1300 nm [97], but beyond ~ 1060 - 1100 nm the increasing QW strain leads to concerns regarding reliability.

2.4 Optical and Electrical Confinement

The DBRs confine the optical field in the longitudinal direction (Figure 2.3), but it must also be confined in the transverse direction. Furthermore, the electrical current must be confined to pump only active material overlapping with the lasing modes. In most VCSEL designs the electrical and optical confinement originate from the same feature. The first VCSELs consisted of an etched air post mesa, see Figure 2.4a. The refractive index step from semiconductor to air provides index guiding, confining the optical field in the transverse direction. Although simple, this design has several issues such as high thermal resistance because of the surrounding air, large scattering losses from rough sidewalls, and trouble with placing large enough top contacts for low resistance while avoiding absorption losses from the metal. A further development is the buried heterostructure VCSEL seen in Figure 2.4b. By regrowing semi-insulating semiconductor material around the etched mesa, problems with thermal resistance and losses are avoided, but the regrowth process is challenging. The first commercial VCSELs instead used proton implantation, see Figure 2.4c. Protons are implanted deep into the top DBR, making the material insulating and forming the current aperture. The implanted material does not form a direct index step for transverse optical confinement. However, as the center of the waveguide heats up during operation, the refractive index increases, creating a refractive index gradient. This effect, referred to as thermal lensing, confines the optical field, but also leads to bias-dependent unstable modal properties. In addition, scattering of the protons during implantation, due to the large penetration depth into the top DBR, makes it difficult to fabricate small-aperture devices.

Stable modal properties are obtained by including a built-in index step that is sufficiently large compared to thermal lensing, gain guiding, and the plasma effect (decreasing refractive index with increased carrier concentration). One approach is to use a selectively oxidized layer forming an oxide aperture, see Figure 2.4d. A high Al-content layer (usually $\text{Al}_{0.98}\text{Ga}_{0.02}\text{As}$) is positioned in

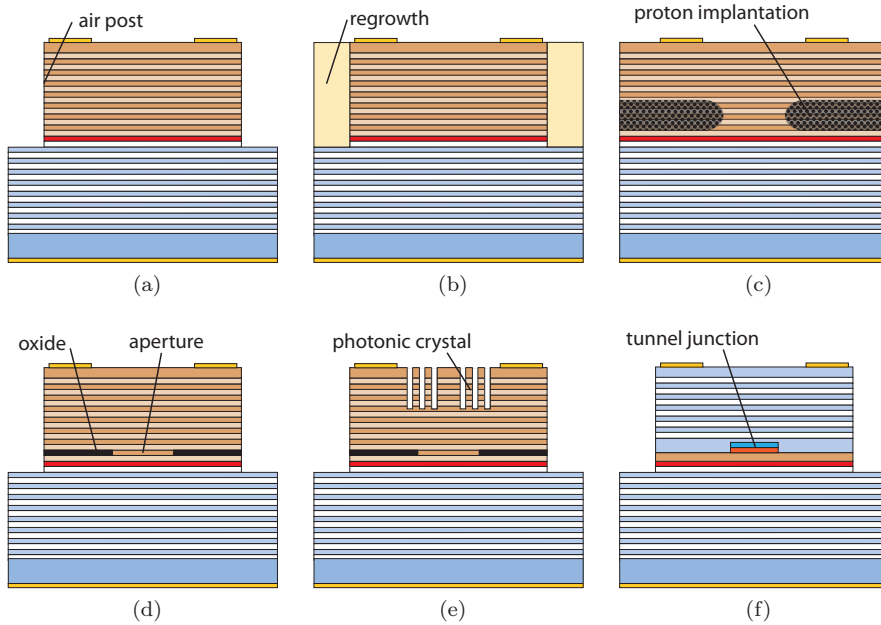


Figure 2.4: Different electrical and optical confinement methods: (a) etched air post, (b) regrown mesa, (c) proton implantation, (d) oxide aperture, (e) photonic crystal and (f) buried tunnel-junction.

the DBR close to the active region. When the etched mesa side is exposed to hot water vapor, this layer will oxidize to form an insulating oxide with reduced refractive index. This creates a current aperture that simultaneously provides the transverse optical guiding. The oxidation rate is strongly dependent on the Al-content, and the highest Al-content layer will therefore form the smallest oxide aperture [98]. To avoid scattering losses and too large index guiding, the oxide layer is usually positioned close to a node of the optical field [99], see Figure 2.3. Multiple oxide layers may be used in order to reduce mesa capacitance to mitigate parasitic bandwidth impairments (as further discussed in Section 3.3). Oxide-aperture VCSELs are the most common GaAs-based VCSELs today, and it is also the confinement scheme used in this work.

Lateral current spreading and diffusion in the region between the oxide aperture and QWs can lead to carrier leakage, accompanied by a reduction of the internal quantum efficiency² and an increased threshold current. A strong lateral confinement of carriers is therefore desired for energy-efficient VCSELs.

²The portion of injected carriers that recombine by stimulated emission in the QWs.

Since holes have lower mobility than electrons, the oxide aperture is typically placed on the p -side to confine the slower holes, as this also prevents electrons from spreading outwards due to the requirement of charge neutrality. Current spreading can be reduced by using un-doped intrinsic material between the oxide aperture and the QWs. This will not have a negative impact on the carrier transport into the QWs if a properly designed short separate confinement heterostructure (SCH) is used [100]. Current spreading can be especially troublesome if there is any doped material between the oxide aperture and the QWs [24]. A strong confinement of the injected carriers is demonstrated in Paper A by positioning the oxide layers as close to the QWs as possible; in the first field minima of the standing wave on either side of the QWs. This approach has previously demonstrated low current spreading and diffusion [101]. The resulting high internal quantum efficiency and low threshold currents enabled high-speed transmission at record-high energy efficiencies (Paper B).

Decoupling of the electrical and optical confinement, in order to tailor the optical properties of the VCSEL waveguide, can be achieved by etching a 2D photonic crystal into the top DBR of an oxide-confined or proton implanted VCSEL, see Figure 2.4e. In addition to increased design and processing complexity, the photonic crystal structure increases optical scattering losses, leading to lower output power and larger threshold current [17]. For long-wavelength InP-based VCSELs emitting at 1.3 and 1.55 μm , a buried tunnel junction is used for electrical and optical confinement since no high-quality oxide exists in this material system, see Figure 2.4f [102]. This technique is not commonly used for electrical and optical confinement in GaAs-based VCSELs because of the difficulty to design effective tunnel junctions, the complex regrowth process required, and the excellent properties of oxide-confined VCSELs.

2.5 Spectral Characteristics

High-speed VCSELs usually have the shortest possible cavity lengths of $1/2\text{-}\lambda$ or $3/2\text{-}\lambda$, since this enhances the modulation bandwidth (Section 3.1). Because of the short cavity, VCSELs are inherently single longitudinal mode as only one longitudinal mode falls within the gain bandwidth. However, due to the large lateral dimensions (oxide aperture diameter $\geq 10\lambda$), the VCSEL cavity often supports several transverse modes. The spectral characteristics of the VCSEL can be analytically investigated using an effective index method [103], where the radial refractive index step is modeled as a parabolic refractive index profile according to

$$n^2(r) = \begin{cases} n_c^2(1 - 2\Delta r^2/a^2) & , r \leq a \\ n_s^2 = \text{const} & , r > a \end{cases} \quad \text{with} \quad \Delta = \frac{n_c^2 - n_s^2}{2n_c^2} \approx \frac{n_c - n_s}{n_c} \quad (2.3)$$

where r is the radial distance, a the radius of the oxide aperture, n_c the core effective refractive index, and n_s the effective index of the surrounding oxide region. It should be noted that although Equation 2.3, strictly speaking, describes a thermally guided VCSEL (e.g. an proton-implanted VCSEL), it may be used to approximate an oxide-confined VCSEL [17, 103]. The advantage is that this index profile yields analytical expressions for the spectral characteristics, which are useful for understanding the VCSEL modal properties. By solving the wave equation in this circular symmetric structure, the near-field intensity of the transverse modes becomes

$$S_{lp}(r, \Phi) \propto |E_{lp}(r, \Phi)|^2 \propto \left(\frac{2r^2}{\omega_0^2}\right)^l \left[L_{p-1}^{(l)}\left(\frac{2r^2}{\omega_0^2}\right)\right]^2 \begin{cases} \cos^2(l\Phi) \\ \sin^2(l\Phi) \end{cases} \exp\left(\frac{-2r^2}{\omega_0^2}\right), \quad (2.4)$$

where E is the optical field strength, ω_0 the $1/e^2$ radius, L_{p-1}^l the l^{th} generalized Laguerre polynomial of order $(p-1)$, and Φ the azimuthal angle. The modes are referred to as linearly polarized LP_{lp} modes with intensity distribution as shown in Figure 2.5. For $l > 0$ the sin and cos factors represent two different orthogonal states rotated $90^\circ/l$ with respect to each other. Furthermore, every mode has two orthogonal polarization states with the electric field oscillating perpendicular to the propagation direction. Therefore, the Gaussian-shaped fundamental mode LP_{01} has two polarization states, while the higher order modes with $l > 0$ have four states per LP_{lp} mode. The wavelength λ_{lp} of mode LP_{lp} differs the fundamental longitudinal mode λ_0 as

$$\lambda_{lp} = \lambda_0 \left[1 - (2p + l - 1) \frac{\sqrt{\Delta}}{\sqrt{2\pi}} \frac{\lambda_0}{n_c a} \right], \quad (2.5)$$

which shows that modes with the same mode index $m = 2p + l - 1$ have the same emission wavelength [103]. From Equation 2.5 the mode spacing between adjacent mode index groups is

$$\Delta\lambda = |\lambda_m - \lambda_{m+1}| = \frac{\sqrt{\Delta}}{\sqrt{2\pi}} \frac{\lambda_0^2}{n_c a} \propto \frac{\sqrt{\Delta}}{D_{ox}}, \quad (2.6)$$

where $D_{ox} = 2a$ is the oxide aperture diameter. The order and spacing of the modes agree well with the measured spectrum and near-field images in

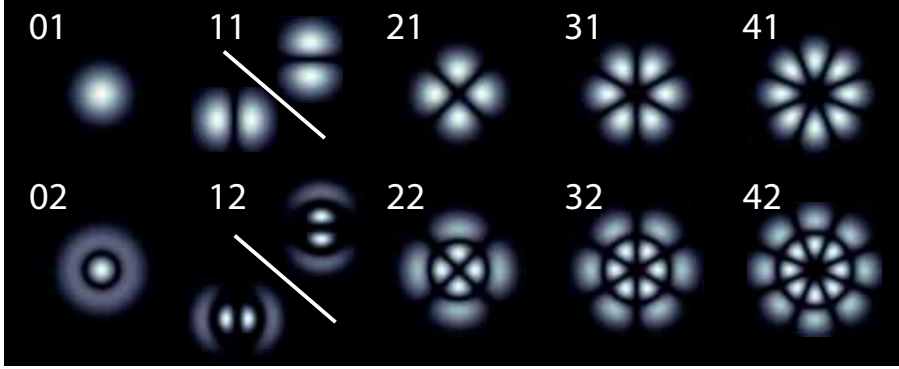


Figure 2.5: Transverse intensity distributions of the lowest order LP_{lp} modes plotted from Equation 2.4. LP_{11} and LP_{12} exemplify the rotated polarization states (cos and sin) which exist for $l > 0$.

Paper F. The number of guided modes is determined from the normalized frequency

$$V = \frac{2\pi a}{\lambda} \sqrt{n_c^2 - n_s^2}. \quad (2.7)$$

Just like a step-index SMF, the waveguide is single mode if $V < 2.405$ [104]. For large V the number of guided transverse modes can be estimated by

$$M \approx \frac{V^2}{4}. \quad (2.8)$$

These equations are useful to gain an understanding of the VCSEL transverse modes. But in reality they are far too simple to describe the complicated interplay between guiding, gain and loss in a VCSEL. In order to quantify and compare different VCSELs, the communication standards usually specify a maximum root-mean-square (RMS) spectral width, which is calculated according to

$$\Delta\lambda_{RMS} = \sqrt{\sum_{i=1}^N \frac{P_i}{P_{tot}} (\lambda_i - \langle\lambda\rangle)^2}, \quad \langle\lambda\rangle = \sum_{i=1}^N \frac{P_i}{P_{tot}} \lambda_i, \quad P_{tot} = \sum_{i=1}^N P_i, \quad (2.9)$$

where N is the number of data points of the measured spectrum, P_i is the power of point i at λ_i , and P_{tot} is the total optical power. Since the VCSEL spectrum consists of few peaks with an asymmetric envelope, the use of the RMS width to quantify VCSEL spectral width can be questioned, especially

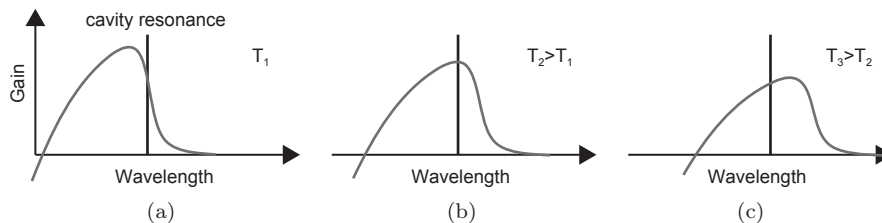


Figure 2.6: Resonance gain peak detuning with increasing temperature.

for quasi-single-mode lasers. It is, however, a simple measurement, which is used to set VCSEL requirements in all transmission standards.

2.6 Thermal Properties

Energy-efficient high-speed VCSELs typically have wall-plug efficiencies of around 25-35% ([46] and Paper A), while the remaining $\sim 70\%$ of the supplied dc power is dissipated as heat inside the device by resistive Joule heating, non-radiative recombination, and internal optical absorption. The combination of these heat sources cause a significant increase in internal device temperature with increasing bias current. At a certain point a runaway process is triggered, where the high temperature leads to an accelerating reduction in internal quantum efficiency, mainly due leakage of carriers from the QWs [100], causing a rapid increase in internal temperature [105]. This, together with an increase in threshold current due to the reduced internal quantum efficiency and gain, cause a saturation in photon density and output power. This thermal rollover occurs at active region temperatures of around 100°C in our high-speed VCSELs [105] (for ambient temperature at RT). The VCSELs in commercial optical interconnects must operate flawlessly at ambient temperatures up to 85°C , making thermal management in VCSELs critical.

One important parameter affecting the thermal behavior of the VCSEL is the alignment of the gain peak and the cavity resonance. Edge emitting Fabry-Perot lasers with closely spaced longitudinal modes always lase at the gain peak. However, since VCSELs only have one longitudinal mode, its position with respect to the gain peak can be engineered. This separation is called the detuning³. Due to thermal expansion and temperature-dependent

³Calculated as $\Delta\lambda = \lambda_{gain}^{peak} - \lambda_{cav}$. It should be noted that the gain peak-resonance detuning and photoluminescence (PL)-resonance detuning are often confused. They are not the same as the gain peak is located about 15 nm red-shifted from the PL peak for wavelengths around 850 nm.

refractive index of the VCSEL cavity, the resonance wavelength is red-shifted at $0.06 \text{ nm}/^\circ\text{C}$ with increasing temperature [106]. Meanwhile, the peak of the QW gain is red-shifted at $0.32\text{-}0.33 \text{ nm}/^\circ\text{C}$ due to bandgap shrinkage [107]. As the gain peak is red-shifted faster, it will eventually outrun the cavity resonance, leading to a reduced material gain and increasing threshold current at high temperatures (Figure 2.6). This can be compensated by an initial negative detuning. As the temperature is increased, the improved overlap of the gain and resonance compensates for the temperature-induced reduction of gain, and enables low thresholds even at high operating temperatures, as illustrated in Figure 2.6. A large negative detuning at RT can enable lasing at ambient temperatures well above 100°C [108]. The impact of thermal effects on the VCSEL dynamics is discussed in Section 3.2.

Chapter 3

VCSEL Dynamics

For high-speed data transmission using direct modulation, the VCSEL output power should react rapidly to changes in bias current or voltage. However, an electron-hole pair takes some time before recombining (differential carrier lifetime), and the generated photon takes some time to leave the cavity (photon lifetime¹). By this simple example, it is clear that a VCSEL can not be modulated infinitely fast. However, properly designed VCSELs can reach very high modulation bandwidths at low bias currents, because of the strong interaction between the injected carriers and the photons in the small VCSEL cavity. The complete dynamic behavior of a VCSEL is a complex interplay of intrinsic, parasitic, and thermal properties, and is therefore challenging to accurately model [109]. This thesis work has been concerned with experimental analysis of high-speed VCSELs in Papers A to G. The first part of this chapter describes the small-signal intrinsic dynamics of the VCSEL. It is followed by a discussion of thermal and parasitic effects on the dynamics, combined with various implications for the design of high-speed VCSELs. Finally, the measurement methods used for the small-signal modulation response measurements and data transmission experiments are presented.

3.1 Intrinsic Dynamics

The intrinsic dynamics of semiconductor lasers are governed by the resonant interaction between the photons in the lasing modes and the injected electron-hole pairs in the active region. This can be described by the rate equations [92]:

¹The photon is either transmitted through a mirror or lost by absorption or scattering.

$$\frac{dN}{dt} = \frac{\eta_i I}{qV_a} - (AN + BN^2 + CN^3) - v_g GS_m, \quad (3.1)$$

$$\frac{dS_m}{dt} = \Gamma v_g GS_m - \frac{S_m}{\tau_p} + \Gamma \beta BN^2, \quad (3.2)$$

where N is the excess carrier density in the active region, η_i the internal quantum efficiency, I the bias current, q the elementary charge, V_a the active region volume², A the Shockley-Read-Hall recombination coefficient³, B the radiative recombination coefficient, C the Auger recombination coefficient, v_g is the group velocity, G the active region gain per unit length, S_m the photon density in the cavity for mode m , Γ the longitudinal confinement factor, τ_p the photon lifetime, and β the fraction of the spontaneous emission that goes into the lasing mode. Since most VCSELs lase in multiple transverse modes, a strict rate equation analysis would involve one rate equation per mode. It has, however, been shown by both experiment and simulation that oxide-confined VCSELs are well described by single-mode rate equations because of the tight overlap of the modes due to the index guiding [110]. The subscript m in Equations 3.1 and 3.2 is therefore dropped, and the single-mode rate equations are used. The compression of the gain at high photon densities, due non-linear effects such as spectral hole burning and carrier heating [17], can be taken into account by

$$G(N, S) = \frac{g(N)}{1 + \varepsilon S}, \quad (3.3)$$

where g is the uncompressed gain coefficient and ε the gain compression factor. Equation 3.1 and 3.2 are coupled differential equations and must in general be solved numerically. However, a small-signal analysis can be used to linearize the equations in order to derive an analytical solution. A first-order Taylor expansion can be made by setting

$$I = I_b + \delta I, \quad (3.4)$$

$$N = N_b + \delta N, \quad (3.5)$$

$$S = S_b + \delta S, \quad (3.6)$$

$$G = \frac{g_b}{1 + \varepsilon S} + \frac{g_0 \delta N}{1 + \varepsilon S} - \frac{\varepsilon g_b \delta S}{(1 + \varepsilon S)^2}, \quad (3.7)$$

where index b indicates the bias point around which the linearization is done, and $g_0 = \partial g / \partial N$ is the differential gain at the bias point. By inserting

²Equal to the oxide aperture area times total thickness of the QWs.

³Defect-related non-radiative recombination.

Equation 3.4 to 3.7 into the rate equations, neglecting the small spontaneous emission factor β , discarding higher order terms and time derivatives of constants, and eliminating ∂N , the differential equation representing a second order damped system is obtained as

$$\frac{d^2}{dt^2}\delta S + \gamma \frac{d}{dt}\delta S + 4\pi^2 f_r^2 \delta S = \frac{\eta_i}{qV_a} \frac{\Gamma v_g g_0 S_b}{1 + \varepsilon S_b} \delta I, \quad (3.8)$$

where γ is the damping rate and f_r the resonance frequency. By assuming a sinusoidal variation in the small deviations $\delta I(t) = \delta I_0 e^{j2\pi f t}$ and $\delta S(t) = \delta S_0 e^{j2\pi f t}$, the time derivatives in Equation 3.8 can be replaced by $j2\pi f$. Further, the amplitude change in output power $\delta P(t) = \delta P_0 e^{j2\pi f t}$ is linearly related to the photon density change δS in the cavity⁴. This yields an approximate expression for the transfer function $H_i(f)$ of the intrinsic small-signal modulation response as

$$H_i(f) = \frac{\delta P_0}{\delta I_0} = \text{const} \cdot \frac{f_r^2}{f_r^2 - f^2 + j \frac{f}{2\pi} \gamma}. \quad (3.9)$$

The modulation bandwidth f_{3dB} is defined as the frequency where the response has dropped to half of its low-frequency value⁵. To obtain Equation 3.9, the following approximate expressions for the characteristic parameters f_r and γ were used [92]

$$f_r \approx \frac{1}{2\pi} \sqrt{\frac{v_g g_0 S_b}{\tau_p (1 + \varepsilon S_b)}}, \quad (3.10)$$

and

$$\gamma \approx K f_r^2 + \gamma_0, \quad \text{with} \quad K = 4\pi^2 \left[\tau_p + \frac{\varepsilon}{v_g g_0} \right], \quad (3.11)$$

where γ_0 is the damping offset and K is referred to as the K -factor. These two equations govern the intrinsic response of the VCSEL. The resonance frequency increases with increasing photon density, leading to a larger bandwidth with increasing bias current. However, the damping in turn increases even faster with photon density, and will eventually limit the modulation bandwidth since $f_r \propto \sqrt{S_b}$ while $\gamma \propto S_b$. The maximum intrinsic bandwidth of a VCSEL is therefore limited by the K -factor to [92]

⁴This assumes that the generated photon density is constant throughout the cavity. This is a good approximation for VCSELs, since the cavity round trip time of a photon $\tau_{RT} \ll \tau_p$ due to the high mirror reflectivity

⁵Equivalent to $|H_i(f_{3dB})|^2 / |H_i(0)|^2 = 1/2$ (or -3 dB when plotted in dB scale).

3. VCSEL DYNAMICS

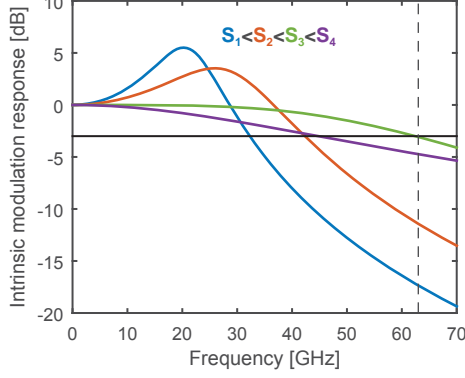


Figure 3.1: Damping-limited intrinsic modulation response for a VCSEL in Paper A, using $K=0.14$ ns and $\gamma_0=8.5$ ns⁻¹.

$$f_{3dB}^{max} \approx \frac{2\sqrt{2}\pi}{K}. \quad (3.12)$$

The intrinsic modulation response for increasing photon densities is seen in Figure 3.1. The maximum modulation frequency is 63 GHz before the damping limits the response. However, 63 GHz is far above the measured maximum bandwidth of 26 GHz for this particular device, because the VCSEL modulation response is reduced by thermal and parasitic effects, as discussed further in the following sections.

To reach a high resonance frequency, a large photon density is required. In order to quantify this, the D -factor is derived from Equation 3.10 as the rate at which the resonance frequency increases with increasing bias current as

$$f_r = D \cdot \sqrt{I - I_{th}}, \quad \text{with} \quad D = \frac{1}{2\pi} \sqrt{\frac{\eta_i \Gamma v_g}{q V_a}} \cdot g_0, \quad (3.13)$$

where I is the bias current and I_{th} the threshold current. A high D -factor signifies the ability to reach high resonance frequencies at low bias currents, and it is therefore an important figure of merit for energy-efficient VCSELs. The D -factor also shows that a small cavity volume⁶ enables VCSELs to reach high resonance frequencies at low bias currents. In Paper A we reduce the mode volume by strongly confining the optical fields with the shortest possible

⁶The volume of the optical mode V_p is connected with the active region volume as $V_a = \Gamma \cdot V_p$.

cavity of $1/2\lambda$ to facilitate a strong carrier-photon interaction. This yields $\sim 20\%$ increase in Γ compared to the next possible⁷ cavity length of $3/2\lambda$ [24].

See [92] or [111] for a more detailed discussion on small-signal modulation dynamics and derivations. It should be noted that the expressions for the D and K -factors in Paper A also include a transport factor χ , describing the effects of carrier capture and escape from the QWs. However, for properly designed active regions χ is approximately equal to one [92].

3.2 Thermal Limitations

The VCSEL resonance frequency will keep increasing with $\sqrt{I_b - I_{th}}$ until the photon density saturates due to thermal effects (as described in Section 2.6). By setting $\gamma=0$ in Equation 3.9, the thermally limited modulation bandwidth can be estimated as

$$f_{3dB}^{thermal} = \sqrt{1 + \sqrt{2}} \cdot f_r \approx 1.55 \cdot f_r. \quad (3.14)$$

A high D -factor is therefore beneficial in order to reach a high resonance frequency before thermal saturation kicks in. Since the resonance frequency saturates at high temperatures, the D -factor is evaluated at low currents, where self-heating effects are negligible and Equation 3.13 is valid. At higher ambient temperatures, the D -factor is reduced by the decrease in η_i due to carrier leakage from the QWs, and the reduced g_0 due to the higher carrier concentration needed to reach the threshold material gain at elevated temperatures. In contrast, the K -factor is relatively insensitive to changes in temperature ([112] and Paper A). The reason is that the free-carrier absorption increases at high temperatures, because of increased phonon scattering rates leading to reduced carrier relaxation times [113]. Meanwhile, g_0 is reduced. These two effects cancel out, leading to a temperature-stable K -factor.

The gain-resonance detuning discussed, in Section 2.6, has an important effect on the thermal high-speed performance, as it influences both I_{th} and g_0 , which is considerably higher on the short-wavelength side of the gain peak [32, 114]. The detuning can be investigated experimentally by measuring I_{th} as a function of temperature, and finding the temperature for the minimum threshold with a quadratic fit. At this temperature, the gain peak and resonance are aligned and the detuning is zero. Our high-speed VCSELs typically have minimum I_{th} at around 0°C , meaning that the detuning is positive above this temperature ([111] and Paper A). This indicates that

⁷A cavity length of for instance λ is also possible. But the standing wave will not have a node in the middle of the cavity where the QWs are preferably positioned.

we have a positive detuning of around 6 nm at RT⁸, growing larger as the temperature increases. A steadily increasing positive detuning is disadvantageous for the high-temperature static performance as the VCSEL must be pumped harder to compensate for the lower gain. However, it is beneficial for the dynamic performance at RT due to the higher g_0 . By using a different approach with a large negative detuning of ~ 15 nm, researchers at TUB have demonstrated impressive results for temperature-stable high-speed 980 nm VCSELs [28, 54, 56, 108]. The negative detuning facilitates temperature-insensitive threshold currents and slope efficiencies, enabling data transmission at 38 Gbit/s from RT to 95°C with unchanged bias conditions [32]. However, the temperature stability comes at the price of worse performance at low and middle temperatures, for instance a lower g_0 from RT to $\sim 70^\circ\text{C}$, compared to 0 nm detuning at RT.

Except for the detuning, there are basically two viable strategies to mitigate detrimental thermal effects; either prevent heating in the first place, or conduct away the generated heat by appropriate heat sinking. Carrier leakage from the QWs could potentially be reduced by an electron blocking layer [115], but this may have adverse effects on the carrier transport and dynamic performance. To simultaneously reduce Joule heating and optical absorption in the DBRs is challenging, since the first requires higher doping levels and the latter lower. A good compromise can be obtained by using modulation doping schemes, with higher doping levels at the nodes of the standing optical field. In a first approximation, this can be achieved by minimizing the resistance-loss product [24, 116]. Another approach is to use intra-cavity contacts to avoid injection of carriers through the resistive DBRs, where most of the Joule heating and free-carrier absorption occurs [33, 53]. However, the long lateral distance the carriers must travel may lead to uneven carrier injection with current crowding at the oxide aperture edges. This is especially harmful for quasi-single-mode VCSELs, as the higher order modes will experience a larger modal gain due to a better spatial overlap with the carriers (Chapter 4). An efficient heat-extraction from the active region can be achieved by using materials with high thermal conductivity in the design. VCSELs emitting at 850 nm may use binary AlAs in the bottom mirror due to its higher thermal conductivity than for instance $\text{Al}_{0.90}\text{Ga}_{0.10}\text{As}$ [117]. At longer wavelengths, where also GaAs is transparent, a fully binary GaAs/AlAs bottom DBR may be used. Papers A to G use AlAs/ $\text{Al}_{0.12}\text{Ga}_{0.88}\text{As}$ in the bottom DBR for good thermal conductivity. Heat-sinking may be improved by electroplating the mesa sidewalls with metal [118], or by removing the substrate and electroplating a metal substrate [119]. However, introducing large metal areas generally leads to larger capacitances, increasing the parasitic limitations.

⁸Assuming the gain peak is red-shifted at $0.32 \text{ nm}/^\circ\text{C}$ [107], and the cavity resonance with $0.06 \text{ nm}/^\circ\text{C}$ [106].

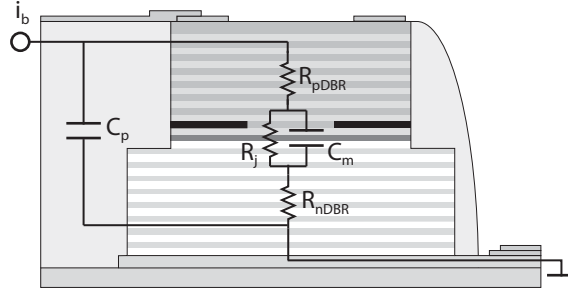


Figure 3.2: Schematic figure of a BCB-planarized VCSEL and a simplified equivalent circuit with the most important parasitic elements.

3.3 Parasitic Effects

As any high-frequency electronic components, VCSELs have a number of parasitic resistances and capacitances. At high frequencies these will act as a low-pass filter, reducing the modulation response. The most important parasitic elements are depicted in Figure 3.2. The main contributions to the VCSEL resistance are the junction resistance R_j , from funneling the current through the narrow oxide aperture, and the n - and p -DBR resistances R_{nDBR} and R_{pDBR} [120, 121]. Low mirror resistance is usually achieved by modulation doping, in order to avoid excessive free-carrier absorption, and grading of the DBR interfaces to facilitate carrier transport across the interfaces.

The mesa capacitance C_m consists of both the junction capacitance (mainly the diffusion capacitance across the pin -junction), and the capacitance over the insulating oxide layers. To reduce the mesa capacitance, recent high-speed VCSELs use elaborate oxide layer configurations with multiple oxide layers [112, 120, 122]. The VCSELs in Paper A to G use a configuration with two deep oxide layers to confine the carriers and provide the transverse optical guiding, and four shallow oxide layers to reduce mesa capacitance. This is accomplished by using a different Al-content in the layers [98]. It has also been seen that the $Al_{0.90}Ga_{0.10}As$ layer closest to the $Al_{0.98}Ga_{0.02}As$ oxidizes vertically from the 98%-layer during oxidation, effectively increasing the oxide thickness from the designed 20-30 nm to 50-70 nm, see Figure 3.3. This increases the index guiding, but also leads to a reduced capacitance [123]. Alternatively, ion implantation can be used to insulate the material above the oxide aperture, but this requires an extra step in the VCSEL fabrication [18, 20]. The bondpad capacitance C_p is kept low by using a thick layer of benzocyclobutene (BCB), with a low dielectric constant, to planarize the VCSEL mesa and separate the bondpads. The n -doped GaAs contact layer is also etched

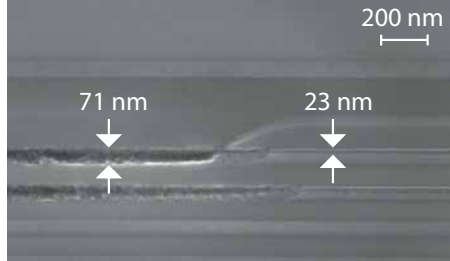


Figure 3.3: Scanning electron microscope (SEM) image of a double oxide aperture. The 23 nm $\text{Al}_{0.98}\text{Ga}_{0.02}\text{As}$ layer is seen, showing the vertical oxidation of the $\text{Al}_{0.90}\text{Ga}_{0.10}\text{A}$ layer below.

away underneath the p -bondpad, leaving only the semi-insulating substrate in order to further reduce bondpad capacitance. The VCSEL parasitic elements can be experimentally analyzed by fitting an equivalent circuit model to the measured small-signal reflection S_{11} [120, 121].

To a first approximation, all of these parasitic effects can be accounted for by adding an extra pole to the VCSEL small-signal modulation response with a parasitic cut-off frequency f_p

$$H_{tot}(f) = \frac{\delta P_0}{\delta I_0} = \text{const} \cdot \frac{f_r^2}{f_r^2 - f^2 + j\frac{f}{2\pi}\gamma} \cdot \frac{1}{1 + j\frac{f}{f_p}}. \quad (3.15)$$

By fitting Equation 3.15 to the measured small-signal modulation response, values for f_r , γ , and f_p can be extracted. The parasitic pole is relatively insensitive to oxide aperture size, since R_j increases for small oxide apertures while C_m decreases ([120] and Paper A).

3.4 High-Speed VCSEL Design

All the previously described limitations must be considered to design state-of-the-art high-speed VCSELs. This is illustrated in Figure 3.4, where the corresponding reductions in maximum bandwidth are shown. The intrinsic VCSEL dynamics are facilitated by using strained InGaAs QWs for high differential gain. The strain reduces the density of states in the top of the valence band, leading to a more rapid separation of the quasi Fermi levels with carrier density [96, 124], and thereby higher differential gain.

Although the thermal and parasitic limitations are typically the main limiting factors (Figure 3.4), a low damping is still essential for high-speed VC-

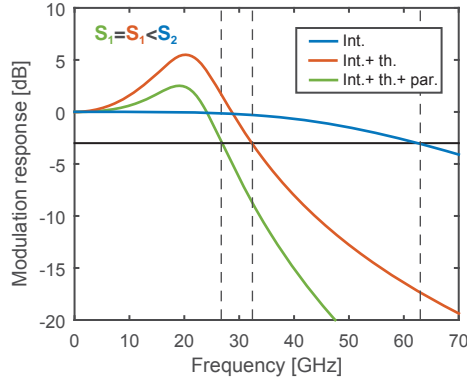


Figure 3.4: Impact of the limiting factors on the modulation response for a VCSEL from Paper A, using $K=0.14$ ns and $\gamma_0=8.5$ ns⁻¹. The necessary photon density S_2 to achieve the intrinsic limit (63 GHz) can not be reached due to the thermal rollover. The thermal saturation of the photon density to S_1 limits the resonance frequency to $f_r^{max}=22$ GHz, decreasing the bandwidth to around 32 GHz. Also including the parasitic effects, by using the parasitic pole $f_p=20$ GHz, further reduces the maximum bandwidth to the measured 26 GHz.

SELS. A low damping leads to a strong resonance peak in the modulation response, that can partially compensate for the parasitic roll-off. Reduced damping can thereby significantly increase the total modulation bandwidth of the VCSEL [112]. This is shown in Figure 3.5, where a modulation response is shown for different K -factors. With reduced damping, the resonance peak is lifted, increasing the modulation bandwidth. However, a too low damping can be detrimental to large signal modulation, causing excessive overshoot and noise during data transmission [125]. The damping factor K is optimized by adjusting the photon lifetime (Equation 3.11). This may be done by a shallow (<60 nm) etch into the top DBR, allowing a post-process setting of the photon lifetime and thereby the damping [112]. The surface etch also has significant impact on the static performance of the VCSEL, since it changes the top mirror reflectivity and thereby the threshold, slope efficiency, and thermal rollover. More details on this can be found in [112] and Paper F.

Another important concern that is out of the scope of this thesis is VCSEL reliability. The vast number of optical interconnects in future supercomputers means that the failure rate must be extremely low. Reliability is an increasing concern for high-speed VCSELs as they are typically biased at higher current densities during operation than the 10 kA/cm² that is the industry standard for 10 Gbit/s VCSELs [126].

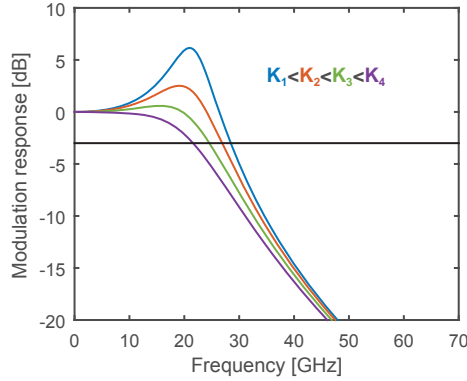


Figure 3.5: Modulation response with different damping, using $\gamma_0=8.5 \text{ ns}^{-1}$, $f_p=20 \text{ GHz}$, $f_r=22 \text{ GHz}$ and $K=0.08\text{-}0.26 \text{ ns}$ in steps of 0.06 ns .

3.5 High-Speed Characterization

This section describes the high-speed measurement methods used for the VCSEL characterization.

3.5.1 Small-Signal Modulation Response

By measuring the small-signal modulation response (S_{21}) of the VCSEL and fitting Equation 3.15 to the measurement, f_{3dB} , γ , f_r , and f_p are extracted. These can then in turn be used to obtain the K - and D -factors from Equations 3.11 and 3.13. With some further parameters from measurements and simulations, the differential gain and the gain compression can also be extracted [112].

A small sinusoidal signal from a network analyzer is combined with the bias current through a bias-T and fed to the VCSEL through a high-frequency RF probe, see Figure 3.6. The output light is focused by an anti-reflection-coated lens system onto an angled-facet short MMF, in order to minimize optical feedback from the measurement setup. A photodetector is used to detect the signal which is fed back to the network analyzer. The measured data is corrected for the photodetector response and probe insertion loss to isolate the VCSEL response. In addition to S_{21} , the reflection coefficient (S_{11}) may be measured to fit an equivalent circuit in order to analyze the parasitic resistances and capacitances of the device [120].

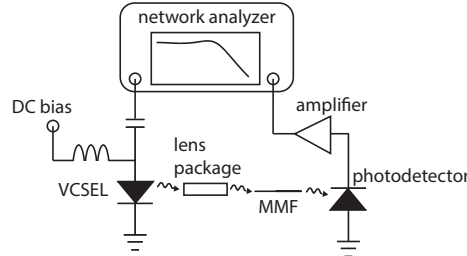


Figure 3.6: The small-signal measurement setup.

3.5.2 Large-Signal Modulation and Data Transmission

A realistic system test is necessary to fully characterize the VCSEL performance in a datacom link. This is performed by setting up a fiber-optical link and transmitting a bit sequence through it. By comparing the sent and received bits, the bit-error-rate (BER) is measured. The measurement setup is seen in Figure 3.7. A pattern generator generates a pseudorandom binary sequence (PRBS) of length 2^7-1 ($=127$) bits, which is combined with the DC bias through a bias-T, and fed to the VCSEL using a high-frequency RF probe. The output light is coupled into a MMF by either butt-coupling or focusing with a lens package. The MMF which is either short (≤ 2 m) for back-to-back (BTB) measurements, or longer for evaluation of link reach. A variable optical attenuator (VOA) is placed before the photodetector to vary the received optical power. If the photodetector does not have an integrated amplifier, an external amplifier is used to boost the signal before it is analyzed. BER is measured by an error analyzer which compares the sent and received bits. An oscilloscope may be used to record eye diagrams consisting of an overlay of many received data patterns. These may be used to measure jitter, rise and fall times, and analyze overshoot, as well as optimize the setup alignment and bias point before performing the more time consuming BER measurements. The photodetector has a significant impact on the link performance, and the photodetectors are as much a limiting factor as the VCSELs in short-reach optical links. The detector limitations for long-reach optical interconnects are discussed in Paper D.

The VCSEL performance is determined by measuring the BER for different received powers, using a bias monitor in the photodetector to record the received optical power. To accurately evaluate very low error-rates ($\text{BER} < 10^{-10}$) statistical methods are used where the BER is taken as the 95% confidence interval. The link is defined as error-free when the BER is less than 10^{-12} with a confidence of 95%, which occurs after measuring 3 Tbit without a single error (regardless of the bit rate) [127]. However, usually >6 Tbit

3. VCSEL DYNAMICS

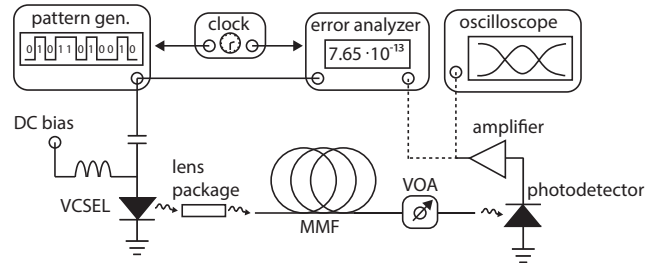


Figure 3.7: The BER measurement setup.

are sent without any error, corresponding to a 99.75% confidence interval of $\text{BER} < 10^{-12}$, and a 95% confidence interval for $\text{BER} < 5 \cdot 10^{-13}$.

Chapter 4

Quasi-Single Mode VCSELs

For a VCSEL to be referred to as single mode, a side-mode suppression ratio (SMSR) larger than 30 dB is typically required. If nothing else is specified, *single mode* usually refers to a VCSEL lasing in the fundamental LP_{01} mode, which has two different polarizations. Single-polarization emission can be achieved by introducing some anisotropy in the cavity, for instance by using gratings [128]. Single-mode VCSELs have been extensively researched since the beginning of VCSEL development. They are essential for long-wavelength (1.3 and 1.55 μm) communication VCSELs and many sensing applications such as gas sensing [129]. However, most applications pose complicated demands on the VCSEL, leading to a trade-off between output power, high-speed properties, and spectral characteristics. As previously discussed in Figure 1.3, almost all of the reported highest bit-rate-distance product 850 nm VCSEL links today use single-mode or quasi-single-mode VCSELs. The term *quasi-single-mode* does not have a clear definition, other than being a VCSEL that is *almost* single mode. The term is used in this thesis to refer to VCSELs with an SMSR of $\sim 15\text{-}20$ dB.

There are several designs aimed at achieving single-mode emission or low-spectral width of 850 nm GaAs-based VCSELs. In general there are two different approaches; an inherently single-mode waveguide, or a mode selective loss. The former includes photonic crystal VCSELs and basically any device with a narrow enough transverse aperture and sufficiently small index step [130]. Mode selective losses can be implemented by for instance metal apertures, extended cavities, and shallow surface reliefs [131–133]. There are also more complex VCSEL designs with non-epitaxial structures, such as using a curved external mirror which has achieved 15 mW of single-mode power [134]. This thesis concerns two of the most promising approaches to simultaneously

4. QUASI-SINGLE MODE VCSELS

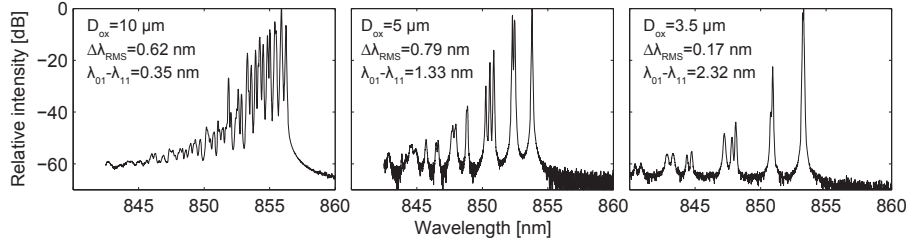


Figure 4.1: VCSEL spectra for decreasing oxide aperture diameter with values for the RMS spectral width, and the mode spacing between the fundamental and first higher order mode ($\lambda_{01} - \lambda_{11}$). The VCSELs are biased about halfway to their respective thermal rollover.

achieve excellent high-speed properties and low spectral width; either using a small oxide aperture or an integrated surface-relief mode filter.

4.1 Small Oxide Aperture

A large oxide aperture and strong index guiding results in a large V and many guided modes, see Equation 2.7 and Figure 4.1. Hence, reducing the oxide aperture diameter to reduce the number of guided modes could be expected to reduce the spectral width. However, doing so will lead to a larger mode spacing (according to Equation 2.6), which comes in squared when calculating the RMS width (Equation 2.9). In general, large aperture devices will have a relatively narrow RMS spectral width because the mode spacing is small. However, the numerous modes will lead to significant modal dispersion during long-reach transmission. Shrinking the oxide aperture reduces the number of modes, but does not decrease the spectral width because of the increased mode spacing, essentially reducing modal dispersion effects at the cost of increased chromatic dispersion. In order to simultaneously reduce the effects of chromatic and modal fiber dispersion, and reach low RMS widths, a single-mode or quasi-single-mode VCSEL is required. This is illustrated in Figure 4.1.

A quasi-single-mode VCSEL is obtained by shrinking the oxide aperture size to $\sim 3.5 \mu\text{m}$ for high-speed VCSELs, while single-mode operation requires even smaller oxide aperture of just $\sim 2 \mu\text{m}$. For lower index guiding, such as ion implantation or oxide-confined VCSELs with only one thin oxide layer, apertures around $4\text{-}5 \mu\text{m}$ may yield single-mode emission. For instance a high single-mode power of 4.8 mW has been obtained using an $3.5 \mu\text{m}$ single oxide aperture VCSEL [130]. Even though small aperture devices have excellent

spectral properties, there are several drawbacks of such a small device aperture. The output power is relatively small, in general being limited to 1-2 mW, giving a limited power budget for long-reach links. A small oxide aperture can also enhance diffraction losses, leading to higher threshold current and lower output power. Funneling the current through the small aperture also leads to an increase in differential resistance from $<100 \Omega$ for $7 \mu\text{m}$ devices, to $200\text{-}300 \Omega$ for a small oxide device. This large impedance mismatch between the VCSEL and the driver leads to large microwave reflections and inefficient transfer of the modulation energy.

Although smaller devices operate at smaller currents, the current density (bias current divided by oxide aperture area) is increased compared to large devices. The industry standard for reliable operation is $10 \text{ kA}/\text{cm}^2$ [126], while the reported small oxide VCSELs for long-reach transmission operate at $20\text{-}35 \text{ kA}/\text{cm}^2$ ([51, 68] and Paper C). These high current densities may shorten the device lifetime, leading to premature device failure. On the other hand, smaller oxide aperture VCSELs seem to handle higher current densities better [126], likely because of the larger perimeter relative to the active area, enabling a better heat sinking of the generated heat. In a recent reliability study, 50 high-speed VCSELs with $6 \mu\text{m}$ oxide aperture were biased at 5 mA ($18 \text{ kA}/\text{cm}^2$) at 95°C for 6000 h without any failures [135], indicating that relatively small oxide aperture devices can operate reliably at elevated current densities. However, the reliability of even smaller oxide aperture ($2\text{-}4 \mu\text{m}$) high-speed VCSELs with InGaAs QWs and multiple oxide apertures has still not been thoroughly evaluated (to my best knowledge).

The fabrication of small oxide aperture VCSELs is straightforward with no extra processing steps, but requires a reproducible and uniform oxidation process. Since the oxidation rate is exponentially dependent on the temperature, a temperature variation across the wafer below 0.5°C is required [98]. This can, however, be managed by a well calibrated fabrication process, and small oxide apertures devices are actually the highest-volume production VCSEL type since they are used in optical computer mice [17]. It should be noted that the lifetime requirements on VCSELs for communication are likely much stricter than for computer mice. In addition, optical computer mice VCSELs usually have single oxide layers and operate at a smaller current density (1.5 mA for a $4 \mu\text{m}$ device, $12 \text{ kA}/\text{cm}^2$) than what is necessary for high-speed operation [17]. The small oxide aperture approach is explored in Papers C and D.

4.2 Surface Relief Mode Filter

Instead of altering the guiding of the waveguide, a mode-selective loss can be used to suppress higher-order modes. One property that distinguishes the different transverse modes in a VCSEL, is their different spatial intensity distri-

4. QUASI-SINGLE MODE VCSELS

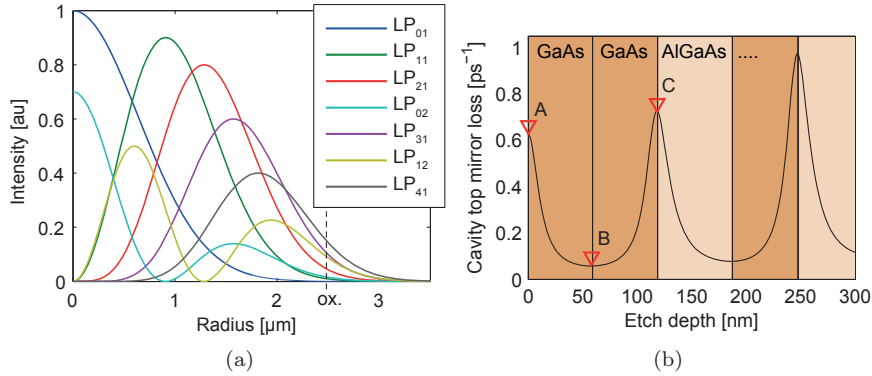


Figure 4.2: (a) Radial intensity distributions of the seven lowest order transverse modes in a 5 μm oxide aperture VCSEL (from Equation 2.4, ox.=oxide aperture edge). (b) Calculated top mirror loss rate as a function of etch depth.

butions, seen in Figure 4.2a (and Figure 2.5). Hence, by introducing a spatially varying loss, the threshold of the higher-order modes can be made larger than that of the fundamental mode. The top mirror loss can be greatly varied by varying the thickness of the topmost layer of the top DBR, see Figure 4.2b. Because of the periodic DBR structure, etching away one quarter-wavelength layer will change the phase of the semiconductor-air reflection, in essence modifying the top mirror reflectivity. For a DBR with an initial anti-phase top reflection (point A in Figure 4.2b), etching away the top 59 nm of GaAs results in an in-phase reflection (point B in Figure 4.2b) and lower mirror loss (corresponding to higher mirror reflectivity). Etching a quarter wavelength deep recess into the top anti-phase layer, lowers the mirror loss in the center of the waveguide, lowering the threshold for the fundamental mode which has the largest overlap with the etched region, see Figure 4.3b. The etched recess, called an inverted surface relief, functions as an integrated mode filter.

Most early mode-filter VCSELS featured an initial in-phase top reflection, equivalent to beginning at point B (Figure 4.2b) and etching a donut-shaped recess to point C, see Figure 4.3a. The drawback of this design is that it requires a very precise etch to point C. For an inverted surface relief, the high precision of epitaxial growth is used to grow the material to an anti-phase reflection, reducing the precision requirements for the shallow etch. For optimal mode selectivity the mode filter should have a diameter equal to half the oxide aperture and be centered in the oxide aperture [136].

Mode filtering by shallow surface etching was first demonstrated by Dowd

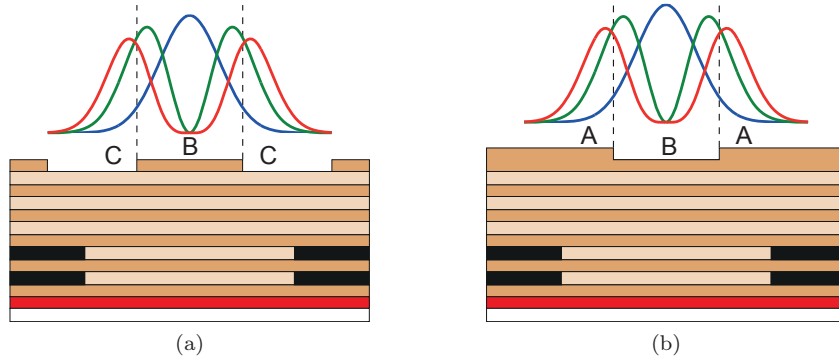


Figure 4.3: Schematic figure of surface-relief techniques illustrating the oxide aperture and the overlap of the three lowest-order modes (LP_{01} , LP_{11} and LP_{21}) for (a) donut-shaped surface relief etched from B to C, and (b) inverted surface relief etched from A to B in 4.2b.

et al. in 1997, achieving single-mode emission for large aperture implanted VCSELs and a spectral narrowing for oxide-confined VCSELs [137]. The technique was from the late 1990's further developed mainly by Chalmers University of Technology [128, 133, 136] and Ulm University [138–140]. The mode-filtering technique has successfully achieved single-mode VCSELs with output powers exceeding 6 mW [133, 140]. For applications such as gas sensing, where a single polarization is desired, a subwavelength grating surface relief can be used to achieve polarization-stable single-mode emission [128, 139]. The surface-relief method has also been applied to other material systems, for instance AlGaSb VCSELs emitting at 2.35 μm [141]. High-speed VCSELs with inverted surface reliefs are investigated in Papers E, F and G.

4.2.1 Effects on Static Characteristics

Since the shallow surface etching affects the top DBR reflectivity, the threshold current and slope efficiency are also affected. For an initial anti-phase top DBR, the inverted surface-relief etching increases the overall top mirror reflectivity, in effect lowering the threshold current and slope efficiency. A large reflectivity also leads to a longer photon lifetime, leading to an increased internal absorption rate, and stronger damping of the modulation response accompanied by lower bandwidth [112] (as discussed in Section 3.4). A shorter photon lifetime for lower damping requires a larger overall loss, while a successful mode discrimination still requires a large loss difference between points A and B in Figure 4.2b. This seems possible by for instance using fewer mirror

4. QUASI-SINGLE MODE VCSELS

pairs, as seen in Figure 4.2b. The top mirror loss is in general increased for fewer mirror pairs and the maximum loss difference between an anti-phase and in-phase reflection also increases.

Chapter 5

VCSEL Fabrication

The epitaxial VCSEL structures used in this work were grown by IQE Europe Ltd. using metal-organic chemical vapor deposition (MOCVD). Molecular beam epitaxy (MBE) can also be used to grow the structure, but MOCVD is usually preferred for commercial production because of the higher throughput. In MOCVD gaseous organic compounds transport III-metals (Al, Ga, In) into the reactor where they react with gaseous As (carried by the gas AsH_3) and adsorb on the heated substrate. Doping is done by introducing Si or C into the reactor for *n*- and *p*-doping. After the growth of the epitaxial structure, the device processing starts. The different processing steps used in high-speed VCSEL fabrication are briefly described in this chapter, followed by an overview of the full VCSEL process.

5.1 Lithography

Most process steps in micro- and nanofabrication starts by patterning a protective coating called a resist on the sample using lithography. The most straightforward method is photolithography where a photoresist (a photosensitive polymer diluted with a solvent) is used. The viscous photoresist is dispensed onto the sample which is spun at a few thousand rounds per minute to form a thin film. The film thickness is on the order of one or a few micrometers depending on the resist viscosity and spin speed. The resist is then baked on a hotplate to remove the solvent. To pattern the resist a glass plate with a chromium pattern is manually aligned on top of the sample, shadowing certain areas as the sample is exposed with ultra-violet radiation at 400 nm. By using a liquid developer, the exposed areas can be removed, leaving a pattern on the sample. The manual alignment has an error margin of around 1 μm . If a

so-called negative resist is being used, the unexposed resist areas are instead removed. A third resist type is image reversal resist, commonly used for lift-off processes.

The wave nature of light prohibits definition of features smaller than $\lambda/2$ by conventional photolithography. Standard contact photolithography with a resolution of approximately 1 μm , was used in this work [142]. More advanced photolithography techniques such as phase shifted masks, enables the definition of features smaller than 100 nm. However, such a process is not feasible for a flexible research environment, where electron-beam lithography is used instead. It works essentially the same way as photolithography, but instead using an electron-sensitive resist. The main difference is that instead of a UV lamp exposing the entire sample as once, an electron beam scans across the sample, making this lithography technique a more time consuming serial process. Because of the very short electron wavelength, electron beam lithography can achieve a resolution down to 10 nm. The electron beam lithography system uses an automated alignment system that detects alignment marks on the sample for near perfect alignment. Definition of small features in commercial production may also be done by nanoimprint lithography, where an imprint resist is patterned with a stamp. Compared to the serial electron beam lithography, nanoimprint is very fast, but manufacturing of the stamp is expensive and it allows no process flexibility. Nanoimprint lithography has for instance been used to fabricate polarization-stable sub-wavelength grating VCSELs [143].

5.2 Thin Film Deposition

Both dielectric and metal thin films are used in VCSEL processing. Dielectric materials such as Si_xN_y (exact stoichiometry varies with deposition conditions), SiO_2 , amorphous Si and TiO_2 are commonly used as electrical passivation layers, hard masks for etching, and optical coatings, as well as to protect surfaces during particular processing steps. Metal thin films are used for contacts on semiconductor material and bondpads. A lift-off process with an image-reversal photoresist is usually used for thin-film deposition. After deposition the image reversal resist is lifted off by immersion in heated solvents (usually acetone, methanol and isopropanol). For difficult lift-offs, acetone spray may be used, while ultrasonic bath should be avoided because of the risk of breaking the relatively brittle GaAs samples.

Dielectric materials are commonly deposited by plasma-enhanced chemical vapor deposition (PECVD). Gases are injected into a vacuum chamber where a plasma is generated by a plasma source as, for instance, an inductively-coupled plasma (ICP). Ions and reactive radicals from the plasma react on the sample surface to form the thin film. The film thickness can be precisely

in-situ monitored by a laser interferometer. ICP-PECVD was used to deposit Si_xN_y to protect the top surface during oxidation and as a hardmask for mesa processing for mode filter VCSELs.

Metals thin films are conveniently deposited by electron-beam evaporation. An electron beam is used to heat the metal which evaporates and the metal vapor adsorbs on the sample. The deposition rate is accurately controlled by monitoring the decrease in resonance frequency of a crystal as the deposited film thickness increases. This technique was used to deposit Ti/Pt/Au p-contacts and Ni/Ge/Au n-contacts.

Both dielectric and metal films can be deposited by sputtering. Energetic Ar ions generated in a plasma are accelerated towards a target and sputter away atoms which are deposited on the sample. Sputtering has the advantage of a better step coverage than PECVD and electron beam evaporation, and was therefore used to deposit Ti/Au bondpads in this work.

5.3 Etching

Removal of semiconductor material may be done by either dry or wet etching, depending on the requirements on etch rate, anisotropy and selectivity. Wet etching is inherently chemical where a reactive liquid dissolves the material. GaAs wet etchants usually contain one oxidizer that oxidizes the surface and one acid that then dissolves the oxide. Even though a high selectivity can be achieved for certain material systems, the etched material usually etches isotropically, meaning that for instance a VCSEL mesa etched by wet etching would have sloped sidewalls.

When vertical sidewalls are desired, dry-etching techniques are used. Ions and radicals are created in a plasma and accelerated towards the sample by an electric field, where the ions sputter away material and the highly reactive radicals chemically etch the material. This gives the dry-etching process both a physical and a chemical etch component. By changing the process parameters the plasma density and accelerating electric field may be varied, meaning that the chemical and physical process components may be individually tuned in order to optimize the process. The etched material forms volatile products that leave the process chamber through the vacuum exhaust. In this work inductively coupled plasma reactive ion etching (ICP-RIE) was used to etch AlGaAs (using SiCl_4/Ar and Cl_2/Ar), Si_xN_y (using NF_3), and benzocyclobutene (BCB, using CF_4/O_2). The dry etching was done in the same tool as the PECVD and the etch depth can be *in-situ* monitored with a laser interferometer.

To achieve a very precise etch depth for the surface-relief mode filters, Ar ion-beam milling was first used. Ar ions are generated in a plasma and accelerated towards the surface, sputtering away material. While the etch

rate for ICP-RIE may vary due to different conditions that affect the sensitive chemical component of the etch, the ion beam milling is purely physical. This enables a very stable and reproducible etch rate, allowing precise etch depths by timed etching. One drawback is that the etched material does not form volatile products, and may redeposit somewhere else on the sample. Papers E and F used Ar ion beam milling to etch the mode filters, while Paper G used ICP-RIE using the laser interferometer for *in-situ* monitoring.

5.4 Wet Oxidation

In order to form the oxide aperture, the etched mesa sidewalls are exposed to hot water vapor at 420°C. Nitrogen gas is fed through a bubbler and carries the water vapor into a furnace. Through a glass window in the top of the furnace chamber, the oxidation can be *in-situ* observed by imaging the sample with an infrared LED through a microscope onto a CCD camera. The oxide apertures can be discerned by the difference in reflectivity between the oxidized and non-oxidized areas. The oxidation process is highly sensitive to the temperature and even a small temperature gradient across the sample will lead to a varying oxidation rate and an undesired spread in oxide apertures across the chip [98]. To avoid this, the chip can be turned 180° after half the process time. The oxidation rate for $\text{Al}_{0.98}\text{Ga}_{0.02}\text{As}$ is approximately 0.25 $\mu\text{m}/\text{min}$ in our standard oxidation process. Layers with a lower Al content will oxidize much slower, but neighboring layers such as $\text{Al}_{0.90}\text{Ga}_{0.10}\text{As}$ may oxidize vertically from the 98% layer, making the oxide layer thicker, see Figure 3.3.

5.5 High-Speed VCSEL Process

Before processing started, the large 3" wafer was cleaved into 8 x 10 mm chips and cleaned. As a first step Ti/Pt/Au alignment marks and top *p*-contact rings were deposited by electron-beam evaporation (Figure 5.1a). Then a Si_xN_y film was blanket deposited to protect the top surface during the later wet oxidation step. The mesas were defined by electron-beam or photolithography. The mesa etching was done with ICP-RIE to first remove the protective Si_xN_y (using NF_3), and then etch the AlGaAs with Ar/ SiCl_4 and Ar/ Cl_2 . A precise etch depth of 3.3-3.5 μm was obtained by using the *in-situ* laser interferometer in order to expose the oxide layers, but not the AlAs layers of the bottom DBR. Without breaking vacuum, the sample was moved to another chamber, where ICP-PECVD was used to deposit another layer of Si_xN_y . After lifting off the photoresist, the chip was thereby covered in Si_xN_y without any AlGaAs being exposed to air (Figure 5.1b). The Si_xN_y on the sidewalls was then removed by photolithography and ICP-RIE etching with NF_3 , which has a high selectivity

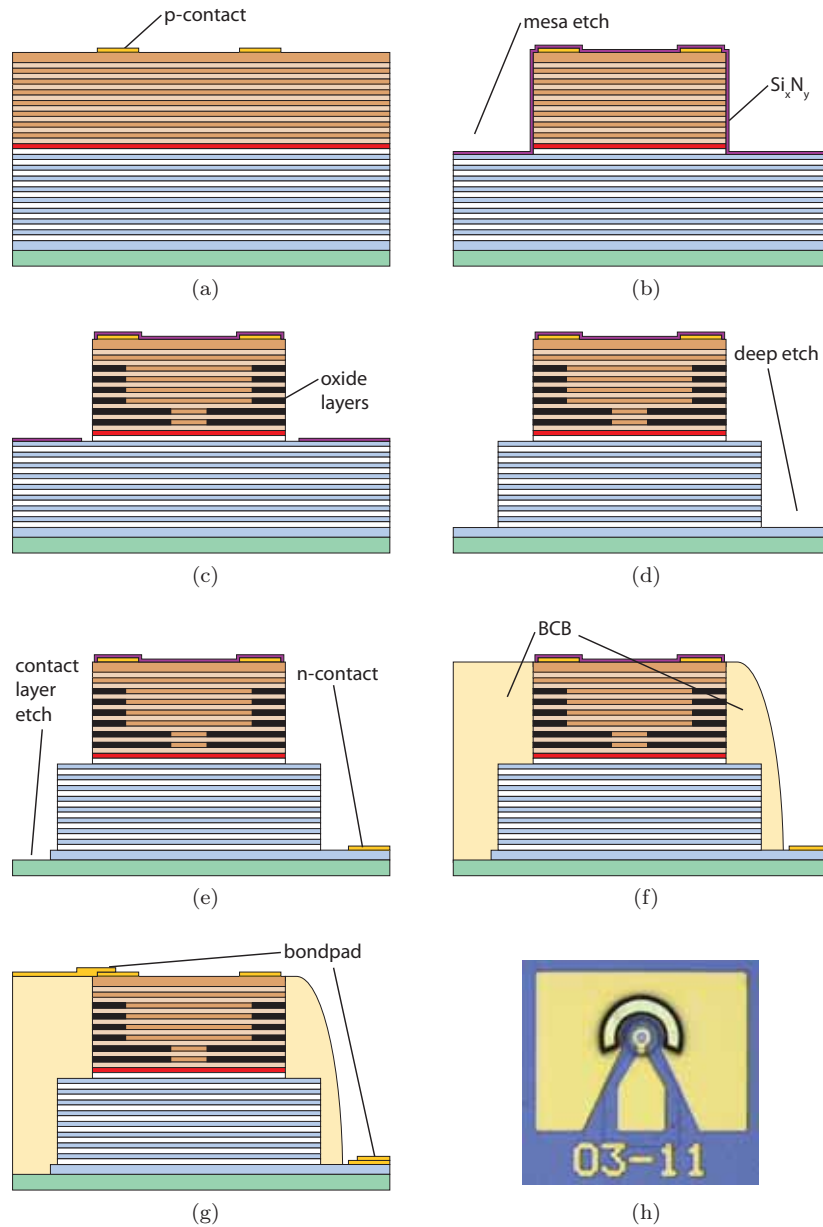


Figure 5.1: High-speed VCSEL process steps: (a) top contact evaporation, (b) mesa etch and Si_xN_y deposition, (c) open up Si_xN_y and wet oxidation, (d) deep etch, (e) bottom contact evaporation and contact layer etch, (f) BCB planarization and contact layer etch, (g) bondpad deposition. (h) a microscope image of a finished high-speed VCSEL (courtesy of Dr. P. Westbergh).

(~ 100) to AlGaAs. The oxidation at 420°C takes around 40 min, depending on the exact Al-content, and was monitored using the *in-situ* microscope (Figure 5.1c). By using different mesa sizes, oxide aperture diameters from 3 to 9 μm were obtained. After photolithography, the bottom mesa was etched to reach the *n*-contact layer, using again NF_3 to remove the Si_xN_y , and Ar/SiCl_4 and Ar/Cl_2 to etch the AlGaAs (Figure 5.1d). The bottom Ni/Ge/Au *n*-contacts were deposited by electron-beam evaporation and annealed for 30 s at 430°C in an N_2 atmosphere. Following this step the *n*-doped GaAs contact layer was removed under the future *p*-bondpad by photolithography and ICP-RIE etching (Figure 5.1e). A thick layer of BCB was spun over the mesa to planarize the structure (Figure 5.1f). The BCB is photosensitive, enabling opening up of the BCB covering the *n*-contact and mesa by photolithography. However, spreading of the UV-light in the thick BCB gives poor contrast, and prevents complete opening up by photolithography only. The last BCB must therefore be etched away using ICP-RIE etching with CF_4/O_2 . It is very important to remove all BCB, and at the same time not etch through the protective Si_xN_y . As final steps, the protective Si_xN_y was removed with ICP-RIE and Ti/Au bondpads were deposited by sputtering to achieve a good step-coverage into the *n*-contact trench in the BCB (Figure 5.1g).

5.5.1 Surface-Relief Processing

There are a few special requirements on the processing of mode-filter VCSELs. Firstly, the epitaxial growth must have nm-precision in order to have an anti-phase top DBR reflection with a high mirror loss (see Section 4.2). For the processing of the mode filter it is necessary to achieve a good alignment between the oxide aperture and the surface relief, as well as a precise etch depth (Figure 4.2b). Near perfect alignment is obtained by using electron-beam lithography to define the mode filters, aligned to etched alignment marks defined simultaneously with the mesas. Another option would be to use a self-aligned process, where the mesa edge, which will define the oxide aperture, and the mode filter is defined by a donut-shaped hard mask [138]. However, because of variations in oxide aperture due to a varying oxidation rate, the mode filters were defined and etched as the very last process step. This allowed matching of every oxide aperture with an appropriate mode filter. It is critical that the VCSEL top surface, with its anti-phase reflection, is carefully protected during the processing since accidental oxidation or etching of just a few nanometers will impact the mode filter performance.

Chapter 6

Monolithic Multi-Wavelength VCSEL Arrays using High-Contrast Gratings

By proper design of the HCG-VCSEL cavity, the resonance wavelength can be set in a single lithography step by defining HCGs with different period and duty cycle. Using this effect to design multi-wavelength arrays with HCG-VCSELs was first proposed by Kim *et al.* in 2007 [144]. Such devices have since then been designed and experimentally demonstrated by optical pumping experiments [145]. This thesis presents the first demonstration of wavelength-setting of electrically-injected HCG-VCSELs using the grating parameters (Paper H). This chapter starts with a review of different techniques to realize monolithic multi-wavelength VCSEL arrays, followed by a presentation of the important properties of HCGs and details on the design of multi-wavelength HCG-VCSELs.

6.1 Monolithic Multi-Wavelength VCSEL Arrays

A low-cost monolithically integrated multi-wavelength light source is highly desired for WDM in optical interconnects. Small variations in VCSEL wavelengths, on the order of a couple of nm, can be realized by using VCSELs with different oxide aperture [146], or biasing the VCSELs at different currents [147]. But for uncooled operation a wider channel spacing is needed. Different designs and technologies for fabricating multi-wavelength VCSEL arrays have been explored since the early 1990's. In general all techniques work by modifying the effective cavity length and thereby the resonance wavelength. Early attempts utilized nonuniform epitaxial growth by MBE [148], and MOCVD growth on patterned substrates using non-uniform gas flow in

etched grooves [149]. The latter technique was used to demonstrate VCSEL arrays with an impressive wavelength span of 192 nm from 960-1160 nm, but requires complicated epitaxial growth techniques [150]. Strained suspended cantilevers with top DBRs where the cavity length depends on the cantilever length have also been explored [151]. These techniques successfully demonstrated multi-wavelength VCSEL arrays across the wafer, but are not suitable for small-footprint dense VCSEL arrays with arbitrary layout. Better wavelength control and layout flexibility can be achieved by post-growth intra-cavity modifications using micro- and nanofabrication techniques. By vertically oxidizing a thick AlGaAs layer, devices with different cavity length can be lithographically defined [152]. However, introducing thick oxide layers may lead to issues with thermal conductivity. Another technique is adjusting the thickness of a phase-tuning layer inside the VCSEL cavity. By using a dielectric top DBR, the VCSEL cavity can be accessed during fabrication. The resonance wavelength can be easily modified by varying the thickness of the cavity or the first DBR layer by either deposition or etching [153–156]. However, these intra-cavity techniques require at least $\log_2(N)$ highly accurate etching or deposition steps, where N is the number of channels desired. Precise thickness control is necessary for accurate wavelength control to fabricate VCSEL arrays with wavelengths falling within the desired wavelength slots of the WDM channels [157].

A design utilizing high-contrast gratings (HCGs) for lithographically defined post-growth wavelength setting was proposed in 2007 by Kim *et al.* [144], and further described in 2010 by Karagodsky *et al.* [158]. By fabricating HCGs with different parameters (period, duty cycle), the grating reflection phase may be tailored, introducing a certain phase shift in the cavity that determines the resonance wavelength. Such devices have previously been designed and proven by optical pumping experiments [145], using VCSELs with an InP active region and wafer bonded mirrors of Si HCGs buried in SiO₂. The optical pumping realized a wavelength span of 12 nm around 1.55 μ m. Electrically-injected wavelength-setting of HCG-VCSELs using the grating parameters have so far not been published. The main challenge is that HCGs with exceptionally high reflectivities are needed as further described in this chapter. A monolithic multi-wavelength HCG-VCSEL array was presented by Rao *et al.* in 2010 [159]. However, the wavelength was set by varying the air gap thickness below a suspended HCG using time-controlled wet etching, and not by changing the grating parameters.

In addition to controlling the cavity length, an active region with a broad optical gain is desired to design VCSEL arrays with a wide wavelength span and uniform device performance. By using QWs with different widths, the same active region could support lasing over a 90 nm span from 766 nm in a tunable grating-coupled ring laser [160]. MOVCD growth on patterned sub-

strates, mentioned earlier, realized QWs with different widths, enabling the impressive wavelength span of 192 nm from 960-1160 nm [150]. Hence, even though they were grown simultaneously, the different VCSELs in the array have different active regions. Using identical-quantum-well active regions, lasing over a span of ~ 20 -30 nm is commonly obtained in monolithic short-wavelength multi-wavelength VCSEL arrays [148, 152–154]. This wavelength span could enable 3-4 WDM channels with 10 nm channel spacing. However, nonuniform device performance would likely be a significant issue, and may well prevent high-speed (>25 Gbit/s) operation.

6.2 High-Contrast Gratings

High-contrast gratings (HCGs) are gratings of a high-refractive index material surrounded by low-index material, see Figure 6.1. For sub-wavelength HCG periods, remarkable properties such as close to 100% reflectivity with a wide stop-band can be obtained for certain HCG parameters [161]. Highly reflective HCGs were first proposed and demonstrated by the group of Prof. Connie J. Chang-Hasnain at the University of California, Berkeley in 2004 [162, 163]. The first VCSEL with an HCG-based top mirror was demonstrated by the same group in 2007 [164]. Since then HCGs have been proposed and fabricated in a wide range of materials for different wavelengths ranging from 450 to 2300 nm [163, 165–167]. Already from the start, HCGs attracted a large interest as mirrors for InP-based VCSELs emitting at 1310 or 1550 nm [166, 168], since epitaxial DBRs in this material system have a small index difference between the high and low-refractive index material, resulting in long growth times for the thick DBRs and a narrow reflection stopband. The small mass of the thin HCG compared to a ~ 30 -pair DBR has also enabled micro-electro-mechanical systems (MEMS)-VCSELs with ultra-fast electrostatic tuning [169].

The phase of the HCG reflection and transmission is highly dependent on the HCG parameters, for instance grating period and duty cycle. This effect is used in this work to design and demonstrate monolithically integrated multi-wavelength VCSEL arrays. The same phenomena can also be used to design and fabricate chirped-period HCGs with arbitrary spatially varying phase, enabling the design of flat lenses with high numerical aperture [170]. Furthermore, HCGs have several additional interesting properties. They may be used both as reflectors, vertical to in-plane couplers, or a combination thereof [171], making them highly interesting for applications in small-footprint integrated optics in both silicon photonics and heterogeneously integrated III-V on silicon [171–173].

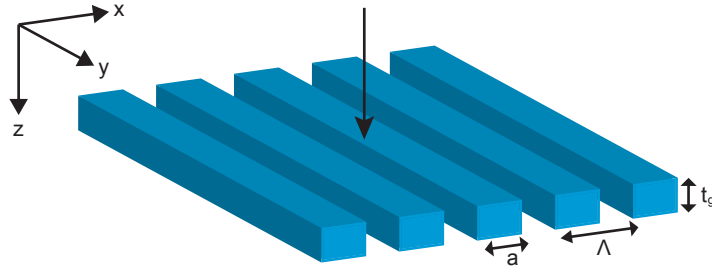


Figure 6.1: Schematic figure of a high-contrast grating.

6.3 Physics of HCGs

The grating is formed by bars of high-refractive-index material (e.g. GaAs with $n \approx 3.5$) surrounded by air, see Figure 6.1. For bars with ideal rectangular cross-section, the HCG is fully characterized by the grating thickness t_g , period Λ , and duty cycle a/Λ , where a is the grating bar width. HCGs can be designed for either transverse electric polarization (TE, electric field parallel to HCG bars) or transverse magnetic polarization (TM, electric field perpendicular to HCG bars), where the different boundary conditions lead to different characteristics [174], see Figure 6.2. All the HCGs in this thesis are designed for TM polarization. From the input plane at $z = 0$ the HCG looks like an array of slab waveguides with a width a , period Λ , and length t_g . An incoming plane wave excites array waveguide modes in the HCG propagating in the $+z$ -direction. Because of the large index contrast and near-wavelength dimensions, the cut-off frequencies for the array waveguide modes are widely spaced, and there is a large wavelength range where only two guided modes exist. Hence, there are two modes with real propagation constant that carry energy, while higher order modes are cut-off and form evanescent waves. While propagating from the input HCG plane at $z = 0$ to the output at $z = t_g$, the two guided modes accumulate different phase. At the output plane they are reflected and also couple to each other, because of the abrupt index change. The two modes then travel back to the input plane where a similar reflection and coupling occurs. For proper HCG thickness, the accumulated phase difference between the two guided modes, together with the interaction at the output and input planes, cause the two guided modes to experience destructive interference at the output plane. Because of the sub-wavelength dimension, only the 0th order diffraction order exists. Therefore no light may be diffracted and no light may be transmitted due to the destructive interference. As a result the light will be reflected, achieving reflectivities close to 100% over a wide wavelength range, see Figure 6.2. High reflectivities are obtained for HCGs

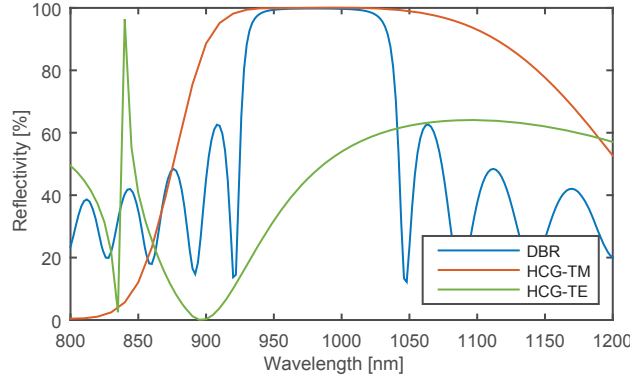


Figure 6.2: Comparison of the reflectivity spectra of an HCG with thickness 270 nm, period 405 nm, and duty cycle 60% and a typical top DBR consisting of 21 pairs of $\text{Al}_{0.90}\text{Ga}_{0.10}\text{As}/\text{GaAs}$.

with a large variation in period and duty cycle, as seen in Figure 6.3a, but different HCG parameters will result in different phase of the reflection from the HCG, see Figure 6.3b. The HCG thickness was chosen as 270 nm to obtain a large highly-reflective region coinciding with a large span in reflection phase. For HCGs with a period of around 400-450 nm and DC from 45-75%, reflection phases spanning 60° can be obtained. Even larger reflection phase spans can be reached for larger DCs, but DCs $>75\%$ can be challenging to fabricate as discussed further in Section 7.2. For more details on the physics of HCGs, see for instance the work of C. J. Chang-Hasnain *et al.* [161].

Both analytical and numerical analysis of HCGs are relatively straightforward for infinite gratings by using periodic boundary conditions [161]. In effect this means infinitely long grating bars (infinite extent in y -direction), and infinite periodicity in x -direction. Simulations are typically performed using rigorous coupled-wave analysis (RCWA), which is an efficient method for analysis of planar gratings [175]. RCWA solves Maxwell's equations by a Fourier series expansion and matching of the electromagnetic field at boundaries. RCWA is used to study infinite gratings, while finite-difference time-domain (FDTD) methods may be used to simulate finite-size effects [176]. The RCWA simulations presented in this work were performed using the RiCWaA MATLAB package from the University of Michigan [177].

The reflection and transmission properties of doped HCGs were investigated by RCWA simulations. Free-carrier absorption was accounted for by a complex refractive index $n - i\kappa$, with an extinction coefficient of

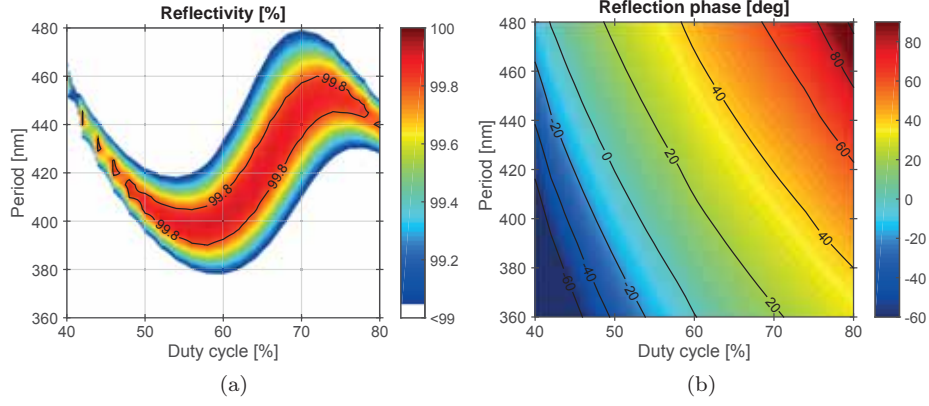


Figure 6.3: RCWA simulation of HCGs with $t_g = 270$ at 980 nm. (a) Power reflectivity and (b) reflection phase as function of period and duty cycle.

$$\kappa = \frac{\alpha \lambda_0}{4\pi}, \quad (6.1)$$

where α is the absorption coefficient. This can be related to the acceptor concentration in the p -doped GaAs grating layer as

$$\alpha [\text{cm}^{-1}] = 7 \cdot 10^{-18} \cdot N_a [\text{cm}^{-3}], \quad (6.2)$$

where N_a is the acceptor concentration [178]. The grating absorption loss was calculated as $1 - R - T$.

For undoped highly-reflective HCGs, all of the incident light is either reflected or transmitted, see Figure 6.4. With increasing absorption, the reflectivity is reduced and the loss, calculated as $1 - R - T$, increases correspondingly. Surprisingly, the transmission is unaffected by absorption. Although the transmission for fabricated gratings is likely considerably higher than expected from simulations, this raises questions as to the physical origins of the HCG transmission. The simulations thus indicate that the HCG absorption loss due to free-carrier absorption causes a considerable reduction in the efficiency of HCG-VCSELs. If this is indeed that case, an undoped HCG could be used, and top contacts deposited on the current-spreading layer, see section 6.4.1. It should be noted that the RCWA simulations are for perfect gratings, and no diffraction loss is observed in the simulations, but may be present in real HCGs with a certain surface roughness and non-vertical sidewalls.

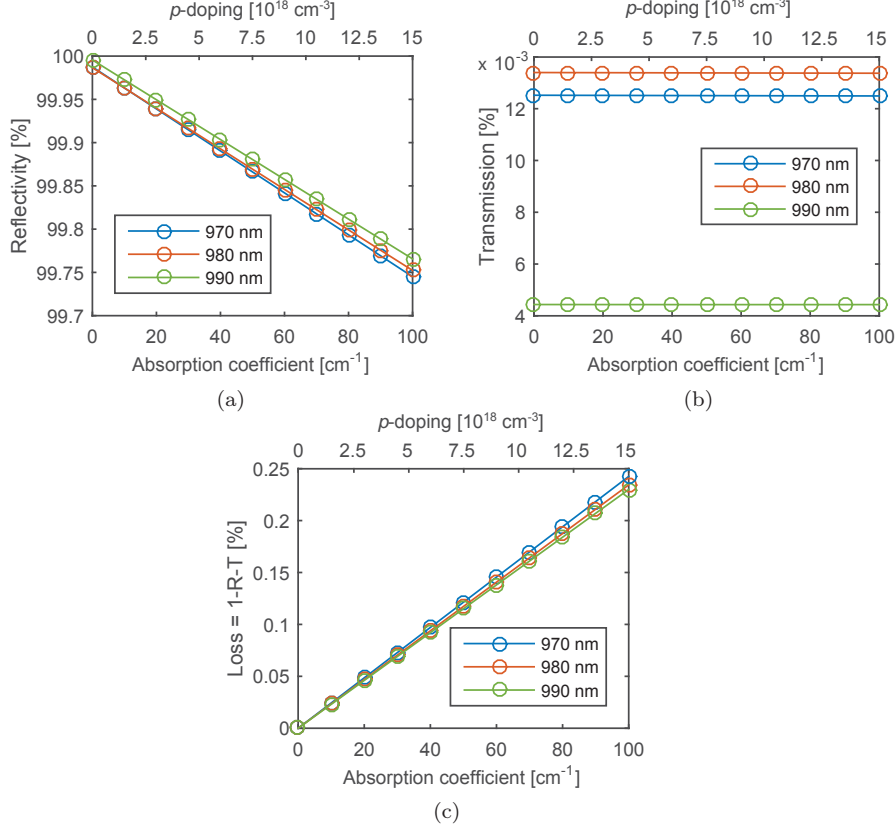


Figure 6.4: RCWA simulation of the effect of free-carrier absorption on an HCG with thickness 270 nm, period 405 nm, and duty cycle 60%. (a) Power reflectivity, (b) transmission, and (c) loss as a function of absorption or p -doping calculated using Equation 6.2.

6.4 Design of Multi-Wavelength HCG-VCSEL Arrays

The resonance wavelength in any Fabry-Perot cavity is set by the round-trip phase according to

$$\phi_{rt} = \phi_{m1} + 2\phi_{cav} + \phi_{m2} = 2\pi m = \frac{2\pi n_{eff}}{\lambda_0} \cdot 2L_{eff} \quad (6.3)$$

where ϕ_{m1} and ϕ_{m2} are the reflection phase of the mirrors, ϕ_{cav} is the phase accumulated by traversing the cavity, m is an integer, n_{eff} the effective mode

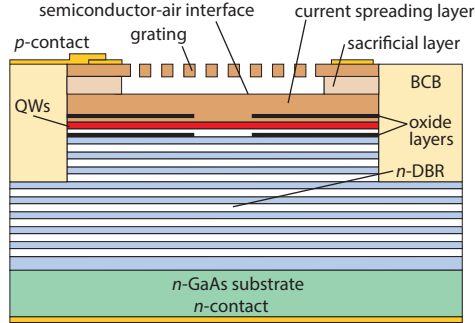


Figure 6.5: Schematic figure of an HCG-VCSEL. Note that the dimensions are not to scale; the true mesa diameter is 40-50 μm and the mesa height is $\sim 2.5 \mu\text{m}$.

index, and L_{eff} the effective cavity length. By using an HCG top mirror, ϕ_{m1} will be different for VCSELs with different HCG parameters, since the reflection phase of the HCG varies according to Figure 6.3b. The reflection phase from the bottom DBR (ϕ_{m2}) is relatively insensitive to wavelength, and may be regarded as a constant throughout the wavelength range of interest. A schematic figure of an HCG-VCSEL, designed for emission at 980 nm, is seen in Figure 6.5. There are a number of differences in designing an HCG-VCSEL compared to a conventional double-DBR VCSEL. The air gap below the HCG makes it similar in design to a MEMS-VCSEL, where the resonance wavelength is continuously tuned by moving the suspended top DBR to change the length of the air gap below. The most important design features for realization of multi-wavelength HCG-VCSEL arrays are discussed in detail below.

6.4.1 Transverse Electrical Confinement

Holes are injected through the thin p -GaAs current-spreading layer above the active region. For low resistance, the layer should be thick enough to enable efficient injection of holes, which have low mobility compared to electrons. However, a thick layer will increase the cavity length, leading to lower longitudinal confinement factor Γ and reduced wavelength change for a certain cavity phase shift [179], in effect reducing the obtainable wavelength span for the array. The thickness of the current-spreading layer also affects the thermal properties as it conducts heat away from the active region. A $3\lambda/4$ -thick current-spreading layer was used in our HCG-VCSEL design as a compromise between low resistance and low threshold gain. To further facilitate low resistance, while keeping free-carrier absorption low, the layer is modulation

p -doped with carbon, using a general level of $1 \cdot 10^{18} \text{ cm}^{-3}$ and $5 \cdot 10^{18} \text{ cm}^{-3}$ at the nodes of the optical standing wave.

The position of the oxide aperture is also critical. GaAs-based VCSELs are with few exceptions [118] grown with the p -side up, as it is simpler to grow high-quality QWs on n -doped AlGaAs-based DBRs than p -doped [180]. The limited thickness of the current spreading layer makes it tempting to put the oxide aperture below the active region in the top layer of the n -DBR. However, this may lead to a problem with electrons spreading outwards laterally above the oxide aperture. The result is a leakage current, generating electron-hole pairs that will not contribute to the stimulated emission. The slow holes are injected far out and must travel a considerable lateral distance, while the fast electrons can spread outwards as soon as they pass through the oxide aperture, attracted by the slow holes. The combination of a thin current-spreading layer and oxide aperture in the n -DBR leads to a large current leakage. To effectively confine the current, the final HCG-VCSEL structure therefore used one oxide layer on either side of the active region as seen in Figure 6.5.

6.4.2 Semiconductor-Air Interface

The presence of the intra-cavity semiconductor-air interface, between the current-spreading layer and the air-gap, has a large effect on the cavity resonance and threshold gain of an HCG-VCSEL (or MEMS-VCSEL). The semiconductor-air interface has a reflectivity of $\sim 30\%$ and will therefore have a large influence on the standing optical wave in the cavity [93, 181, 182]. Different positions of the interface with respect to the standing wave lead to three cavity configurations commonly studied for MEMS-VCSELs [181, 183].

- **Semiconductor-coupled cavity (SCC):** The interface is placed at an anti-node of the standing wave, see Figure 6.6a. This means that the air-gap thickness should be $L_g = (2k + 1)\lambda/4$, and thickness of the current-spreading layer $L_c = m\lambda/2$, with integers k and m . Since the air gap is an odd number of $\lambda/4$, it acts as the first layer of the top mirror. The large index difference at the semiconductor-air interface yields a high total top mirror reflectivity (for the combined air gap and HCG) and effectively confines the standing wave to the active region cavity. The result is a relatively large longitudinal confinement factor, and low cavity loss, both leading to a low threshold material gain. However, this design makes the resonance wavelength relatively unresponsive to the phase of HCG reflection (or the air gap length in the case of a MEMS-VCSEL).
- **Air-coupled cavity (ACC):** The interface is placed at a node of the standing wave, see Figure 6.6b. This means that the air gap should have a thickness of $L_g = k\lambda/2$, and the current-spreading layer $L_c = (2m + 1)\lambda/4$, where

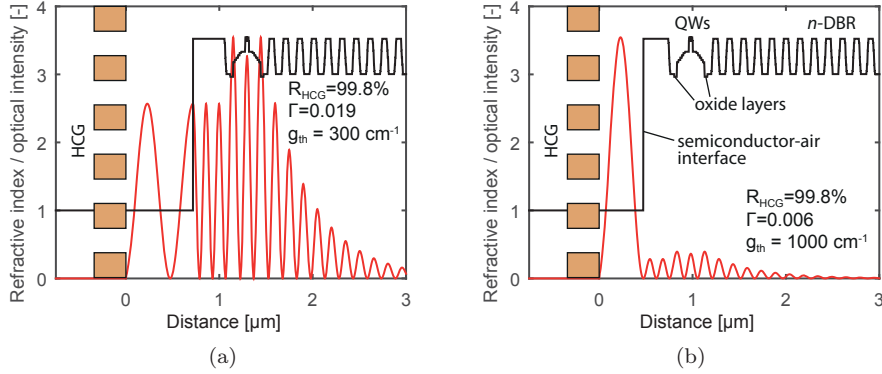


Figure 6.6: Refractive index profile and calculated field intensity of the standing optical wave for (a) SCC and (b) ACC cavity configuration. Calculated using gratings with 99.8% reflectivity for comparison of longitudinal confinement Γ and threshold material gain g_{th} .

k and m are integers. With this configuration the air gap acts as the cavity and the standing wave is strongly confined to the air gap. The semiconductor active region below acts as the first layer of the bottom DBR. This has the drawback of a considerably lower confinement factor, in turn demanding a significantly higher material threshold gain. However, the resonance wavelength becomes highly sensitive to the HCG reflection phase, enabling a wide range of wavelengths for the multi-wavelength HCG-VCSEL array (or large tuning range in a MEMS-VCSEL).

- **Extended cavity (EC):** By using an anti-reflection (AR) coating at the interface, the reflections from the interface are suppressed, and the standing wave distributes itself uniformly throughout both the air gap and semiconductor active region. This approach leads to a threshold gain only slightly higher than the SCC, but the wavelength span is somewhat reduced, compared to the ACC, due to a longer effective cavity length. The major drawback is a more complicated fabrication process because of the AR coating.

Widely tunable MEMS-VCSELs typically use the EC configuration as a good compromise between wide linear wavelength tuning and low threshold gain [183, 184]. Most electrically-injected HCG-VCSELs realized to date use the SCC configuration (exceptions [166, 185]), and also 2-4 DBR-pairs in the current spreading layer to boost the top mirror reflectivity [164, 166, 186–188]. The first realized HCG-VCSEL in 2007 featured an SCC with a 4-pair AlGaAs-based DBR above the active region acting as a current spreading layer [164].

Even though the authors claim that enough reflectivity could be provided by the HCG itself, a 4-pair DBR with $\text{Al}_{0.90}\text{Ga}_{0.10}\text{As}/\text{Al}_{0.12}\text{Ga}_{0.88}\text{As}$ has a reflectivity of about 70% (from transfer matrix calculations [92]), and therefore significantly increases the top mirror reflectivity. The combination of a SCC and a 4-pair DBR makes the VCSEL rather insensitive to the HCG phase, with a wavelength change of about 2 nm for changes in period and duty cycle [187, 189].

HCGs have also been used as the top mirror for tunable MEMS-VCSELs. Also here most designs feature an SCC, and a few DBR-pairs in the current-spreading layer, in order to get low enough threshold gain to reach lasing [169, 188]. The only exception is [185], which demonstrated a MEMS HCG-VCSEL with an EC configuration with an oxidized $\text{Al}_{0.98}\text{Ga}_{0.02}\text{As}$ layer as an AR coating, and no DBR-pairs in the current-spreading layer.

The HCG-VCSELs in this work use the ACC configuration in order to obtain a large wavelength span from the different HCG reflection phases (Figure 6.3b). Owing to the high threshold gain, this configuration has in the past often been considered impractical for MEMS-VCSELs [183]. In order to reach lasing in our HCG-VCSELs, we must achieve the needed top mirror reflectivity with only the HCG, without any assistance from the semiconductor-air interface or extra DBR-pairs. For comparison, for HCG-VCSELs with 99.8% HCG reflectivity, the threshold material gain is rather low at 300 cm^{-1} for the SCC, while the ACC requires 1000 cm^{-1} to reach threshold, see Figure 6.6. In order to reach threshold, HCGs with exceptionally high reflectivity are therefore required.

6.4.3 Wavelength-Setting and Threshold Material Gain

The wavelength setting and threshold characteristics of HCG-VCSELs using HCGs with different period/duty cycle combinations were investigated by a 1-D transfer-matrix method [92], where the HCG is replaced by an interface having the properties obtained from RCWA grating simulations. One such calculation can be seen in Figure 6.6b, and results for HCG-VCSELs with different HCGs can be seen in Figure 6.7. Each different HCG sets the resonance frequency and threshold gain depending on its parameters, so each point in Figure 6.7 represents a certain HCG-VCSEL design, with its corresponding threshold gain and resonance wavelength. A free-carrier absorption of 35 cm^{-1} , equivalent to a p -doping at $5 \cdot 10^{18}\text{ cm}^{-3}$, was included in the grating for the RCWA simulations. The HCG thickness of $t_g = 270\text{ nm}$ was chosen for the TM-HCGs since it results in a wide low-threshold-gain region, see Figure 6.7a. By varying both grating period and duty cycle, resonance wavelengths from 960-1000 nm are possible, while keeping the threshold material gain $<1000\text{ cm}^{-1}$. It should be noted that the material gain discussed in

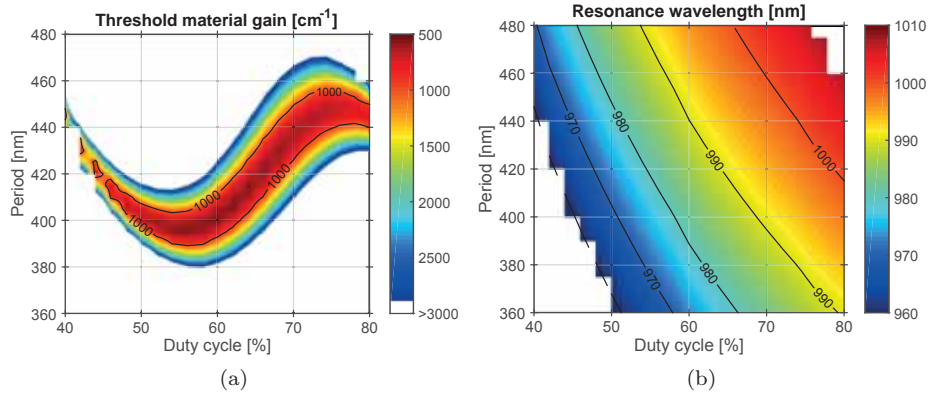


Figure 6.7: Simulated properties of HCG-VCSELs with different grating parameters (period and duty cycle) for an HCG thickness of $t_g = 270$ nm. (a) Threshold material gain. (b) Cavity resonance wavelength.

this chapter is the gain required in the active region to compensate the cavity losses for a certain longitudinal confinement factor. However, the QWs only provide gain over a limited spectral range, and may not be able to deliver the necessary material gain over the full wavelength span.

Chapter 7

HCG Fabrication

High-contrast gratings have sometimes been described and demonstrated as tolerant to processing imperfections [187]. While this has irrefutably been proven for HCG-VCSELs with a hybrid DBR-HCG top mirror and SCC configuration, the highly reflective gratings needed for multi-wavelength HCG-VCSEL arrays must be clean with little residue, close to rectangular cross-section, and low grating edge roughness. These demands make the HCG fabrication a challenging and delicate process. A schematic process flow for HCG fabrication is shown in Figure 7.1. First, the gratings are defined by electron-beam lithography. If a Si_xN_y hard mask is used, the HCG pattern is transferred into the Si_xN_y by dry etching. The gratings are then dry etched through the grating layer down to the sacrificial layer using either the hard mask or only the resist mask. The remaining mask is removed, and the sacrificial layer is etched away by a selective wet etch. After the etch, the gratings are not dried in air, as the grating bars would bend and stick to each other by surface tension. Instead critical point drying must be used, where the rinsing liquid is replaced by liquid CO_2 at high pressure, which is then removed without a liquid-gas phase transition.

A highly selective wet etch is needed to remove the sacrificial layer and underetch the grating. This makes the choice of material combination for the grating and sacrificial layers important. In addition to enable highly-selective wet etching, the materials must also be lattice matched to avoid strain which may lead to buckling of the suspended HCG bars. Two different grating/sacrificial layer material combinations were evaluated; GaAs/ $\text{In}_{0.49}\text{Ga}_{0.51}\text{P}$ for 980 nm HCGs, and $\text{Al}_{0.45}\text{Ga}_{0.55}\text{As}$ /GaAs for 850 nm HCGs. All scanning-electron microscope (SEM) images in this chapter are images of 980 nm GaAs

7. HCG FABRICATION

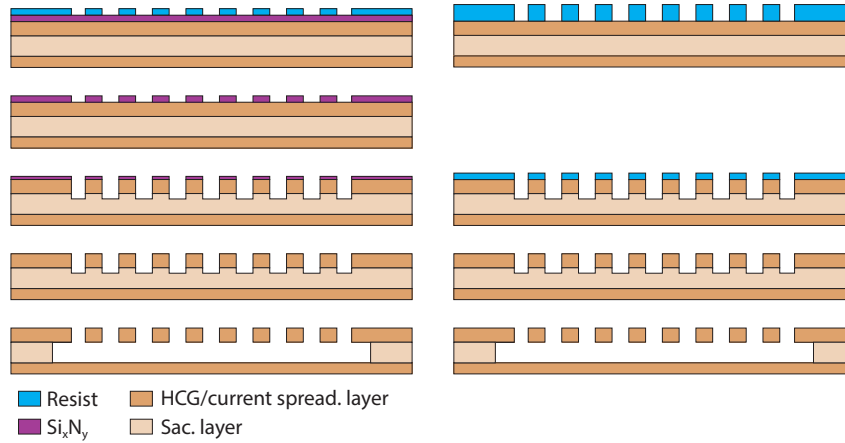


Figure 7.1: Process flow for the HCG process with Si_xN_y hard mask (left) and ZEP520A resist mask (right).

HCGs, except in the section on 850 nm $\text{Al}_{0.45}\text{Ga}_{0.55}\text{As}$ gratings. This chapter describes the different HCG fabrication steps and the materials used.

7.1 HCG Definition

The subwavelength dimension of the HCG prevents definition of the gratings by standard contact photolithography. Definition is instead commonly done with electron-beam lithography, which also has the benefit of a high degree of flexibility in grating layout, size, and period/duty cycle. The HCGs were defined in ZEP520A resist by electron-beam lithography, either directly on the grating layer, or on a previously deposited Si_xN_y to be used as a hard mask, see Figure 7.2. For the hard mask, the grating pattern was transferred from the resist to the Si_xN_y by ICP-RIE dry etching using NF_3 . Unfortunately, this etch is relatively isotropic, leading to lateral etching of the hard mask and therefore a shrinkage of the duty cycle by 5-15 percentage points. An example of duty cycle shrinkage from the ZEP520A to the Si_xN_y can be seen in Figure 7.2 (a)-(b). Instead of a hard mask, a thick layer of ZEP520A can be used as seen in Figure 7.2c. However, such a thick resist results in a high aspect ratio, complicating the subsequent dry etch of the grating layer.

Due to problems with HCG sidewall roughness, and duty cycle shrinkage, a thick layer of ZEP520A was used as the grating mask for the final successful HCG-VCSEL process. The hard mask definition process could potentially be

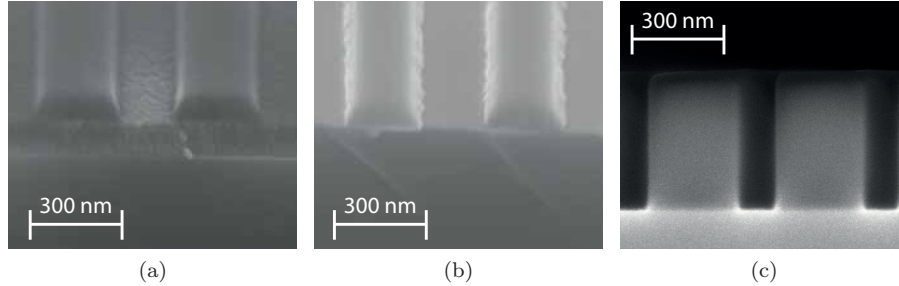


Figure 7.2: Close-up SEM images of the HCG definition. (a) Tilted SEM image of 90 nm ZEP520A on 105 nm Si_xN_y ($\Lambda=450$ nm, DC=60%). (b) Tilted SEM image of Si_xN_y hard mask ($\Lambda=450$ nm, DC=55%). (c) Cross-sectional SEM image of a 440 nm thick ZEP520A mask ($\Lambda=405$ nm, DC=71%). The low electrical conductivity of the resist makes it difficult to capture sharp SEM images.

improved by another combination of material, resist thickness, and dry etch recipe. However, such an investigation would not be trivial.

7.2 HCG Dry Etching

After HCG definition, the HCG pattern was transferred into the grating layer by RIE etching into the sacrificial layer. A recipe using SiCl_4/Ar chemistry was used to etch the GaAs or $\text{Al}_{0.45}\text{Ga}_{0.55}\text{As}$ grating layer. Examples of etching with the Si_xN_y hard mask and ZEP520A resist mask can be seen in Figure 7.3. It should be noted that the etched grooves in Figure 7.3b are not deep enough for the released gratings to have a rectangular cross-section, and longer etch times were used in later HCG etching processes. The narrow dimensions and high aspect ratio of the grating etch leads to an etch rate in the grating grooves much lower than the rate for large area etching. For high aspect ratios, the physical part of the RIE etch is reduced as the groove sidewalls shadow a large range of angles for the impinging energetic ions. This is seen in Figure 7.3b, where the high aspect ratio leads to a pointed etch profile. Moreover, the deep and narrow grooves obstruct the flow of the reactive gas and removal of volatile etch products, slowing the etch down. This is sometimes referred to as aspect-ratio-dependent etching (ARDE). An example of ARDE can be seen by comparing Figure 7.3(a) and (b). For the 105 nm thick Si_xN_y hard mask, ~ 100 nm wide grooves etch about 50% slower than a large area, while for the thicker 440 nm ZEP520A resist mask, the even higher aspect ratio reduces the etch rate by up to 75%.

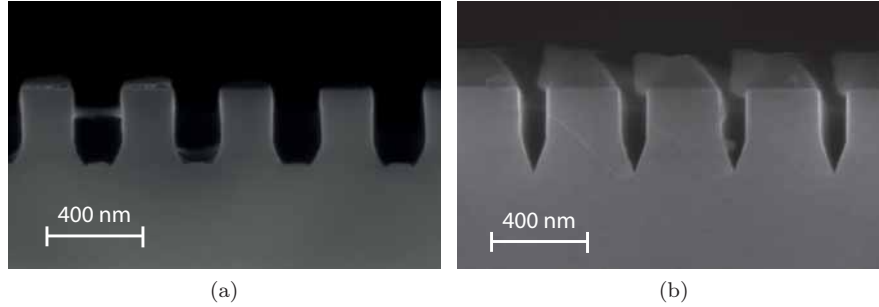


Figure 7.3: Cross-sectional SEM images of cleaved dry etched HCGs. (a) Etched with a 105 nm Si_xN_y hard mask. Mask still on ($\Lambda=405$ nm, $\text{DC}=53\%$). (b) Etched with a 440 nm ZEP520A mask. The remaining resist is distorted by charging in the SEM or cleaving. ($\Lambda=405$ nm, $\text{DC}=73\%$).

The result is long etch times, making erosion of the mask a critical issue for both the Si_xN_y and resist masks. As the mask is etched away, the etch will attack the grating bar top corners, giving the top of the grating bars a trapezoidal cross-section. Furthermore, for resist masks, long etch times lead to burnt resist residue that is difficult to remove. This was mitigated by improving the heat transfer from the chip during etching. The thermal conductivity between the chip and the sapphire carrier was facilitated by attaching the chip with a thermally conductive cooling grease, and cooling the backside of the carrier by a He-flow during the etch. After the grating dry etch, the hard mask was removed by RIE NF_3 -based etching. The ZEP520A mask was removed by a combination of O_2 plasma and ozone cleaning.

7.3 GaAs/InGaP HCGs for 980 nm VCSELs

For 980 nm HCGs GaAs is a good choice of grating material, while there are several possible choices for sacrificial layer. $\text{Al}_x\text{Ga}_{1-x}\text{As}$ with $x > 0.5$ may be used, as it can be etched selectively from GaAs with for instance HCl or HF [190, 191], and epitaxial growth of lattice matched $\text{Al}_x\text{Ga}_{1-x}\text{As}$ on GaAs for low strain is straightforward. However, the use of Al-containing compounds may lead to problems with oxidation of the remaining sacrificial layer. In addition, the limited selectivity of AlGaAs/GaAs wet etching will lead to a slight etching of the gratings and thereby a reduction of the grating thickness and duty cycle.

To avoid these problems, this work used $\text{In}_{0.49}\text{Ga}_{0.51}\text{P}$ as sacrificial layer material (from here on referred to as InGaP). In addition to allowing for lattice-matched epitaxial growth on GaAs, concentrated HCl (12 M, 37% by weight) can be used to etch InGaP with almost infinite selectivity over GaAs. HCl does not etch GaAs, except the $\sim 0.5\text{-}1$ nm thin native oxide which is always present after exposing the GaAs to air [192]. However, the InGaP etch is highly dependent on the crystal orientation. HCl will not etch InGaP in the direction of the $\{110\}$ cleavage planes. The HCGs must therefore be oriented at some angle to $\langle 110 \rangle$, or underetching of the HCGs will not be possible. Lateral underetching of InGaP was observed at a rate of $0.5\mu\text{m}/\text{min}$ in $\langle 100 \rangle$

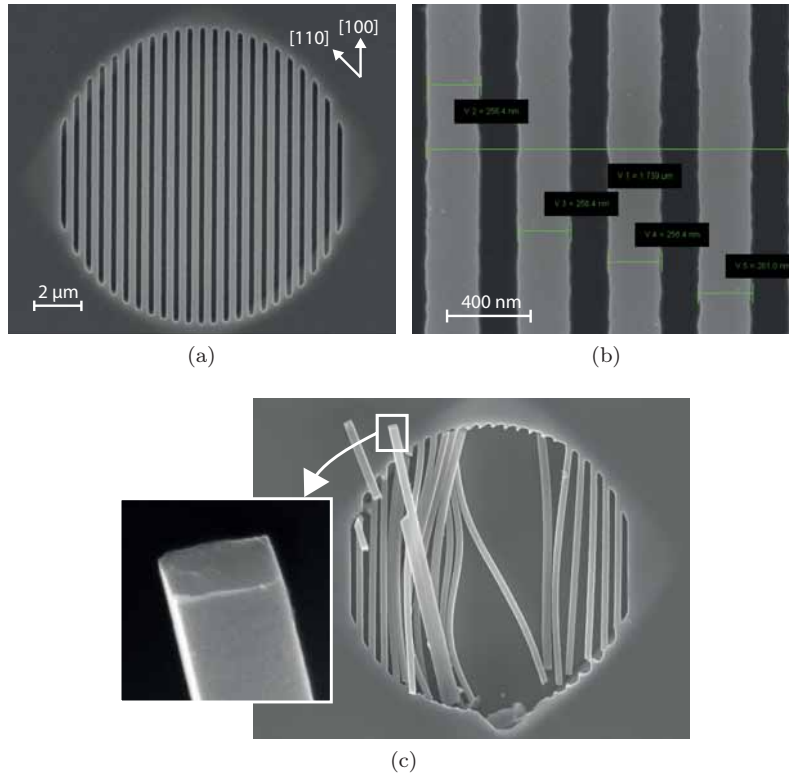


Figure 7.4: SEM images of a released HCG with bars oriented along $\langle 100 \rangle$ fabricated with the Si_xN_y hardmask process. Period 435 nm and 59% duty cycle. (a) The underetching in $\langle 100 \rangle$ can be seen as brighter areas outside the grating. (b) Close-up SEM image. (c) HCG intentionally broken with surface profiler. Inset: broken grating bar showing a rectangular cross-section.

(45° angle to the 110 cleavage planes), making etch times of 2-3 min sufficient for the HCG underetch. The crystallographic dependence was found to be in good agreement with [193]. Alternatively, the similar compound $\text{In}_x\text{Al}_{1-x}\text{P}$ could have been used as sacrificial layer, as demonstrated by Ansæk *et al.* for GaAs gratings in tunable 1060 nm MEMS HCG-VCSELs [185, 194].

No buckling of the bars of released GaAs gratings were observed, indicating low strain in the GaAs grating layer. Previously realized HCG-VCSELs often use stress-relieving trenches around the gratings [164], but we did not find this necessary. The underetching of the gratings can be directly confirmed by breaking the grating bars with a surface profiler. This enables direct observation of the semiconductor-air interface below the grating, and, with a bit of luck, the HCG cross-section can also be studied, as seen in Figure 7.4c.

7.4 AlGaAs/GaAs HCGs for 850 nm VCSELs

Our HCG-VCSEL efforts initially focused on 850 nm devices with gratings of $\text{Al}_{0.45}\text{Ga}_{0.55}\text{As}$ with a GaAs sacrificial layer. No successful 850 nm HCG-VCSELs were fabricated due to problems with the grating etch described in the next section. By the time these problems were resolved, the $\text{Al}_{0.45}\text{Ga}_{0.55}\text{As}$ gratings for 850 nm VCSELs had already been put aside in favor of the GaAs gratings for 980 nm VCSELs. The development of the HCG process is nevertheless presented here, since it could potentially be applied to fabricate 850 nm HCG-VCSELs. This is the only section where 850 nm $\text{Al}_{0.45}\text{Ga}_{0.55}\text{As}/\text{GaAs}$ HCGs are discussed.

Successful underetching and release of HCGs were first achieved by sacrificial layer etching with $\text{H}_2\text{O}_2:\text{NH}_4\text{OH}=1:50$ diluted with 5 parts water. However, the etchant was found to severely oxidize the $\text{Al}_{0.45}\text{Ga}_{0.55}\text{As}$ grating. The gratings were therefore underetched using the citric acid mixture described in [186], and used in for instance [164]. First, citric acid was mixed as anhydrous citric acid and water at a ratio of 1:1 by weight, and the pH value was adjusted to 6.5 with NH_4OH for high selectivity to AlGaAs [195]. It was then diluted as (citric acid mixture): $\text{H}_2\text{O}_2=5:1$ to further improve selectivity [196], and heated to 60°C. A slight anisotropy was observed with twice as fast underetch in $\langle 100 \rangle$ compared to $\langle 110 \rangle$.

A selectivity of around 250 to $\text{Al}_{0.45}\text{Ga}_{0.55}\text{As}$ was observed in good agreement with [197]. Even though this is a rather high selectivity it still has to be taken into consideration as the HCG properties are highly sensitive to the grating thickness. Assuming that an underetch of 1 μm is desired in $\langle 110 \rangle$, means that GaAs in $\langle 100 \rangle$ (vertical direction on our wafer) will etch 2 μm . With a selectivity of 250, the $\text{Al}_{0.45}\text{Ga}_{0.55}\text{As}$ grating will etch 8 nm on the top surface, and a bit less on the underside while the sacrificial layer is etched away. In total, the grating will be thinned by 10-15 nm during the release

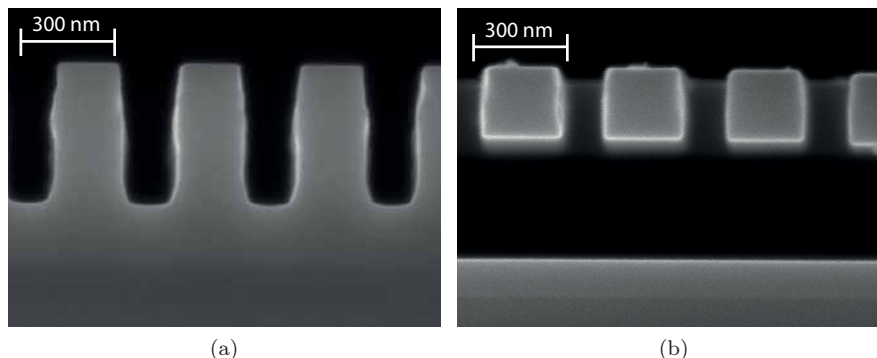


Figure 7.5: Cross-sectional SEM images from the $\text{Al}_{0.45}\text{Ga}_{0.55}\text{As}$ HCG fabrication. (a) After dry etch. (b) After release (cleaved prior to release etch). Note that these are two different gratings with different intended period/duty cycle.

etch. This is in good agreement with the observed thinning of underetched $\text{Al}_{0.45}\text{Ga}_{0.55}\text{As}$ layers observed in cross-sectional SEM, and must be taken into account for the HCG design. However, if the gratings would instead be aligned along $\langle 100 \rangle$, the underetch would be twice as fast, and the grating thickness reduction half as much. SEM images of released test HCGs can be seen in Figure 7.5. A rather rectangular cross-section is seen with somewhat slanted sidewalls. Released cross-sectional images such as Figure 7.5b are not possible with the 980 nm HCGs with InGaP sacrificial layer, since the InGaP will not underetch along the $\{110\}$ cleavage planes.

7.5 HCG-VCSEL Fabrication

The HCG-VCSELs were fabricated using the standard fabrication steps for oxide-confined VCSELs described in Chapter 5, as well as the HCG fabrication steps described previously. The HCGs were fabricated at the end of the fabrication process. Although, the HCG definition and dry etch could be done earlier in the fabrication, and underetched at the end, protecting the dry-etched grating surfaces during for instance wet oxidation would be troublesome. First, Ti/Pt/Au top p -contacts and Ni/Ge/Au backside n -contacts were deposited by electron-beam evaporation, and annealed 30 s at 430°C . Mesas with a diameter of 40-50 μm were etched in a three-step etch process. First, the top GaAs grating layer was etched away using a SiCl_4/Ar -based ICP-RIE dry etching process. The InGaP in the sacrificial layer etches very poorly in this chemistry, and was therefore removed by a wet etch using con-

centrated HCl. This step will underetch the mesa edges around 1 μm , but this is of no concern for the large mesas used. Finally, the ICP-RIE dry etch was used to etch partly into the n -DBR to expose the layers to be oxidized. The current apertures were formed by selective wet oxidation of one 30-nm-thick $\text{Al}_{0.98}\text{Ga}_{0.02}\text{As}$ layer on each side of the QWs. Prior to planarization with BCB, a Si_xN_y layer was deposited by PECVD to enhance the BCB adhesion. The BCB on top of the mesas was removed in a photolithography step, using the BCB as a negative photoresist. A short ICP-RIE dry etch with CF_4/O_2 made sure the BCB was completely removed from the mesa. The remaining Si_xN_y on the mesa was removed by NF_3 RIE etching before Ti/Au bondpads were deposited.

Throughout most of the fabrication, the top surface was protected by a layer of sputtered Si_xN_y in order to avoid contamination or unintentional etching. Each resist removal was performed using a combination of standard solvents, O_2 plasma ashing, and ozone cleaning. Especially ozone cleaning was found to be of vital importance, as the mesa surface must be absolutely clean before the HCG fabrication starts. Without the ozone clean, the HCG wet etch only worked a fraction of the attempts. Surprisingly, this problem was never observed when processing test HCGs on blank chips with no prior processing steps performed. The conclusion must be that even with thorough resist removal with solvents and O_2 plasma ashing, there are some residue left that does not hinder the HCG dry etch, but later obstructs the wet etch of the InGaP. The short 10 minute ozone cleaning likely forms an oxide layer on the GaAs grating layer which is thinner than one nanometer [198], which is removed in the final HCG wet etch.

After the bondpad deposition, and thorough cleaning of the mesa surface, the HCGs were fabricated using the ZEP520A etch mask as previously described. Full HCG-VCSEL structures were also fabricated using the Si_xN_y hard mask process, but no clear lasing was observed. Using only the resist mask seems to yield smoother grating sidewalls with a more rectangular cross-section, and thereby higher-reflective gratings. No successful 850 nm HCG-VCSELs with $\text{Al}_{0.45}\text{Ga}_{0.55}\text{As}$ gratings and GaAs sacrificial layer were processed because of the mentioned etch problems, that were later solved by the ozone cleaning. Once the problem had been solved, the project had already moved on to the 980 nm HCG-VCSELs.

Chapter 8

HCG-VCSEL Experiments

The main experimental results for multi-wavelength HCG-VCSEL arrays can be found in Paper H, while this chapter presents results from reflection measurements on test HCGs, and some additional characteristics of the HCG-VCSELs. Note that only 980 nm GaAs HCGs are characterized.

8.1 Test Structures

Prior to integration of HCGs on full VCSEL structures, test structures consisting of only the grating and sacrificial layers were processed as part of the development of the HCG fabrication process. The epitaxial structure was grown by MOCVD on 2" (001)-GaAs wafers at the Royal Institute of Technology in Stockholm, Sweden. A 285 nm thick grating layer was grown on top of a 520 nm $\text{In}_{0.49}\text{Ga}_{0.51}\text{P}$ sacrificial layer. Both layers were *p*-doped to about $1 \cdot 10^{19} \text{ cm}^{-3}$. HCGs with periods of 435-475 nm and duty cycles 35-65% were fabricated using the Si_xN_y hard mask process (see Chapter 7). SEM images of the fabricated HCGs can be seen in Figure 7.4.

The reflectivity of the HCGs was investigated using a micro-reflectivity measurement setup at HP Labs in Palo Alto, CA, USA. Light from a fiber-coupled superluminescent diode, with a useful spectral width of around 100 nm at 1040 nm, was focused on the HCG using a lens setup, resulting in a spot size of 5 μm . The reflected light was then collected back into the single-mode fiber by the same lens setup, and connected to an optical spectrum analyzer (OSA) through a 3dB fiber coupler. The measurement was calibrated against electron-beam evaporated gold next to the HCGs, assuming a reflectivity of 98% for the gold throughout the entire wavelength range [199]. Due to chromatic aberrations in the lens package, its height had to be changed to maintain

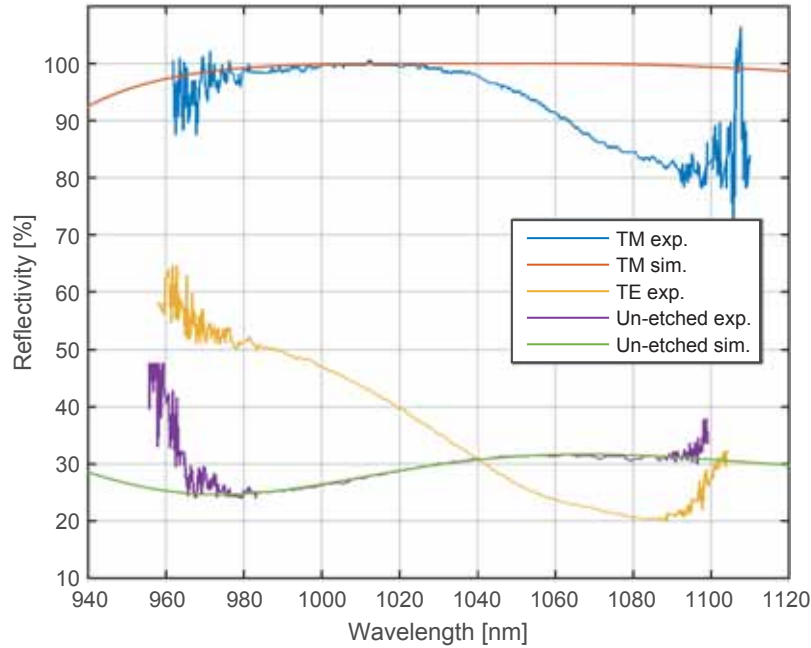


Figure 8.1: Measured and simulated reflectivity spectra of an HCG with period 435 nm, duty cycle 63%, and thickness of 285 nm. Un-etched refers to the as-grown three-layer epitaxial GaAs/InGaP/GaAs structure.

focus on the HCG throughout the wavelength range. Simultaneously, a hold-max function on the OSA was used to capture the reflectivity spectra. The measurements had to be performed rather quickly due to the limited stability of the light source.

One such reflection measurement can be seen in Figure 8.1. The measured reflectivity was compared with simulations, taking the air gap and the underlying GaAs interface into account using a transfer-matrix method [92]. For longer wavelengths there is some disagreement between the measured and simulated reflectivity, but a reflectivity close to 100% was measured around 1010 nm, with a large difference between TM and TE polarized light as expected.

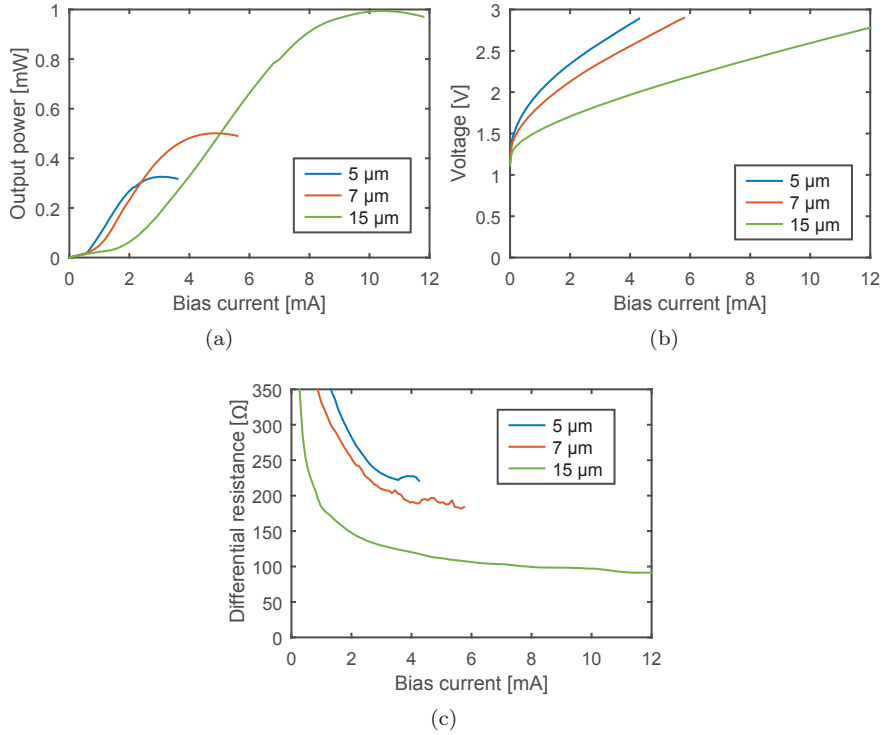


Figure 8.2: IPV characteristics of HCG-VCSELS with different oxide aperture diameters. (a) Output power vs. current measured with a large-area Si photodiode. (b) Voltage drop over the HCG-VCSEL vs. current. (c) Differential resistance vs. current.

8.2 HCG-VCSELS

Some basic characteristics of the HCG-VCSELS are presented here, while the design and performance of the multi-wavelength HCG-VCSEL arrays are presented in Paper H. The 980 nm HCG-VCSELS were fabricated as previously described in Chapter 7. The static current-power-voltage (IPV) characteristics of HCG-VCSELS with three different oxide aperture diameters are shown in Figure 8.2. Low threshold currents of 0.52, 0.78, and 1.95 mA were measured for the 5, 7, and 15 μm oxide aperture HCG-VCSELS, corresponding to threshold current densities of 2.6, 2.0, and 1.1 kA/cm^2 . The low threshold currents, similar to our standard double-DBR VCSELS, indicate excellent HCG reflectivity. With similar threshold currents, but lower confinement factor, this

signifies that the HCG reflectivities may be even higher than our standard top DBR reflectivity in Paper A. Despite low threshold currents, the output power is relatively low with a maximum power of ~ 0.5 mW for a $7\ \mu\text{m}$ oxide aperture HCG-VCSEL. The low slope efficiencies (~ 0.2 W/A) indicate either a low internal quantum efficiency, high internal optical loss, or simply a small HCG transmission (extremely high HCG reflectivity). However, the internal quantum efficiency can not be too bad, as the threshold currents are low. In any case, the vast majority of the photons generated by stimulated emission are not contributing to the HCG-VCSEL output power. The photons could, for instance, be absorbed by free-carrier absorption in the modulation-doped current-spreading layer or the doped HCG. The GaAs HCG layer is *p*-doped at $5 \cdot 10^{18}\ \text{cm}^{-3}$, which gives absorption losses in the HCG of around 0.08% per single pass from RCWA simulations (Figure 6.4c). Furthermore, the top 20 nm is a highly doped contact layer, doped at $5 \cdot 10^{19}\ \text{cm}^{-3}$, that could add further to the absorption loss of the HCG.

A large differential resistance was observed, with around $230\ \Omega$ for a $5\ \mu\text{m}$ oxide aperture HCG-VCSEL and $180\ \Omega$ for a $7\ \mu\text{m}$ oxide aperture device. The differential resistance is large compared to standard VCSELs, and also does not decrease as fast with increasing oxide aperture size, see Paper A. This is likely due to a large resistance associated with hole injection through the thin current-spreading layer. By using smaller-diameter gratings, the lateral distance the holes have to travel can be reduced. HCG diameters of 12, 14, and $22\ \mu\text{m}$ were used for the 5, 7, and $15\ \mu\text{m}$ oxide aperture diameters. Somewhat smaller HCG could be used, but it is important that the whole optical mode field is well covered by the HCG, or the cavity loss will rapidly increase [176].

Thermal rollover occurs at relatively low currents compared to standard VCSELs, indicating a rapid internal temperature increase due to self-heating. This is likely due to a combination of high thermal resistance in the structure as no top DBR is present to act as a heat-spreader, high resistance leading to large Joule heating, and relatively large internal optical absorption in the cavity. The wall-plug efficiencies are only about 5%, meaning that the rest of the supplied electrical power is converted to heat.

8.2.1 Single-Mode Emission

Single-mode emission is expected from HCG-VCSELs due to the angular selective reflection from the HCG [200, 201]. On the other hand, nonuniform injection of carriers due to the thin current-spreading layer may yield higher modal gain for the higher order modes. Single-mode emission with high side-mode suppression-ratio (SMSR) of >40 dB was observed for all 5 and most $7\ \mu\text{m}$ oxide aperture devices, see Figure 8.3. However, some $7\ \mu\text{m}$ oxide aperture HCG-VCSELs had two strongly lasing modes, and $15\ \mu\text{m}$ oxide aperture

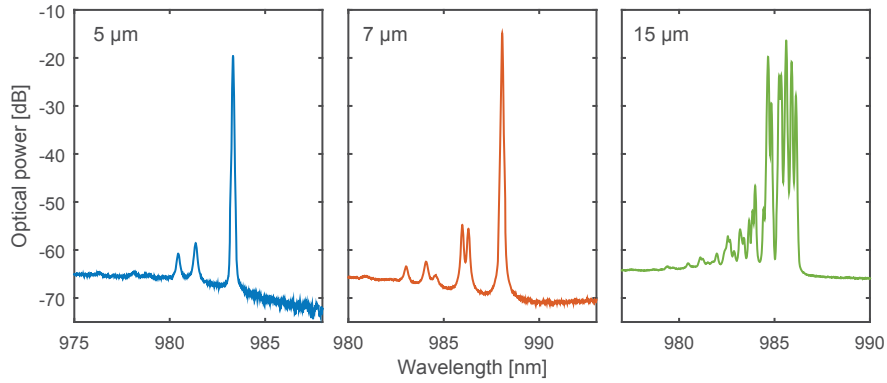


Figure 8.3: Optical spectra just below thermal rollover for 5, 7, and 15 μm oxide aperture HCG-VCSELS.

devices exhibited multimode emission. It is clear that the HCG is angular selective, since the standard VCSELS presented in this work are not single-mode for oxide apertures larger than $\sim 3 \mu\text{m}$ (Paper D). The angular dependence of the reflectivity for the specific HCGs implemented in this work has not been evaluated by simulations, and can likely be optimized for a larger angular dependence. On the other hand, there is a trade-off between broadband reflectivity and angular selective reflectivity [200]. Single-polarization emission is also expected from HCG-VCSELS due to the large difference in HCG reflectivity between TM and TE polarization, see Figure 8.1. Polarization discrimination measurements have not yet been performed on our HCG-VCSELS, but orthogonal-polarization suppression ratios in excess of 20 dB have been reported for other 850 nm TM-HCG-VCSELS [187].

Chapter 9

Outlook and Future Directions

It is clear that future optical interconnects will require a continuous improvement of high-speed VCSEL performance. This thesis and its appended papers aim at dissecting some important aspects, but there are many topics outside of the scope of this thesis. This chapter discusses some possible future directions for continued research.

Future optical interconnects for extremely high capacity (many Tbit/s) will likely use combination of high-speed VCSELs and photodetectors, advanced driver and receiver circuits with equalization [45], multilevel modulation formats [39], and multiplexing (e.g. ribbons of multicore fiber [79, 202] and/or WDM [62]). However, it is important to simultaneously strive for low power consumption, small footprint, and, as always, low cost. A further miniaturization by integration of III-V VCSELs on silicon is another important path, which could enable photonic integrated circuits with heterogeneously integrated VCSELs [171, 203], drivers, and silicon nitride waveguides [204], as well as other elements such as MUX/DEMUX for WDM [205].

Increasing the bandwidth of VCSELs (and photodiodes) continues to be an important path towards higher-speed optical interconnects. Even though advanced electronic compensation techniques will likely be used to boost the data rate [43–45], a high device bandwidth will simplify the driver and receiver circuit design, reducing their energy consumption and footprint. State-of-the-art high-speed VCSELs have very high intrinsic bandwidths, but are restrained by parasitics and thermal effects (see Section 3.4 and Paper A). Special attention should be paid to device resistance since it impacts both the parasitics and the self-heating. Thermal effects may be improved by moving from 850 to 1060 nm, due to higher differential gain [29], deeper QWs for lower carrier leakage [100], the use of binary GaAs for improved thermal conductivity [117],

and the possibility of bottom emitting devices for flip-chip mounting [30].

Longer-reach MMF links (>500 m) might not become economically viable, depending on the future cost of MMF and SMF, and the transceivers. However, an introduction of WDM could tip the balance in favor for MMF. Anyway, quasi-single-mode VCSELs will still be needed to increase the data rate of links up to 500 m to ≥ 25 Gbit/s. Since the next standard data rate after 25 Gbit/s is expected to be 40 Gbit/s, a logical next step would be to pursue quasi-single-mode VCSELs capable of transmitting 40 Gbit/s over 500 m of MMF. This could be accomplished by simultaneous optimization of the spectral and dynamic properties. In a mode-filter VCSEL this requires a higher total top mirror loss, while keeping the modal discrimination large. This could be achieved by using fewer mirror pairs (equivalent to moving further to the right in Figure 4.2b). Longer-reach optical interconnects would also benefit from longer wavelengths due to the reduced loss and chromatic dispersion in the silica used in MMFs [74].

After more than three years of work, the fact that air-coupled-cavity HCG-VCSELs could achieve lasing with low threshold currents was rather surprising to me. Lasing devices were only recently realized (July 2015), and more detailed measurements and analyses (of for instance thermal properties) could not be performed in time for this thesis. However, the performance can probably be significantly improved by considering the following points:

- **Larger wavelength span:** Successful fabrication of HCGs with duty cycles covering the full span of 40-85% would enable an even larger span of resonance wavelengths. However, simultaneous dry etching of HCGs with significantly different aspect ratios is not trivial due to aspect ratio dependent etching. Ultimately, the achievable lasing span for any multi-wavelength VCSEL array is limited by the gain bandwidth of the QWs, which will also lead to a variation in device performance across the array (e.g. threshold current, output power, and differential gain).
- **Higher output power:** Despite low threshold currents the output power is rather low. One reason could simply be that the HCG transmission is too low, leading to a large internal absorption and low slope efficiency. If this is the case, bottom emitting devices could be designed, with $\sim 100\%$ -reflective undoped HCGs top mirrors. Another concern is the HCG loss predicted by RCWA simulations, induced by free-carrier absorption due to doping. Experimental verification by evaluation of an undoped HCG would therefore be interesting. A third obvious critical issue is the early thermal rollover of the HCG-VCSELs. Future designs would need to pay significant attention to heat-sinking and thermal conductivity.
- **High-speed design:** A high-speed design of any WDM VCSEL array would involve trade-offs between the static and dynamic properties. How-

ever, HCGs are at an advantage since the wavelength and top-mirror reflectivity can be varied independent of each other in a single process step, which is not possible with any other technique (Section 6.1). For instance, a uniform threshold current could be achieved by tailoring the HCG reflectivity to compensate for the spectral variation of the QW gain.

Whether HCG-VCSELs are the most suitable technique to realize monolithically-integrated WDM arrays remains uncertain, due to the complicated fabrication and the relatively low efficiencies so far presented for HCG-VCSELs [164, 166, 187, 194]. It is in fact unclear whether any of the monolithic multi-wavelength VCSEL techniques, presented in Section 6.1, have the capability of high-speed modulation over a sufficiently wide wavelength span for practical use in uncooled optical interconnects. The industry is therefore currently exploring coarse WDM using discrete VCSELs fabricated from different wafers [75, 85]. However, this demonstrates a real need for multi-wavelength VCSEL arrays, motivating continued research towards wide-span high-speed monolithic multi-wavelength VCSEL arrays.

Chapter 10

Summary of Papers

Paper A

“High-speed VCSELs with strong confinement of optical fields and carriers,” to appear in *J. of Lightwave Technol.*, vol. 33, no. 24, pp. 1-9, Dec. 2015, (invited paper).

This invited paper presents the design, fabrication, and performance of a new generation of 850 nm high-speed VCSELs, where both carriers and optical fields are strongly confined to the active region. A short $1/2\text{-}\lambda$ cavity provides a large longitudinal optical confinement. The strong lateral confinement of carriers was obtained by positioning the oxide layers close to the QWs, yielding high internal quantum efficiencies, low threshold currents, and high WPEs of up to 34% for 7.5 μm oxide aperture VCSELs at RT and 24% at 85°C. An analysis of the temperature-dependent small-signal modulation response indicates that the bandwidth is limited by parasitics at RT, and by a combination of parasitics and thermal effects at 85°C.

My contribution: I participated in the design work, fabricated the VCSELs, performed all the measurements, and analyzed the results. I wrote the paper and presented the results at the European Conference on Lasers and Electro-Optics 2015 (Munich, Germany).

Paper B

“30 GHz bandwidth 850 nm VCSEL with sub-100 fJ/bit energy dissipation at 25-50 Gbit/s,” *Electron. Lett.*, vol. 51, no. 14, pp. 1096-1098, July 2015.

In this paper we present results from data transmission experiments using the VCSEL design presented in Paper A. A record-high modulation bandwidth of 30 GHz is demonstrated for a small-oxide-aperture VCSEL. High internal quantum efficiency and low threshold currents contributed to a high D -factor of $17.5 \text{ GHz/mA}^{1/2}$, and a bandwidth of 25 GHz already at a bias current of 1.8 mA. This enabled error-free ($\text{BER} < 10^{-12}$) energy-efficient high-speed data transmission at 40 and 50 Gbit/s, with record-low dissipated energy in the VCSEL of 73 and 95 fJ/bit, respectively.

My contribution: I fabricated the VCSELs, identified energy-efficient high-speed data transmission as a promising application, performed all the measurements, and analyzed the results. I wrote the paper and presented the results at the European Conference on Lasers and Electro-Optics 2015 (Munich, Germany).

Paper C

“20 Gbit/s error-free operation of 850 nm oxide-confined VCSELs beyond 1 km of multimode fibre,” *Electron. Lett.*, vol. 48, no. 19, pp. 1225-1227, Sept. 2012.

In this paper we present long-reach transmission using a small-oxide aperture ($\sim 3 \mu\text{m}$) quasi-single-mode VCSEL. A narrow RMS spectral width of 0.29 nm reduced the effect of chromatic dispersion in the MMF. This enabled error-free ($\text{BER} < 10^{-12}$) transmission at 20 Gbit/s over 1.1 km, which was at that time a record bit-rate-distance product for directly-modulated VCSEL MMF links.

My contribution: I helped introduce R. Safaisini to the VCSEL fabrication process and assisted with the fabrication, measurements, and analysis. I also presented the result at the European VCSEL Day 2013 (Lausanne, Switzerland).

Paper D

“High-Speed 850 nm Quasi-Single-Mode VCSELs for Extended-Reach Optical Interconnects,” *J. Opt. Commun. Netw.*, vol. 5, no. 7, pp. 686-695, July 2013.

This paper is an expanded investigation of the quasi-single-mode VCSELs in Paper C, with a detailed discussion on the design and fabrication. The VCSEL dynamic properties were investigated by small-signal modulation measurements, demonstrating a bandwidth of 23 GHz and a large D -factor of 17.3 GHz/mA^{1/2}. A 10 GHz photoreceiver with an integrated transimpedance amplifier was used to demonstrate data transmission at 22 Gbit/s over 1100 m of OM4 MMF. A theoretical study of the influence of the receiver bandwidth on the link performance showed that a receiver with 15 GHz bandwidth should enable transmission at 25 Gbit/s over 1000 m. In addition, 2 km transmission at 20 Gbit/s could be possible with a receiver with >15 GHz bandwidth, but this also requires sufficient VCSEL output power to overcome fiber and connector losses.

My contribution: I aided R. Safaisini with the VCSEL fabrication process, and assisted with the measurements and analysis.

Paper E

“25 Gbit/s transmission over 500 m multimode fibre using 850 nm VCSEL with integrated mode filter,” *Electron. Lett.*, vol. 48, no. 9, pp. 517-518, April 2012.

The spectral width of high-speed VCSELs developed at Chalmers was reduced by integrating a surface-relief mode filter on the VCSEL surface. This enables VCSEL with narrow spectral width with larger oxide aperture than in Papers C and D. A significant reduction in RMS spectral width from 0.9 to 0.3 nm was obtained when etching a 1.5 μm diameter mode filter on a 5 μm oxide aperture VCSEL. A transmission distance of 500 m was achieved at 25 Gbit/s.

My contribution: I established the mode filter fabrication process and fabricated the VCSELs. I performed all the measurements, analyzed the results, wrote the paper, and presented the results at SPIE Photonics West 2012 (San Francisco, CA, USA).

Paper F

“Reducing the spectral width of high speed oxide confined VCSELs using an integrated mode filter,” *Proc. of SPIE*, vol. 8276, pp. 82760L1-8, Feb. 2012.

This conference paper is an expanded study on the mode filter VCSELs from Paper E with more details on device structure and mode filter functionality. Spectrally resolved near-field imaging was used to identify the different

transverse modes and their relative radial intensity distributions of a large-spectral-width high-speed VCSEL. The static and dynamic properties of three different 5 μm -aperture VCSELs are compared; one with a surface-relief mode filter, one without any surface etch (full anti-phase top DBR reflection), and one device with the entire surface etched to an in-phase reflection. As expected, the shallow surface etching has a significant influence on both static and dynamic properties.

My contribution: I fabricated the VCSELs, performed all the measurements, and analyzed the results. I wrote the paper and presented it at SPIE Photonics West 2012 (San Francisco, CA, USA).

Paper G

“20 Gb/s data transmission over 2 km multimode fibre using 850 nm mode filter VCSELs,” *Electron. Lett.*, vol. 50, no. 1, pp. 40-42, Jan. 2014., Aug. 2013.

This paper present a new generation of mode-filter VCSELs with improved mode filter fabrication process. By using a 6 μm oxide aperture VCSEL with a 3 μm surface-relief mode filter, single-mode output powers exceeding 4 mW was achieved for high-speed VCSELs. This enabled error-free ($\text{BER} < 10^{-12}$) transmission at 25 and 20 Gbit/s over 1300 and 2000 m of OM4 MMF, respectively. The resulting bit-rate-distance product of 40 Gbit·km/s is the highest ever reported for a directly-modulated OOK 850 nm VCSEL link.

My contribution: I fabricated the VCSELs together with R. Safaisini. In particular I performed the mode-filter fabrication process. I assisted with the measurements and analysis of the results. I co-authored the paper and was the corresponding author.

Paper H

“Demonstration of post-growth wavelength setting of VCSELs using high-contrast gratings,” submitted to *Optics Express*, Aug. 2015.

This paper demonstrates experimentally, for the first time, post-growth wavelength setting of electrically-injected VCSELs by varying the parameters of high-contrast gratings (HCGs). The design, fabrication, and static properties of multi-wavelength HCG-VCSEL arrays are presented. As the HCG reflection phase varies significantly with grating period and duty cycle, an HCG top mirror can set the VCSEL wavelength depending on its parameters. A cavity design for maximum wavelength setting range was used, requiring HCGs

with very high reflectivity. The air-suspended GaAs HCGs were realized by selectively removing a InGaP sacrificial layer. Lasing was observed over a wavelength span of 15 nm, starting at 977 nm. Sub-mA thresholds indicate excellent HCG reflectivity.

My contribution: I participated in the design work and developed the HCG fabrication process. I fabricated the HCG-VCSELs, performed all the measurements, and wrote the paper.

References

- [1] J. A. Kash, A. Benner, F. E. Doany, D. Kuchta, B. G. Lee, P. Pepeljugoski, L. Schares, C. Schow, and M. Taubenblatt, "Optical interconnects in future servers," in *Optical Fiber Communication Conference/National Fiber Optic Engineers Conference 2011*, p. OWQ1, Optical Society of America, 2011.
- [2] "Top #1 systems." <http://www.top500.org/featured/top-systems/>, accessed 2015-08-14, 2015.
- [3] N. Lehrer, "The largest data centers in the world." <http://www.networkcomputing.com/cloud-infrastructure/the-largest-data-centers-in-the-world/d/d-id/1269250>, accessed 2015-08-16, 2014.
- [4] Fédération Internationale de Football Association (FIFA), "Laws of the game," 2015/2016.
- [5] A. Flatman, "Data centre link lengths." http://www.ieee802.org/3/NGBASET/public/nov12/flatman_01a_1112_ngbt.pdf, accessed 2015-08-17, 2012.
- [6] H. Liu, C. F. Lam, and C. Johnson, "Scaling optical interconnects in datacenter networks opportunities and challenges for WDM," in *High Performance Interconnects (HOTI), 2010 IEEE 18th Annual Symposium on*, pp. 113–116, 2010.
- [7] J. Kash, A. Benner, F. Doany, D. Kuchta, B. Lee, P. Pepeljugoski, L. Schares, C. Schow, and M. Taubenblatt, "Optical interconnects in exascale supercomputers," in *23rd Annual Meeting of the IEEE Photonics Society*, pp. 483–484, Nov 2010.
- [8] A. Krishnamoorthy, K. Goossen, W. Jan, X. Zheng, R. Ho, G. Li, R. Rozier, F. Liu, D. Patil, J. Lexau, H. Schwetman, D. Feng, M. Asghari, T. Pinguet, and J. Cunningham, "Progress in low-power switched

REFERENCES

- optical interconnects,” *IEEE J. Sel. Top. Quantum Electron.*, vol. 17, pp. 357–376, March 2011.
- [9] “Obama orders speedy delivery of first exascale supercomputer.” <http://spectrum.ieee.org/tech-talk/computing/hardware/obama-orders-speedy-delivery-of-first-exascale-supercomputer->, accessed 2015-08-14, 2015.
- [10] A. Larsson, “Advances in VCSELs for communication and sensing,” *IEEE J. Sel. Top. Quantum Electron.*, vol. 17, no. 6, pp. 1552–1567, 2011.
- [11] R. W. Herrick, *Materials and Reliability Handbook for Semiconductor Optical and Electron Devices*. Springer Science+Business Media, 2013.
- [12] R. E. Freund, C. Bunge, N. N. Ledentsov, D. Molin, and C. Caspar, “High-speed transmission in multimode fibers,” *J. Lightw. Technol.*, vol. 28, no. 4, pp. 569–586, 2010.
- [13] M. Freebody, “Lasers evolve to meet the demands of optical communications,” *Photonics Spectra*, February 2012.
- [14] “Multimode optical fiber selection & specification,” tech. rep., Corning Cable Systems LLC, 2012.
- [15] N. Chitica, J. Carlsson, L.-G. Svenson, and M. Chacinski, “Vertical-cavity surface-emitting lasers enable high-density ultra-high bandwidth optical interconnects,” in *Proc. SPIE*, vol. 9381, p. 938103, 2015.
- [16] I. T. Organization, “Infiniband Roadmap.” http://www.infinibandta.org/content/pages.php?pg=technology_overview, accessed 2015-08-15, 2015.
- [17] R. Michalzik, ed., *VCSELs - Fundamentals, Technology and Applications of Vertical-Cavity Surface-Emitting Lasers*. Springer-Verlag Berlin Heidelberg, 2013.
- [18] K. Lear, V. Hietala, H. Hou, J. Banas, B. Hammons, J. Zolper, and S. Kilcoyne, “Small and large signal modulation of 850 nm oxide-confined vertical-cavity surface-emitting lasers,” *OSA TOPS*, vol. 15, pp. 69–74, 1997.
- [19] D. Kuchta, P. Pepeljugoski, and Y. Kwark, “VCSEL modulation at 20 Gb/s over 200 m of multimode fiber using a 3.3 V SiGe laser driver IC,” in *Advanced Semiconductor Lasers and Applications/Ultraviolet and Blue Lasers and Their Applications/Ultralong Haul DWDM Transmission and*

-
- Networking/WDM Components, 2001. Digest of the LEOS Summer Topica*, pp. 49–50, July 2001.
- [20] R. H. Johnson and D. M. Kuchta, “30 Gb/s directly modulated 850 nm datacom VCSELs,” in *Proc. Conference on Lasers and Electro-Optics*, paper CPDB2, 2008.
- [21] P. Westbergh, J. S. Gustavsson, B. Kögel, Å. Haglund, A. Larsson, A. Mutig, A. Nadtochiy, D. Bimberg, and A. Joel, “40 Gbit/s error-free operation of oxide-confined 850 nm VCSEL,” *Electron. Lett.*, vol. 46, no. 14, pp. 1014–1016, 2010.
- [22] P. Westbergh, J. Gustavsson, B. Kögel, Å. Haglund, A. Larsson, and A. Joel, “Speed enhancement of VCSELs by photon lifetime reduction,” *Electron. Lett.*, vol. 46, pp. 938–940, June 2010.
- [23] P. Westbergh, E. P. Haglund, E. Haglund, R. Safaisini, J. S. Gustavsson, and A. Larsson, “High-speed 850 nm VCSELs operating error free up to 57 Gbit/s,” *Electron. Lett.*, vol. 49, no. 16, pp. 1021–1023, 2013.
- [24] P. Westbergh, R. Safaisini, E. Haglund, J. S. Gustavsson, A. Larsson, M. Geen, R. Lawrence, and A. Joel, “High-speed oxide confined 850-nm VCSELs operating error-free at 40 Gb/s up to 85°C,” *IEEE Photon. Technol. Lett.*, vol. 25, no. 8, pp. 768–771, 2013.
- [25] D. Kuchta, A. Rylyakov, F. Doany, C. Schow, J. Proesel, C. Baks, P. Westbergh, J. Gustavsson, and A. Larsson, “A 71-Gb/s NRZ modulated 850-nm VCSEL-based optical link,” *IEEE Photon. Technol. Lett.*, vol. 27, pp. 577–580, March 2015.
- [26] D. Kuchta, A. Rylyakov, C. Schow, J. Proesel, C. Baks, P. Westbergh, J. Gustavsson, and A. Larsson, “A 50 Gb/s NRZ modulated 850 nm VCSEL transmitter operating error free to 90°C,” *Lightwave Technology, Journal of*, vol. 33, pp. 802–810, Feb 2015.
- [27] S. Fryslie, M. Siriani, D. Siriani, M. Johnson, and K. Choquette, “37-GHz modulation via resonance tuning in single-mode coherent vertical-cavity laser arrays,” *IEEE Photon. Technol. Lett.*, vol. 27, pp. 415–418, Feb 2015.
- [28] P. Moser, J. Lott, P. Wolf, G. Larisch, H. Li, and D. Bimberg, “Error-free 46 Gbit/s operation of oxide-confined 980 nm VCSELs at 85°C,” *Electron. Lett.*, vol. 50, pp. 1369–1371, September 2014.
- [29] L. Coldren, Y.-C. Chang, Y. Zheng, and C.-H. Lin, “Efficient sources for chip-to-chip to box-to-box communication within data centers,” in

REFERENCES

- Photonics Society Summer Topical Meeting Series, 2010 IEEE*, pp. 205–206, July 2010.
- [30] C. Schow, F. Doany, C. Baks, Y. Kwark, D. Kuchta, and J. Kash, “A single-chip CMOS-based parallel optical transceiver capable of 240-Gb/s bidirectional data rates,” *J. Lightw. Technol.*, vol. 27, pp. 915–929, April 2009.
- [31] R. Dangel, F. Horst, D. Jubin, N. Meier, J. Weiss, B. Offrein, B. Swatowski, C. Amb, D. Deshazer, and W. Weidner, “Development of versatile polymer waveguide flex technology for use in optical interconnects,” *J. Lightw. Technol.*, vol. 31, pp. 3915–3926, Dec 2013.
- [32] H. Li, P. Wolf, P. Moser, G. Larisch, A. Mutig, J. Lott, and D. Bimberg, “Impact of the quantum well gain-to-cavity etalon wavelength offset on the high temperature performance of high bit rate 980-nm VCSELs,” *Quantum Electronics, IEEE Journal of*, vol. 50, pp. 613–621, Aug 2014.
- [33] T. Anan, N. Suzuki, K. Yashiki, H. Fukatsu, H. Hatakeyama, T. Akagawa, K. Tokutome, and M. Tsuji, “High-speed ingaas vcsels for optical interconnections,” in *Proc. International Symposium on VCSELs and Integrated Photonics*, Dec 2007.
- [34] N. Suzuki, T. Anan, H. Hatakeyama, K. Fukatsu, K. Yashiki, J. Tokutome, T. Akagawa, and M. Tsuji, “High speed 1.1- μm -range InGaAs-based VCSELs,” *IEICE Trans. Electron.*, vol. E92, no. 7, pp. 942–950, 2009.
- [35] J. Heroux, T. Kise, M. Funabashi, T. Aoki, C. Schow, A. Rylyakov, and S. Nakagawa, “Energy-efficient 1060-nm optical link operating up to 28 Gb/s,” *Lightwave Technology, Journal of*, vol. 33, pp. 733–740, Feb 2015.
- [36] S. Imai, K. Takaki, S. Kamiya, H. Shimizu, J. Yoshida, Y. Kawakita, T. Takagi, K. Hiraiwa, H. Shimizu, T. Suzuki, N. Iwai, T. Ishikawa, N. Tsukiji, and A. Kasukawa, “Recorded low power dissipation in highly reliable 1060-nm VCSELs for $\text{t}\ddot{\text{t}}$ Green” optical interconnection,” *IEEE J. Sel. Top. Quantum Electron.*, vol. 17, pp. 1614–1620, Nov 2011.
- [37] K. Takaki, S. Imai, S. Kamiya, H. Shimizu, Y. Kawakita, K. Hiraiwa, T. Takagi, H. Shimizu, J. Yoshida, T. Ishikawa, N. Tsukiji, and A. Kasukawa, “1060nm VCSEL for inter-chip optical interconnection,” in *Proc. SPIE*, vol. 7952, pp. 795204–795204–7, 2011.
- [38] K. Szczerba, M. Karlsson, P. A. Andrekson, and A. Larsson, “Intersymbol interference penalties for OOK and 4-PAM in short-range optical

- communications,” in *Optical Fiber Communication Conference/National Fiber Optic Engineers Conference 2013*, p. OW4A.3, Optical Society of America, 2013.
- [39] K. Szczerba, P. Westbergh, M. Karlsson, P. A. Andrekson, and A. Larsson, “60 Gbits error-free 4-PAM operation with 850 nm VCSEL,” *Electron. Lett.*, vol. 49, no. 15, pp. 953–955, 2013.
- [40] X. Gu, M. Nakahama, A. Matsutani, M. Ahmed, A. Bakry, and F. Koyama, “850 nm transverse-coupled-cavity vertical-cavity surface-emitting laser with direct modulation bandwidth of over 30 GHz,” *Appl. Phys. Express*, vol. 8, no. 8, p. 082702, 2015.
- [41] H. Höpfner, M. Lindemann, N. C. Gerhardt, and M. R. Hofmann, “Controlled switching of ultrafast circular polarization oscillations in spin-polarized vertical-cavity surface-emitting lasers,” *Applied Physics Letters*, vol. 104, no. 2, p. 022409, 2014.
- [42] J. Proesel, B. G. Lee, C. W. Baks, and C. Schow, “35-Gb/s VCSEL-based optical link using 32-nm SOI CMOS circuits,” in *Optical Fiber Communication Conference/National Fiber Optic Engineers Conference 2013*, p. OM2H.2, Optical Society of America, 2013.
- [43] A. Rylyakov, C. Schow, J. Proesel, D. M. Kuchta, C. Baks, N. Y. Li, C. Xie, and K. Jackson, “A 40-Gb/s, 850-nm, VCSEL-based full optical link,” in *Optical Fiber Communication Conference*, p. OTh1E.1, Optical Society of America, 2012.
- [44] D. Kuchta, A. Rylyakov, C. Schow, J. Proesel, F. Doany, C. W. Baks, B. Hamel-Bissell, C. Kocot, L. Graham, R. Johnson, G. Landry, E. Shaw, A. MacInnes, and J. Tatum, “A 56.1Gb/s NRZ modulated 850nm VCSEL-based optical link,” in *Optical Fiber Communication Conference/National Fiber Optic Engineers Conference 2013*, p. OW1B.5, Optical Society of America, 2013.
- [45] D. Kuchta, A. V. Rylyakov, C. L. Schow, J. Proesel, C. Baks, P. Westbergh, J. S. Gustavsson, and A. Larsson, “64Gb/s transmission over 57m MMF using an NRZ modulated 850nm VCSEL,” in *Optical Fiber Communication Conference*, p. Th3C.2, Optical Society of America, 2014.
- [46] P. Moser, J. A. Lott, and D. Bimberg, “Energy efficiency of directly modulated oxide-confined high bit rate 850-nm VCSELs for optical interconnects,” *IEEE J. Sel. Top. Quantum Electron.*, vol. 19, no. 4, pp. 1702212–1702212, 2013.

REFERENCES

- [47] P. Wolf, P. Moser, G. Larisch, H. Li, J. Lott, and D. Bimberg, "Energy efficient 40 Gbit/s transmission with 850 nm VCSELs at 108 fJ/bit dissipated heat," *Electronics Letters*, vol. 49, pp. 666–667, May 2013.
- [48] P. Moser, W. Hofmann, P. Wolf, J. A. Lott, G. Larisch, A. Payusov, N. N. Ledentsov, and D. Bimberg, "81 fJ/bit energy-to-data ratio of 850 nm vertical-cavity surface-emitting lasers for optical interconnects," *Applied Physics Letters*, vol. 98, no. 23, 2011.
- [49] J.-W. Shi, J.-C. Yan, J.-M. Wun, J. Chen, and Y.-J. Yang, "Oxide-relief and Zn-diffusion 850-nm vertical-cavity surface-emitting lasers with extremely low energy-to-data-rate ratios for 40 Gbit/s operations," *IEEE J. Sel. Top. Quantum Electron.*, vol. 19, no. 2, pp. 7900208–7900208, 2013.
- [50] P. Westbergh, R. Safaisini, E. Haglund, B. Kögel, J. S. Gustavsson, A. Larsson, M. Geen, R. Lawrence, and A. Joel, "High-speed 850 nm VCSELs with 28 GHz modulation bandwidth operating error-free up to 44 Gbit/s," *Electron. Lett.*, vol. 48, no. 18, pp. 1145–1147, 2012.
- [51] P. Moser, J. A. Lott, P. Wolf, G. Larisch, H. Li, and D. Bimberg, "85-fJ dissipated energy per bit at 30 Gb/s across 500-m multimode fiber using 850-nm VCSELs," *IEEE Photon. Technol. Lett.*, vol. 25, no. 16, pp. 1638–1641, 2013.
- [52] P. Moser, P. Wolf, G. Larisch, H. Li, J. Lott, and D. Bimberg, "Energy efficient 850 nm VCSELs for error-free 30 Gb/s operation across 500 m of multimode optical fiber with 85 fJ of dissipated energy per bit," in *Optical Interconnects Conference, 2013 IEEE*, pp. 13–14, May 2013.
- [53] Y.-C. Chang, C. Wang, and L. Coldren, "High-efficiency, high-speed VCSELs with 35 Gbit/s error-free operation," *Electron. Lett.*, vol. 43, pp. 1022–1023, September 2007.
- [54] H. Li, P. Wolf, P. Moser, G. Larisch, A. Mutig, J. Lott, and D. Bimberg, "Energy-efficient and temperature-stable oxide-confined 980 nm VCSELs operating error-free at 38 Gbit/s at 85°C," *Electron. Lett.*, vol. 50, pp. 103–105, January 2014.
- [55] H. Li, P. Wolf, P. Moser, G. Larisch, J. Lott, and D. Bimberg, "Temperature-stable, energy-efficient, and high-bit rate oxide-confined 980-nm VCSELs for optical interconnects," *Selected Topics in Quantum Electronics, IEEE Journal of*, vol. 21, pp. 1–9, Nov 2015.
- [56] H. Li, P. Wolf, P. Moser, G. Larisch, J. Lott, and D. Bimberg, "Temperature-stable 980-nm VCSELs for 35-Gb/s operation at 85°C

- with 139-fJ/bit dissipated heat,” *IEEE Photon. Technol. Lett.*, vol. 26, pp. 2349–2352, Dec 2014.
- [57] P. Wolf, P. Moser, G. Larisch, W. Hofmann, and D. Bimberg, “High-speed and temperature-stable, oxide-confined 980-nm VCSELs for optical interconnects,” *IEEE J. Sel. Top. Quantum Electron.*, vol. 19, pp. 1701207–1701207, July 2013.
- [58] K. Yashiki, N. Suzuki, K. Fukatsu, T. Anan, H. Hatakeyama, and M. Tsuji, “1.1- μm -range high-speed tunnel junction vertical-cavity surface-emitting lasers,” *IEEE Photon. Technol. Lett.*, vol. 19, pp. 1883–1885, Dec 2007.
- [59] P. Moser, J. Lott, P. Wolf, G. Larisch, H. Li, N. Ledentsov, and D. Bimberg, “56 fJ dissipated energy per bit of oxide-confined 850 nm VCSELs operating at 25 Gbit/s,” *Electron. Lett.*, vol. 48, pp. 1292–1294, September 2012.
- [60] L. Qiu, E. J. Lawrence, B. Ayres, M. Schumacher, A. Amezcua, D. Molin, and G. Kuyt, “40GBASE-SR4 frame error rate test of chromatic dispersion compensating MMF,” in *Optical Fiber Communication Conference/National Fiber Optic Engineers Conference 2013*, p. NW1J.6, Optical Society of America, 2013.
- [61] A. Gholami, D. Molin, and P. Sillard, “Compensation of chromatic dispersion by modal dispersion in MMF- and VCSEL-based gigabit ethernet transmissions,” *IEEE Photon. Technol. Lett.*, vol. 21, no. 10, pp. 645–647, 2009.
- [62] J. Tatum, D. Gazula, L. Graham, J. Guenter, R. Johnson, J. King, C. Kocot, G. Landry, I. Lyubomirsky, A. MacInnes, E. Shaw, K. Balemarthy, R. Shubochkin, D. Vaidya, M. Yan, and F. Tang, “VCSEL-based interconnects for current and future data centers,” *J. Lightw. Technol.*, vol. 33, pp. 727–732, Feb 2015.
- [63] G. Giaretta, R. Michalzik, and A. J. Ritger, “Long distance (2.8 km), short wavelength (0.85 μm) data transmission at 10Gb/sec over new generation high bandwidth multimode fiber,” in *Proc. Conference on Lasers and Electro-Optics, San Fransisco*, pp. 683–684, 2000.
- [64] P. Pepeljugoski, D. Kuchta, Y. Kwark, P. Pleunis, and G. Kuyt, “15.6-Gb/s transmission over 1 km of next generation multimode fiber,” *IEEE Photon. Technol. Lett.*, vol. 14, no. 5, pp. 717–719, 2002.

REFERENCES

- [65] G. Fiol, J. A. Lott, N. N. Ledentsov, and D. Bimberg, "Multimode optical fibre communication at 25 Gbit/s over 300 m with small spectral-width 850 nm VCSELS," *Electron. Lett.*, vol. 47, no. 14, pp. 810–811, 2011.
- [66] P. Moser, J. A. Lott, P. Wolf, G. Larisch, A. Payusov, N. N. Ledentsov, W. Hofmann, and D. Bimberg, "99 fJ/(bit · km) energy to data-distance ratio at 17Gb/s across 1 km of multimode optical fiber with 850-nm single-mode VCSELS," *IEEE Photon. Technol. Lett.*, vol. 24, no. 1, pp. 19–21, 2012.
- [67] J.-W. Shi, Z.-R. Wei, K.-L. Chi, J.-W. Jiang, J.-M. Wun, I.-C. Lu, J. Chen, and Y.-J. Yang, "Single-mode, high-speed, and high-power vertical-cavity surface-emitting lasers at 850 nm for short to medium reach (2 km) optical interconnects," *J. Lightw. Technol.*, vol. 31, pp. 4037–4044, Dec 2013.
- [68] P. Moser, J. A. Lott, P. Wolf, G. Larisch, A. Payusov, N. N. Ledentsov, and D. Bimberg, "Energy-efficient oxide-confined 850-nm VCSELS for long-distance multimode fiber optical interconnects," *IEEE J. Sel. Top. Quantum Electron.*, vol. 19, no. 2, pp. 7900406–7900406, 2013.
- [69] P. Moser, P. Wolf, G. Larisch, J. A. Lott, and D. Bimberg, "Energy efficient 850 nm VCSELS for data and computer communication," in *European VCSEL Day 2013*, 2013.
- [70] M. Tan, S. Fryslie, J. A. Lott, N. N. Ledentsov, D. Bimberg, and K. Choquette, "Error-free transmission over 1-km OM4 multimode fiber at 25 Gb/s using a single mode photonic crystal vertical-cavity surface-emitting laser," *IEEE Photon. Technol. Lett.*, vol. PP, no. 99, pp. 1–1, 2013.
- [71] K. Szczerba, P. Westbergh, J. Karout, J. S. Gustavsson, Å. Haglund, M. Karlsson, P. A. Andrekson, E. Agrell, and A. Larsson, "4-PAM for high-speed short-range optical communications," *IEEE J. Opt. Commun. Netw.*, vol. 4, no. 11, pp. 885–894, 2012.
- [72] J. Castro, R. Pimpinella, B. Kose, Y. Huang, B. Lane, K. Szczerba, P. Westbergh, T. Lengyel, J. Gustavsson, A. Larsson, and P. Andrekson, "48.7-gb/s 4-pam transmission over 200 m of high bandwidth mmf using an 850-nm vcsel," *IEEE Photon. Technol. Lett.*, vol. 27, pp. 1799–1801, Sept 2015.
- [73] I.-C. Lu, C.-C. Wei, H.-Y. Chen, K.-Z. Chen, C.-H. Huang, K.-L. Chi, J.-W. Shi, F.-I. Lai, D.-H. Hsieh, H.-C. Kuo, W. Lin, S.-W. Chiu, and J. Chen, "Very high bit-rate distance product using high-power

-
- single-mode 850-nm VCSEL with discrete multitone modulation formats through OM4 multimode fiber,” *Selected Topics in Quantum Electronics, IEEE Journal of*, vol. 21, pp. 1–9, Nov 2015.
- [74] M.-J. Li, “Mmf for high data rate and short length applications,” in *Optical Fiber Communication Conference*, p. M3F.1, Optical Society of America, 2014.
- [75] D. Molin, M. Bigot, F. Achten, A. Amezcua, and P. Sillard, “850-950nm wideband OM4 multimode fiber for next-generation WDM systems,” in *Optical Fiber Communication Conference*, p. M3B.1, Optical Society of America, 2015.
- [76] Y. Sun, R. Shubochnik, and B. Zhu, “New development in optical fibers for data center applications,” in *Proc. SPIE*, vol. 9387, p. 938705, 2015.
- [77] A. Malacarne, V. Sorianello, A. Daly, B. Kögel, M. Ortsiefer, S. Melo, C. Neumeyr, M. Romagnoli, and A. Bogoni, “High-speed long-wavelength VCSELs for energy-efficient 40 Gbps links up to 1 km without error correction,” in *Optical Fiber Communication Conference*, p. Tu2H.1, Optical Society of America, 2015.
- [78] C. Minkenbergh, “HPC networks: Challenges and the role of optics,” in *Optical Fiber Communication Conference*, p. W3D.3, Optical Society of America, 2015.
- [79] P. Westbergh, J. Gustavsson, and A. Larsson, “VCSEL arrays for multi-core fiber interconnects with an aggregate capacity of 240 Gb/s,” *IEEE Photon. Technol. Lett.*, vol. 27, pp. 296–299, Feb 2015.
- [80] P. Westbergh, J. Gustavsson, A. Larsson, T. Taunay, L. Bansal, and L. Gruner-Nielsen, “Crosstalk characteristics and performance of VCSEL array for multicore fiber interconnects,” *IEEE J. Sel. Top. Quantum Electron.*, vol. 21, pp. 1–7, Nov 2015.
- [81] R. Michalzik, G. Giaretta, K. W. Goossen, J. A. Walkers, and M. C. Nuss, “40 Gb/s coarse WDM data transmission with 825 nm wavelength VCSELs over 310 m of high-performance multimode fiber,” in *26th European Conference on Optical Communications (ECOC)*, no. 4, pp. 33–34, 2000.
- [82] K. Takaki, N. Iwai, and Hir, “Parallel-WDM for multi-Tb/s optical interconnects,” in *Lasers and Electro-Optics Society, 2005. LEOS 2005. The 18th Annual Meeting of the IEEE*, pp. 359–360, Oct 2005.

REFERENCES

- [83] B. Lemoff, M. Ali, G. Panotopoulos, G. Flower, B. Madhavan, A. Levi, and D. Dolfi, "MAUI: enabling fiber-to-the-processor with parallel multiwavelength optical interconnects," *Lightwave Technology, Journal of*, vol. 22, pp. 2043–2054, Sept 2004.
- [84] "Migrate to a 40-Gbps data center with Cisco QSFP BiDi technology." <http://www.cisco.com/c/en/us/products/collateral/switches/nexus-9000-series-switches/white-paper-c11-729493.html> , accessed 2015-08-23, 2013.
- [85] D. Kuchta, T. Huynh, F. Doany, A. Rylyakov, C. Schow, P. Pepeljugoski, D. Gazula, E. Shaw, and J. Tatum, "A 4- λ , 40Gb/s/ λ bandwidth extension of multimode fiber in the 850nm range," in *Optical Fiber Communication Conference*, p. W1D.4, Optical Society of America, 2015.
- [86] K. Iga, "Surface-emitting laser-its birth and generation of new optoelectronics field," *IEEE J. Sel. Top. Quantum Electron.*, vol. 6, no. 6, pp. 1201–1215, 2000.
- [87] H. Soda, K. ichi Iga, C. Kitahara, and Y. Suematsu, "GaInAsP/InP surface emitting injection lasers," *Jpn. J. Appl. Phys.*, vol. 18, no. 12, pp. 2329–2330, 1979.
- [88] F. Koyama, S. Kinoshita, and K. Iga, "Room-temperature continuous wave lasing characteristics of a GaAs vertical cavity surface-emitting laser," *Appl. Phys. Lett.*, vol. 55, no. 3, pp. 221–222, 1989.
- [89] Y. H. Lee, J. L. Jewell, A. Scherer, S. L. McCall, J. P. Harbison, and L. T. Florez, "Room-temperature continuous-wave vertical-cavity single-quantum-well microlaser diodes," *Electron. Lett.*, vol. 25, no. 20, pp. 1377–1378, 1989.
- [90] M. R. T. Tan, "Commercial applications of vertical cavity surface emitting lasers," in *Lasers and Electro-Optics, 2000. (CLEO 2000). Conference on*, p. 201, 2000.
- [91] "IQE delivers first 150mm (6") VCSEL epiwafers for high volume, low cost applications." <http://www.iqep.com/news/2014/03/iqe-delivers-first-150mm-vcsel-epiwafers/> , accessed 2015-08-11, 2014.
- [92] L. A. Coldren and S. W. Corzine, *Diode Lasers and Photonics Integrated Circuits*. John Wiley & Sons, 1995.
- [93] B. Kögel, P. Debernardi, P. Westbergh, J. S. Gustavsson, Å. Haglund, E. Haglund, J. Bengtsson, and A. Larsson, "Integrated MEMS-tunable

- VCSELs using a self-aligned reflow process,” *IEEE J. Quantum Electron.*, vol. 48, no. 2, pp. 144–152, 2012.
- [94] S. Adachi, ed., *Properties of Aluminium Gallium Arsenide*. London, UK: INSPEC, 1993.
- [95] R. N. Hall, G. E. Fenner, J. D. Kingsley, T. J. Soltys, and R. O. Carlson, “Coherent light emission from GaAs junctions,” *Phys. Rev. Lett.*, vol. 9, pp. 366–368, Nov 1962.
- [96] S. B. Healy, E. P. O’Reilly, J. S. Gustavsson, P. Westbergh, Å. Haglund, A. Larsson, and A. Joel, “Active region design for high-speed 850-nm VCSELs,” *IEEE J. Quantum Electron.*, vol. 46, no. 4, pp. 506–512, 2010.
- [97] E. Söderberg, J. Gustavsson, P. Modh, A. Larsson, Z. Zhang, J. Berggren, and M. Hammar, “High-temperature dynamics, high-speed modulation, and transmission experiments using 1.3- μm InGaAs single-mode VCSELs,” *J. Lightw. Technol.*, vol. 25, pp. 2791–2798, Sept 2007.
- [98] K. D. Choquette, K. M. Geib, C. I. H. Ashby, R. D. Twisten, O. Blum, H. Q. Hou, D. M. Follstaedt, B. Hammons, D. Mathes, and R. Hull, “Advances in selective wet oxidation of AlGaAs alloys,” *IEEE J. Sel. Top. Quantum Electron.*, vol. 3, no. 3, pp. 916–926, 1997.
- [99] B. Weigl, M. Grabherr, C. Jung, R. Jager, G. Reiner, R. Michalzik, D. Sowada, and K. J. Ebeling, “High-performance oxide-confined GaAs VCSELs,” *Selected Topics in Quantum Electronics, IEEE Journal of*, vol. 3, no. 2, pp. 409–415, 1997.
- [100] R. Nagarajan, M. Ishikawa, T. Fukushima, R. S. Geels, and J. Bowers, “High speed quantum-well lasers and carrier transport effects,” *Quantum Electronics, IEEE Journal of*, vol. 28, pp. 1990–2008, Oct 1992.
- [101] E. Hegblom, N. Margalit, A. Fiore, and L. Coldren, “High-performance small vertical-cavity lasers: a comparison of measured improvements in optical and current confinement in devices using tapered apertures,” *IEEE J. Sel. Top. Quantum Electron.*, vol. 5, pp. 553–560, May 1999.
- [102] M.-C. Amann and W. Hofmann, “InP-based long-wavelength VCSELs and VCSEL arrays,” *IEEE J. Sel. Top. Quantum Electron.*, vol. 15, no. 3, pp. 861–868, 2009.
- [103] K. J. Ebeling, *Semiconductor Quantum Optoelectronics: From Quantum Physics to Smart Devices*, ch. Analysis of vertical cavity surface emitting laser diodes (VCSEL), pp. 295–338. SUSSP Publications and Institute of Physics Publishing, 1999.

REFERENCES

- [104] B. E. A. Saleh and M. C. Teich, *Fundamentals of Photonics*. John Wiley & Sons, 2007.
- [105] P. Baveja, B. Kögel, P. Westbergh, J. S. Gustavsson, Å. Haglund, D. N. Maywar, G. P. Agrawal, and A. Larsson, “Impact of device parameters on thermal performance of high-speed oxide-confined 850-nm VCSELs,” *IEEE J. Quantum Electron.*, vol. 48, no. 1, pp. 17–26, 2012.
- [106] P. Westbergh, J. S. Gustavsson, Å. Haglund, M. Sköld, A. Joel, and A. Larsson, “High-speed, low-current-density 850 nm VCSELs,” *IEEE J. Sel. Top. Quantum Electron.*, vol. 15, no. 3, pp. 694–703, 2009.
- [107] W. Nakwaski, “Thermal aspects of efficient operation of vertical-cavity surface-emitting lasers,” *Opt. Quantum Electron.*, vol. 28, no. 4, pp. 335–352, 1996.
- [108] A. Mutig, G. Fiol, K. Potschke, P. Moser, D. Arsenijevic, V. Shchukin, N. Ledentsov, S. Mikhrin, I. Krestnikov, D. Livshits, A. Kovsh, F. Hopfer, and D. Bimberg, “Temperature-dependent small-signal analysis of high-speed high-temperature stable 980-nm VCSELs,” *IEEE J. Sel. Top. Quantum Electron.*, vol. 15, pp. 679–686, May 2009.
- [109] J. S. Gustavsson, *Modal Dynamics of Vertical-Cavity Surface-Emitting Lasers*. PhD thesis, Department of Microtechnology and Nanoscience, Chalmers University of Technology, 2003.
- [110] Y. Satuby and M. Orenstein, “Mode-coupling effects on the small-signal modulation of multitransverse-mode vertical-cavity semiconductor lasers,” *IEEE J. Quantum Electron.*, vol. 35, no. 6, pp. 944–954, 1999.
- [111] P. Westbergh, *High Speed Vertical Cavity Surface Emitting Lasers for Short Reach Communication*. PhD thesis, Department of Microtechnology and Nanoscience, Chalmers University of Technology, 2011.
- [112] P. Westbergh, J. S. Gustavsson, B. Kögel, Å. Haglund, and A. Larsson, “Impact of photon lifetime on high-speed VCSEL performance,” *IEEE J. Sel. Top. Quantum Electron.*, vol. 21, no. 6, pp. 1603–1613, 2011.
- [113] K. Osamura and Y. Murakami, “Free carrier absorption in n-GaAs,” *Japanese Journal of Applied Physics*, vol. 11, no. 3, p. 365, 1972.
- [114] H. Nishimoto, M. Yamaguchi, I. Mito, and K. Kobayashi, “High-frequency response for DFB LD due to a wavelength detuning effect,” *J. Lightw. Technol.*, vol. 5, pp. 1399–1402, Oct 1987.

-
- [115] Y.-A. Chang, T.-S. Ko, J.-R. Chen, F.-I. Lai, C.-L. Yu, I.-T. Wu, H.-C. Kuo, Y.-K. Kuo, L.-W. Lai, L.-H. Lai, T.-C. Lu, and S.-C. Wang, "The carrier blocking effect on 850 nm InAlGaAs/AlGaAs vertical-cavity surface-emitting lasers," *Semicond. Sci. Technol.*, vol. 21, no. 10, p. 1488, 2006.
- [116] E. R. Hegblom, *Engineering Oxide Apertures in Vertical Cavity Lasers*. PhD thesis, Department of Electrical and Computer Engineering, University of California at Santa Barbara, 1999.
- [117] S. Adachi, "Lattice thermal resistivity of III-V compound alloys," *J. Appl. Phys.*, vol. 54, no. 4, pp. 1844–1848, 1983.
- [118] A. Al-Omari, A. Ababneh, and K. Lear, "High-speed inverted-polarity oxide-confined Copper-plated 850-nm vertical-cavity lasers," *IEEE J. Sel. Top. Quantum Electron.*, vol. 21, pp. 1–8, Nov 2015.
- [119] M. Müller, W. Hofmann, T. Gründl, M. Horn, P. Wolf, R. Nagel, E. Ronneberg, G. Böhm, D. Bimberg, and M.-C. Amann, "1550-nm high-speed short-cavity VCSELs," *IEEE J. Sel. Top. Quantum Electron.*, vol. 17, pp. 1158–1166, Sept 2011.
- [120] Y. Ou, J. S. Gustavsson, P. Westbergh, Å. Haglund, A. Larsson, and A. Joel, "Impedance characteristics and parasitic speed limitations of high-speed 850-nm VCSELs," *IEEE Photon. Technol. Lett.*, vol. 21, no. 24, pp. 1840–1842, 2009.
- [121] H. Li, J. Lott, P. Wolf, P. Moser, G. Larisch, and D. Bimberg, "Temperature-dependent impedance characteristics of temperature-stable high-speed 980-nm VCSELs," *IEEE Photon. Technol. Lett.*, vol. 27, pp. 832–835, April 2015.
- [122] P. Moser, *Energy-efficient oxide-confined VCSELs for optical interconnects in data centers and supercomputers*. PhD thesis, Institut für Festkörperphysik, Technische Universität Berlin, 2015.
- [123] A. M. Nadtochiy, S. A. Blokhin, A. G. Kuzmenkov, M. Maksimov, N. A. Maleev, S. I. Troshkov, N. N. Ledentsov, V. M. Ustinov, A. Mutig, and D. Bimberg, "Decreasing parasitic capacitance in vertical-cavity surface-emitting laser with selectively oxidized aperture," *Tech. Phys. Lett.*, vol. 38, no. 2, pp. 106–109, 2012.
- [124] A. Adams, "Strained-layer quantum-well lasers," *IEEE J. Sel. Top. Quantum Electron.*, vol. 17, no. 5, pp. 1364–1373, 2011.

REFERENCES

- [125] E. Haglund, P. Westbergh, J. Gustavsson, and A. Larsson, "Impact of damping on high-speed large signal VCSEL dynamics," *J. Lightw. Technol.*, vol. 33, pp. 795–801, Feb 2015.
- [126] B. Hawkins, R. A. I. Hawthorne, J. K. Guenter, J. A. Tatum, and J. R. Biard, "Reliability of various size oxide aperture VCSELs," in *Electronic Components and Technology Conference, 2002. Proceedings. 52nd*, pp. 540–550, 2002.
- [127] J. Redd, "Statistical confidence levels for error-probability estimates," *Lightwave Magazine*, vol. 17, no. 5, 2000.
- [128] Å. Haglund, J. S. Gustavsson, J. Bengtsson, P. Jedrasik, and A. Larsson, "Design and evaluation of fundamental-mode and polarization-stabilized VCSELs with a subwavelength surface grating," *IEEE J. Quantum Electron.*, vol. 42, no. 3, pp. 231–240, 2006.
- [129] J. M. Ostermann, F. Rinaldi, P. Debernardi, and R. Michalzik, "VCSELs with enhanced single-mode power and stabilized polarization for oxygen sensing," *IEEE Photon. Technol. Lett.*, vol. 17, no. 11, pp. 2256–2258, 2005.
- [130] C. Jung, R. Jager, M. Grabherr, P. Schnitzer, R. Michalzik, B. Weigl, S. Muller, and K. J. Ebeling, "4.8 mW singlemode oxide confined top-surface emitting vertical-cavity laser diodes," *Electron. Lett.*, vol. 33, no. 21, pp. 1790–1791, 1997.
- [131] N. Ueki, A. Sakamoto, T. Nakamura, H. Nakayama, J. Sakurai, H. Otoma, Y. Miyamoto, M. Yoshikawa, and M. Fuse, "Single-transverse-mode 3.4-mW emission of oxide-confined 780-nm VCSELs," *IEEE Photon. Technol. Lett.*, vol. 11, pp. 1539–1541, Dec 1999.
- [132] H. Unold, M. Riedl, S. Mahmoud, R. Jager, and K. Ebeling, "Long monolithic cavity VCSELs for high singlemode output power," *Electron. Lett.*, vol. 37, pp. 178–179, Feb 2001.
- [133] Å. Haglund, J. S. Gustavsson, J. Vukusic, P. Modh, and A. Larsson, "Single fundamental-mode output power exceeding 6 mW from VCSELs with a shallow surface relief," *IEEE Photon. Technol. Lett.*, vol. 16, no. 2, pp. 368–370, 2004.
- [134] I. Kardosh, F. Demaria, F. Rinaldi, S. Menzel, and R. Michalzik, "High-power single transverse mode vertical-cavity surface-emitting lasers with monolithically integrated curved dielectric mirrors," *IEEE Photon. Technol. Lett.*, vol. 20, no. 24, pp. 2084–2086, 2008.

-
- [135] L. Y. Karachinsky, S. A. Blokhin, I. I. Novikov, N. A. Maleev, A. G. Kuzmenkov, M. A. Bobrov, J. A. Lott, N. N. Ledentsov, V. A. Shchukin, J.-R. Kropp, and D. Bimberg, "Reliability performance of 25 Gbit s⁻¹ 850nm vertical-cavity surface-emitting lasers," *Semicond. Sci. Technol.*, vol. 28, no. 6, p. 065010, 2013.
- [136] H. Martinsson, J. A. Vukusic, and A. Larsson, "Single-mode power dependence on surface relief size for mode-stabilized oxide-confined vertical-cavity surface-emitting lasers," *IEEE Photon. Technol. Lett.*, vol. 12, no. 9, pp. 1129–1131, 2000.
- [137] P. Dowd, L. Raddatz, Y. Sumaila, M. Asghari, I. White, R. V. Penty, P. Heard, G. C. Allen, R. Schneider, M. Tan, and S. Y. Wang, "Mode control in vertical-cavity surface-emitting lasers by post-processing using focused ion-beam etching," *IEEE Photon. Technol. Lett.*, vol. 9, no. 9, pp. 1193–1195, 1997.
- [138] H. J. Unold, S. W. Z. Mahmoud, R. Jager, M. Grabherr, R. Michalzik, and K. J. Ebeling, "Large-area single-mode VCSELs and the self-aligned surface relief," *IEEE J. Sel. Top. Quantum Electron.*, vol. 7, no. 2, pp. 386–392, 2001.
- [139] J. M. Ostermann, P. Debernardi, C. Jolics, and R. Michalzik, "Polarization-stable oxide-confined VCSELs with enhanced single-mode output power via monolithically integrated inverted grating reliefs," *IEEE J. Sel. Top. Quantum Electron.*, vol. 11, no. 5, pp. 982–989, 2005.
- [140] A. Kroner, F. Rinaldi, J. M. Ostermann, and R. Michalzik, "High-performance single fundamental mode AlGaAs VCSELs with mode-selective mirror reflectivities," *Opt. Commun.*, vol. 270, no. 2, pp. 332 – 335, 2007.
- [141] S. Arafin, A. Bachmann, K. Vizbaras, J. S. Gustavsson, A. Larsson, and M.-C. Amann, "Large-area single-mode GaSb-based VCSELs using an inverted surface relief," in *IEEE Photonics Society, 2010 23rd Annual Meeting of the*, pp. 61–62, 2010.
- [142] R. Williams, *Modern GaAs Processing Methods*. Artech House, Inc., 1990.
- [143] M. A. Verschuuren, P. Gerlach, H. A. van Sprang, and A. Polman, "Improved performance of polarization-stable VCSELs by monolithic sub-wavelength gratings produced by soft nano-imprint lithography," *Nanotechnology*, vol. 22, no. 50, p. 505201, 2011.

REFERENCES

- [144] J. H. E. Kim, L. Chrostowski, E. Bisailon, and D. V. Plant, “Dbr, sub-wavelength grating, and photonic crystal slab fabry-perot cavity design using phase analysis by fdtd,” *Opt. Express*, vol. 15, pp. 10330–10339, Aug 2007.
- [145] C. Sciancalepore, B. Bakir, S. Menezo, X. Letartre, D. Bordel, and P. Viktorovitch, “III-V-on-Si photonic crystal vertical-cavity surface-emitting laser arrays for wavelength division multiplexing,” *IEEE Photon. Technol. Lett.*, vol. 25, pp. 1111–1113, June 2013.
- [146] D. Huffaker and D. Deppe, “Multiwavelength, densely-packed 2 x 2 vertical-cavity surface-emitting laser array fabricated using selective oxidation,” *IEEE Photon. Technol. Lett.*, vol. 8, pp. 858–860, July 1996.
- [147] W. Hofmann, E. Wong, G. Böhm, M. Ortsiefer, N. Zhu, and M.-C. Amann, “1.55- μm VCSEL Arrays for high-bandwidth WDM-PONs,” *IEEE Photon. Technol. Lett.*, vol. 20, pp. 291–293, Feb 2008.
- [148] C. Chang-Hasnain, J. Harbison, C. en Zah, M. Maeda, L. Florez, N. Stoffel, and T.-P. Lee, “Multiple wavelength tunable surface-emitting laser arrays,” *IEEE J. Quantum Electron.*, vol. 27, pp. 1368–1376, Jun 1991.
- [149] F. Koyama, T. Mukaihara, Y. Hayashi, N. Ohnoki, N. Hatori, and K. Iga, “Two-dimensional multiwavelength surface emitting laser arrays fabricated by nonplanar MOCVD,” *Electron. Lett.*, vol. 30, pp. 1947–1948, Nov 1994.
- [150] M. Arai, T. Kondo, A. Onomura, A. Matsutani, T. Miyamoto, and F. Koyama, “Multiple-wavelength GaInAs-GaAs vertical cavity surface emitting laser array with extended wavelength span,” *IEEE J. Sel. Top. Quantum Electron.*, vol. 9, pp. 1367–1373, Sept 2003.
- [151] N. Nakahama, T. Sakaguchi, A. Matsutani, and F. Koyama, “Athermalization and on-chip multi-wavelength integration of VCSELs employing thermally actuated micromachined mirrors,” *Appl. Phys. Lett.*, vol. 105, p. 091110, 2014.
- [152] A. Fiore, Y. Akulova, J. Ko, E. Hegblom, and L. Coldren, “Postgrowth tuning of semiconductor vertical cavities for multiple-wavelength laser arrays,” *IEEE J. Quantum Electron.*, vol. 35, pp. 616–623, Apr 1999.
- [153] T. Wipiejewski, M. Peters, E. Hegblom, and L. Coldren, “Vertical-cavity surface-emitting laser diodes with post-growth wavelength adjustment,” *IEEE Photon. Technol. Lett.*, vol. 7, pp. 727–729, July 1995.

-
- [154] P. B. Dayal, T. Sakaguchi, A. Matsutani, and F. Koyama, "Multiple-wavelength vertical-cavity surface-emitting lasers by grading a spacer layer for short-reach wavelength division multiplexing applications," *Appl. Phys. Express*, vol. 2, p. 092501, 2009.
- [155] Y. Kawakita, K. Takaki, M. Funabashi, S. Imai, and A. Kasukawa, "1060nm single-mode multi-wavelength VCSEL array with intra-cavity phase tuning layers," in *International Semiconductor Laser Conference (ISLC)*, pp. 207–208, Sept 2014.
- [156] C. Xie, S. Spiga, P. Dong, P. Winzer, M. Bergmann, B. Kögel, C. Neumeier, and M.-C. Amann, "400-Gb/s PDM-4PAM WDM system using a monolithic 2x4 VCSEL array and coherent detection," *Lightwave Technology, Journal of*, vol. 33, pp. 670–677, Feb 2015.
- [157] A. Mereuta, A. Sirbu, A. Calilman, G. Suruceanu, V. Iakovlev, Z. Mickovic, and E. Kapon, "Fabrication and performance of 1.3- μm 10-Gb/s CWDM wafer-fused VCSELs grown by MOVPE," *J. Cryst. Growth*, 2015.
- [158] V. Karagodsky, B. Pesala, C. Chase, W. Hofmann, F. Koyama, and C. J. Chang-Hasnain, "Monolithically integrated multi-wavelength VCSEL arrays using high-contrast gratings," *Opt. Express*, vol. 18, pp. 694–699, Jan 2010.
- [159] Y. Rao, C. Chase, and C. Chang-Hasnain, "Multiwavelength HCG-VCSEL array," in *Semiconductor Laser Conference (ISLC), 2010 22nd IEEE International*, pp. 11–12, Sept 2010.
- [160] B.-L. Lee and C.-F. Lin, "Wide-range tunable semiconductor lasers using asymmetric dual quantum wells," *IEEE Photon. Technol. Lett.*, vol. 10, pp. 322–324, March 1998.
- [161] C. J. Chang-Hasnain and W. Yang, "High-contrast gratings for integrated optoelectronics," *Adv. Opt. Photon.*, vol. 4, pp. 379–440, Sep 2012.
- [162] C. Mateus, M. Huang, Y. Deng, A. R. Neureuther, and C. Chang-Hasnain, "Ultrabroadband mirror using low-index cladded subwavelength grating," *IEEE Photon. Technol. Lett.*, vol. 16, pp. 518–520, Feb 2004.
- [163] C. Mateus, M. Huang, L. Chen, C. Chang-Hasnain, and Y. Suzuki, "Broad-band mirror (1.12-1.62 μm) using a subwavelength grating," *IEEE Photon. Technol. Lett.*, vol. 16, pp. 1676–1678, July 2004.

REFERENCES

- [164] M. C. Y. Huang, Y. Zhou, and C. J. Chang-Hasnain, “A surface-emitting laser incorporating a high-index-contrast subwavelength grating,” *Nature Photon.*, vol. 1, pp. 119–122, 2007.
- [165] T. T. Wu, Y. C. Syu, S. H. Wu, W. T. Chen, T. C. Lu, S. C. Wang, H. P. Chiang, and D. P. Tsai, “Sub-wavelength GaN-based membrane high contrast grating reflectors,” *Opt. Express*, vol. 20, pp. 20551–20557, Aug 2012.
- [166] W. Hofmann, C. Chase, M. Müller, Y. Rao, C. Grasse, G. Böhm, M.-C. Amann, and C. Chang-Hasnain, “Long-wavelength high-contrast grating vertical-cavity surface-emitting laser,” *IEEE Photon. J.*, vol. 2, pp. 415–422, June 2010.
- [167] Y. Laaroussi, C. Chevallier, Frédéric Genty, N. Fressengeas, L. Cerutti, T. Taliercio, O. Gauthier-Lafaye, P.-F. Calmon, B. Reig, J. Jacquet, and G. Almuneau, “Oxide confinement and high contrast grating mirrors for mid-infrared VCSELs,” *Opt. Mater. Express*, vol. 3, pp. 1576–1585, Oct 2013.
- [168] Y. Rao, W. Yang, C. Chase, M. Huang, D. Worland, S. Khaleghi, M. Chitgarha, M. Ziyadi, A. Willner, and C. Chang-Hasnain, “Long-wavelength VCSEL using high-contrast grating,” *IEEE J. Sel. Top. Quantum Electron.*, vol. 19, pp. 1701311–1701311, July 2013.
- [169] M. C. Y. Huang, Y. Zhou, and C. J. Chang-Hasnain, “A nanoelectromechanical tunable laser,” *Nature Photon.*, vol. 2, pp. 180–184, 2008.
- [170] D. Fattal, L. Jingjing, Z. Peng, M. Fiorentino, and R. G. Beausoleil, “Flat dielectric grating reflectors with focusing abilities,” *Nature Photon.*, vol. 4, 2010.
- [171] G. C. Park, W. Xue, E. Semenova, K. Yvind, J. Mørk, and I. Chung, “III-V/SOI vertical cavity laser with in-plane output into a Si waveguide,” in *Optical Fiber Communication Conference*, p. W2A.17, Optical Society of America, 2015.
- [172] S. Kumari, J. S. Gustavsson, R. Wang, E. P. Haglund, P. Westbergh, D. Sanchez, E. Haglund, Å. Haglund, J. Bengtsson, N. Le Thomas, G. Roelkens, A. Larsson, and R. Baets, “High contrast grating for spatial mode filtering and mode control of vcsels,” in *Proc. SPIE*, vol. 9372, pp. 93720U–93720U–7, 2015.
- [173] J. Ferrara, W. Yang, L. Zhu, P. Qiao, and C. J. Chang-Hasnain, “Heterogeneously integrated long-wavelength vcsel using silicon high contrast

-
- grating on an soi substrate,” *Opt. Express*, vol. 23, pp. 2512–2523, Feb 2015.
- [174] I.-S. Chung, “Study on differences between high contrast grating reflectors for TM and TE polarizations and their impact on VCSEL designs,” *Opt. Express*, vol. 23, pp. 16730–16739, Jun 2015.
- [175] M. G. Moharam and T. K. Gaylord, “Rigorous coupled-wave analysis of planar-grating diffraction,” *J. Opt. Soc. Am.*, vol. 71, pp. 811–818, Jul 1981.
- [176] A. Liu, W. Hofmann, and D. Bimberg, “Two dimensional analysis of finite size high-contrast gratings for applications in VCSELs,” *Opt. Express*, vol. 22, pp. 11804–11811, May 2014.
- [177] L. Zhang, “A MATLAB based rigorous coupled-wave analysis (RCWA) tool.” <http://www-personal.umich.edu/~zlei/>, accessed 2015-08-11, 2010.
- [178] H. C. Casey and M. B. Panish, *Heterostructure Lasers*. Academic Press, 1st ed., 1978.
- [179] I.-S. Chung, V. Iakovlev, A. Sirbu, A. Mereuta, A. Caliman, E. Kapon, and J. Mörk, “Broadband MEMS-tunable high-index-contrast subwavelength grating long-wavelength VCSEL,” *Quantum Electronics, IEEE Journal of*, vol. 46, pp. 1245–1253, Sept 2010.
- [180] K. Lear, H. Hou, J. Banas, B. Hammons, J. Furioli, and M. Osinski, “Vertical cavity lasers on p-doped substrates,” *Electron. Lett.*, vol. 33, pp. 783–784, Apr 1997.
- [181] M. C. Larson, *Microelectromechanical wavelength-tunable vertical-cavity light-emitters and lasers*. PhD thesis, Department of Electrical Engineering, Stanford University, 1996.
- [182] T. Ansbæk, *Vertical-cavity surface-emitting lasers for medical diagnostics*. PhD thesis, Department of Photonics Engineering, Technical University of Denmark, 2013.
- [183] F. Sugihwo, M. Larson, and J. S. Harris, “Micromachined widely tunable vertical cavity laser diodes,” *J. Microelectromech. Syst.*, vol. 7, pp. 48–55, Mar 1998.
- [184] S. Paul, C. Gierl, J. Cesar, Q. T. Le, M. Malekizandi, B. Kögel, C. Neumeier, M. Ortsiefer, and F. Kuppers, “10-Gb/s direct modulation of widely tunable 1550-nm MEMS VCSEL,” *IEEE J. Sel. Top. Quantum Electron.*, vol. 21, pp. 1–8, Nov 2015.

REFERENCES

- [185] T. Ansbæk, I.-S. Chung, E. Semenova, and K. Yvind, “1060-nm tunable monolithic high index contrast subwavelength grating VCSEL,” *IEEE Photon. Technol. Lett.*, vol. 25, pp. 365–367, Feb 2013.
- [186] Y. Zhou, *Subwavelength High-Contrast Grating (HCG) and its Applications in Optoelectronic Devices*. PhD thesis, Electrical Engineering and Computer Sciences, University of California at Berkeley, 2008.
- [187] C. Chang-Hasnain, Y. Zhou, M. Huang, and C. Chase, “High-contrast grating VCSELs,” *IEEE J. Sel. Top. Quantum Electron.*, vol. 15, pp. 869–878, May 2009.
- [188] Y. Rao, *InP-based Long Wavelength VCSEL using High Contrast Grating*. PhD thesis, Electrical Engineering and Computer Sciences, University of California at Berkeley, 2012.
- [189] X. Gu, A. Imamura, and F. Koyama, “Wavelength trimming of vertical-cavity surface-emitting lasers with high-contrast subwavelength grating,” *Jpn. J. Appl. Phys.*, vol. 50, no. 10R, p. 100207, 2011.
- [190] X. Sun, L. Hu, H. Song, Z. Li, D. Li, and H. Jiang, “Selective wet etching of $\text{Al}_{0.7}\text{Ga}_{0.3}\text{As}$ layer in concentrated HCl solution for peeling off GaAs microtips,” *Solid-State Electron.*, vol. 53, no. 9, pp. 1032–1035, 2009.
- [191] X. Wu, L. Coldren, and J. Merz, “Selective etching characteristics of HF for $\text{Al}_x\text{Ga}_{1-x}\text{As}/\text{GaAs}$,” *Electron. Lett.*, vol. 21, pp. 558–559, June 1985.
- [192] L. Feng, L.-d. Zhang, H. Liu, X. Gao, Z. Miao, H.-c. Cheng, L. Wang, and S. Niu, “Characterization study of native oxides on GaAs(100) surface by XPS,” in *Proc. SPIE*, vol. 8912, pp. 89120N01–89120N10, 2013.
- [193] M. J. Cich, J. A. Johnson, G. M. Peake, and O. B. Spahn, “Crystallographic dependence of the lateral undercut wet etching rate of InGaP in HCl,” *Appl. Phys. Lett.*, vol. 82, no. 4, pp. 651–653, 2003.
- [194] T. Ansbæk, E. S. Semenova, K. Yvind, and O. Hansen, “Crystallographic dependence of the lateral undercut wet etch rate of $\text{Al}_{0.5}\text{In}_{0.5}\text{P}$ in diluted hcl for III-V sacrificial release,” *J. Vac. Sci. Technol. B*, vol. 31, no. 1, 2013.
- [195] T. Kitano, S. Izumi, H. Minami, T. Ishikawa, K. Sato, T. Sonoda, and M. Otsubo, “Selective wet etching for highly uniform GaAs/ $\text{Al}_{0.15}\text{Ga}_{0.85}\text{As}$ heterostructure field effect transistors,” *J. Vac. Sci. Technol. B*, vol. 15, no. 1, pp. 167–170, 1997.

-
- [196] G. C. DeSalvo, W. F. Tseng, and J. Comas, "Etch rates and selectivities of citric acid/hydrogen peroxide on GaAs, $\text{Al}_{0.3}\text{Ga}_{0.7}\text{As}$, $\text{In}_{0.2}\text{Ga}_{0.8}\text{As}$, $\text{In}_{0.53}\text{Ga}_{0.47}\text{As}$, $\text{In}_{0.52}\text{Al}_{0.48}\text{As}$, and InP," *J. Electrochem. Soc.*, vol. 139, no. 3, pp. 831–835, 1992.
- [197] E.-A. Moon, J.-L. Lee, and H. M. Yoo, "Selective wet etching of GaAs on $\text{Al}_x\text{Ga}_{1-x}\text{As}$ for AlGaAs/InGaAs/AlGaAs pseudomorphic high electron mobility transistor," *J. Appl. Phys.*, vol. 84, no. 7, pp. 3933–3938, 1998.
- [198] G. Hollinger, R. Skheyta-Kabbani, and M. Gendry, "Oxides on GaAs and InAs surfaces: An x-ray-photoelectron-spectroscopy study of reference compounds and thin oxide layers," *Phys. Rev. B*, vol. 49, pp. 11159–11167, Apr 1994.
- [199] J. M. Bennett and E. J. Ashley, "Infrared reflectance and emittance of silver and gold evaporated in ultrahigh vacuum," *Appl. Opt.*, vol. 4, pp. 221–224, Feb 1965.
- [200] F. Koyama, "High contrast grating for spatial mode filtering and mode control of vcsels," in *Proc. SPIE*, vol. 8270, pp. 827005–827005–8, 2012.
- [201] S. Inoue, J. Kashino, A. Matsutani, H. Ohtsuki, T. Miyashita, and F. Koyama, "Highly angular dependent high-contrast grating mirror and its application for transverse-mode control of VCSELs," *Jpn. J. Appl. Phys.*, vol. 53, no. 9, p. 090306, 2014.
- [202] B. Lee, D. Kuchta, F. Doany, C. Schow, P. Pepeljugoski, C. Baks, T. Tannay, B. Zhu, M. Yan, G. Oulundsen, D. S. Vaidya, W. Luo, and N. Li, "End-to-end multicore multimode fiber optic link operating up to 120 Gb/s," *J. Lightw. Technol.*, vol. 30, pp. 886–892, March 2012.
- [203] E. P. Haglund, S. Kumari, P. Westbergh, J. S. Gustavsson, G. Roelkens, R. Baets, and A. Larsson, "Silicon-integrated short-wavelength hybrid-cavity vcsel," *submitted to Opt. Express*, 2015.
- [204] A. Subramanian, P. Neutens, A. Dhakal, R. Jansen, T. Claes, X. Rottenberg, F. Peyskens, S. Selvaraja, P. Helin, B. Dubois, K. Leyssens, S. Severi, P. Deshpande, R. Baets, and P. Van Dorpe, "Low-loss single-mode PECVD Silicon Nitride photonic wire waveguides for 532-900 nm wavelength window fabricated within a CMOS pilot line," *IEEE Photon. J.*, vol. 5, pp. 2202809–2202809, Dec 2013.
- [205] D. Martens, A. Subramanian, S. Pathak, M. Vanslebrouck, P. Bienstman, W. Bogaerts, and R. Baets, "Compact Silicon Nitride arrayed waveguide gratings for very near-infrared wavelengths," *IEEE Photon. Technol. Lett.*, vol. 27, pp. 137–140, Jan 2015.

